

INVESTIGATION AND MODIFICATION OF THE MAGNETISM OF EPITAXIAL FE STRUCTURES

THÈSE N° 3388 (2005)

PRÉSENTÉE À LA FACULTÉ SCIENCES DE BASE

Institut de physique des nanostructures

SECTION DE PHYSIQUE

ÉCOLE POLYTECHNIQUE FÉDÉRALE DE LAUSANNE

POUR L'OBTENTION DU GRADE DE DOCTEUR ÈS SCIENCES

PAR

Diego REPETTO

Laurea in Fisica, Università di Genova, Italie
de nationalité italienne

acceptée sur proposition du jury:

Prof. K. Kern, directeur de thèse

H. Brune, rapporteur

Prof. L. Mattera, rapporteur

Prof. D. Pescia, rapporteur

Lausanne, EPFL
2006

Abstract

In this thesis, the magnetic and structural properties of layered epitaxial film systems and clusters are presented. A main achievement is the investigation of the direct correlation between magnetism and structural or morphological details of ultrathin films. For this purpose, the film structure has been accessed directly by means of surface science methods. The effect of structural changes on the magnetism were observed in-situ by magneto-optical techniques.

First, epitaxial Fe films grown at low temperature ($\sim 120\text{ K}$) on Cu(100) have been investigated. Such layers assume an fcc-crystal structure due to their interaction with the underlying Cu substrate. Within this work it is shown that the morphology of these films can be altered by annealing treatments. The thermally-induced morphological changes have direct consequences for domain wall propagation and result in increased coercivity and in modified surface anisotropy.

Flat fcc-Fe layers on Cu(100) have been used as templates to form fcc-Fe/Cu/Fe trilayers with coupled perpendicular magnetization. Such systems might be of relevance for data storage applications. The perpendicular coupling is ascribed to the realignment of the magnetization of the bottom Fe layer within the stray field produced by the top Fe layer magnetization. The magnetic coupling has been investigated as a function of the thickness of the top and the bottom Fe layer as well as the Cu spacer thickness. It was found that the magneto-static interaction is a direct consequence of the fcc-structure of both Fe layers and the interface roughness.

It is demonstrated that Fe films with fcc-structure and perpendicular magnetization can also be prepared on other fcc-templates, such as Pt substrates. Monatomic steps on the substrate surface are exploited to steer the growth of the film and with it the magnetism. Despite significant differences in the morphology and the atomic structure of Fe films on flat Pt(111) and stepped Pt(997), the critical thickness for the spin reorientation transition is similar on the two surfaces. However, the local atomic arrangement above three monolayer film thickness determines in-plane easy magnetization axis parallel to the step edges.

For all layered systems investigated in this thesis, epitaxial strain is a the driving force which influences the film structure and triggers structural transitions. The strain dependence of the morphology and the magnetism was probed by a comparative study of Fe deposited on Pt substrates with and without a noble gas buffer layer. The formation of relaxed Fe clusters during Xe layer desorption is favored in the absence of the overlayer-substrate interaction. Striking differences in the magnetic anisotropy between the systems are attributed to magneto-elastic contributions. Measurements of the blocking temperature of the Fe clusters allow estimating the cluster size.

All samples have been investigated under ultra high vacuum conditions. The study of the sample magnetic properties study was done by in-situ magneto-optical Kerr effect measurements and Kerr microscopy. Structural characterization was done by low energy electron diffraction and, in collaboration with other scientists, by scanning tunnelling microscopy.

Version abrégée

Dans cette thèse on présente une étude sur les propriétés magnétiques et structurales de films déposés par épitaxie et de clusters. Le principal résultat est l'observation de la correspondance directe entre le magnétisme et les détails structuraux ou morphologiques des films ultra minces. Dans ce but, la structure du film a été analysée directement au moyen de méthodes de science des surfaces. L'influence de la structure cristalline sur le magnétisme peut être observée in-situ par des techniques magnéto-optiques.

Dans un premier temps, la croissance par épitaxie à basses températures ($\sim 120 K$) de films de Fe sur du Cu(100) a été étudiée. De telles couches ont une structure cristalline de type cfc du fait de l'interaction avec le substrat de cuivre situé en dessous. Ce travail montre que la morphologie de ces films peut être altérée lors des expériences de recuit. Les changements morphologiques induits thermiquement ont des conséquences directes sur la propagation des parois des domaines. Ces changements produisent une augmentation de la coercitivité et une modification de l'anisotropie de surface.

Des couches minces de cfc-Fe sur du Cu(100) ont été utilisées comme base pour la formation de couches triples de cfc-Fe/Cu/Fe ayant une aimantation perpendiculaire couplée. De tels systèmes pourraient être pertinents pour des applications de stockage de données. Le couplage perpendiculaire est attribué au réalignement de l'aimantation de la couche inférieure de Fe située dans le champ dipolaire produit par l'aimantation de la couche supérieure de Fe. Le couplage magnétique a été étudié en fonction de l'épaisseur de la couche inférieure et supérieure de Fe ainsi qu'en fonction de l'épaisseur de la couche de Cu séparant celles de Fe. L'interaction magnéto-statique serait une conséquence directe de la structure cfc des deux couches de Fe et de la rugosité des interfaces.

Il est démontré que les films de Fe ayant une structure cfc et une aimantation perpendiculaire peuvent aussi être préparés sur d'autres bases de type cfc tels que des substrats de Pt. Les marches monoatomiques sur la surface du substrat sont exploitées afin de diriger le mode de croissance du film, ce qui permet ainsi de contrôler l'aimantation. Malgré d'importantes différences dans la morphologie et dans la structure des films de

Fe sur du Pt(111) plat et sur du Pt(997) en forme de marche, l'épaisseur critique pour la transition de la réorientation du spin est similaire dans les deux systèmes. Cependant, après une transition d'une structure cfc vers une structure ccc, et dans le cas d'une épaisseur de marche supérieure à trois monocouches, l'arrangement atomique local détermine l'axe facile d'aimantation dans le plan comme étant parallèle aux bords des marches.

Pour tous les systèmes de couches minces étudiés dans cette thèse, la contrainte épitaxiale représente l'une des forces motrices qui influencent la structure du film et déclenchent les transitions structurales. La dépendance de la morphologie et de l'aimantation en fonction de la déformation a été sondée à partir d'une étude comparative entre le Fe déposé à nu sur un substrat de Pt et le Fe déposé sur un substrat de Pt recouvert d'une couche de gaz noble. La formation de clusters de Fe sans contrainte lors de la désorption de la couche de Xe est favorisée en l'absence d'interaction entre la couche supérieure et le substrat. Les flagrantes différences dans l'anisotropie de l'aimantation entre les deux systèmes sont attribuées aux contributions magnéto-élastiques. Les mesures de la température de blocage des clusters de Fe permettent d'estimer la taille des clusters.

Tous les échantillons ont été analysés sous ultra haut vide. L'étude des propriétés magnétiques a été effectuée par des mesures d'effet Kerr magnéto-optique et par l'utilisation d'un microscope Kerr. La caractérisation structurale a été faite à partir de la diffraction d'électrons lents et par microscopie à effet tunnel en collaboration avec d'autres chercheurs.

Contents

Abstract	i
Version abrégée	iii
Introduction	1
1 Magnetism at ultrathin film limit	5
1.1 Magnetic anisotropy and spin reorientation	6
1.2 Correlation between the film morphology and the magnetism	11
1.3 Interaction between thin magnetic layers	14
2 Experimental setup and methods	25
2.1 The UHV system	27
2.1.1 The sample holder	28
2.1.2 The VT-STM	30
2.2 Magneto-optical measurements	32
2.2.1 Integral MOKE measurements	32
2.2.2 In-situ Kerr microscopy	35
2.3 Sample preparation	37
3 Temperature dependence of the magnetism of Fe/Cu(100)	41
3.1 Thermally-induced spin reorientation transition	42
3.2 Temperature dependence of the magnetization reversal process	49
3.2.1 Magnetic after-effect	49
3.2.2 The magnetization reversal process	53
3.2.3 Energy barriers and relaxation times	55
4 Coupled perpendicular magnetization in Fe/Cu/Fe trilayers	59
4.1 Fabrication of fcc-Fe/Cu/Cu trilayers	59
4.1.1 Bottom Fe layer of variable thickness	63

4.1.2	Top Fe layer of variable thickness	64
4.1.3	Cu spacer of variable thickness	67
4.2	Oxygen adsorption and spin reorientation	70
5	Structure and magnetism of ultrathin Fe films on Pt substrates	75
5.1	Growth of Fe on flat and vicinal Pt surfaces	76
5.1.1	3-D Fe islands on Pt(111)	76
5.1.2	Growth of Fe on Pt(997)	78
5.2	Magnetic properties of Fe on Pt substrates	79
5.2.1	Magnetism of Fe/Pt(111)	79
5.2.2	Magnetism of Fe/Pt(997)	81
5.2.3	Adsorbate induced shift of the Curie Temperature	83
6	Magnetism of Fe clusters on Pt surfaces	89
6.1	Buffer layer assisted growth of Fe clusters	90
6.2	Magnetic properties of clusters and films of Fe on Pt	92
6.2.1	Fe clusters	92
6.2.2	Epitaxial Fe films and strain effects	97
	Conclusions and perspectives	101
	Acknowledgements	105
	Bibliography	107
	Curriculum vitae	117
	Publications	119

Introduction

The fascinating magnetic behavior of some elements present in nature has been known since ancient Greece. However, it was the Chinese, more than 2000 years ago, who built what could be defined as the first magnetic device ever realized: the compass. Curiously, only in the 12th century people started to use it for navigation purposes. For a long time, the compass has been employed by the navigators to discover new continents and explore the world on very large scale. Nowadays, the interest of scientists working in the field of magnetism has turned towards the opposite direction, the infinitely small.

In particular, since the introduction of the first magnetic hard disk drive into a computer by IBM in the late 1950s, many efforts have been concentrated on the study of magnetic thin films because of their key role in magnetic recording and storage media. In recent magnetism-based and magneto-electronic devices, nanometer dimensions have already been reached. The rapidly decreasing dimensions demand investigations of magnetism at the atomic level. For basic research, films approaching a thickness of a single atomic layer are model systems for the investigation of physics in two dimensions. Magnetic properties such as ordering temperature, magnetic moment, magnetic anisotropy, etc., can be drastically different from those in three dimensional systems [1] and are deeply interconnected with the structural and morphological properties of the film as well as its interaction with the substrate. One of the main goals of the research on ultrathin epitaxial films is therefore to find a direct correlation between structure and magnetic properties at the atomic scale. The majority of experiments performed so far show that the observed phenomena are often unique to a particular combination of film and substrate, and principles of general relevance are rare [2, 3]. Moreover, in some cases the published results are partly contradictory, indicating that subtle deviations in the preparation condition, substrate quality, etc. can cause significant changes in the structure or magnetism. A deeper understanding of such a relationship is not only of basic interest but would allow tailoring of the magnetic properties of more complex structures for application in new devices. Being able to control the assembling of particular nanostructures (multilayers, films, wires, dots) of high quality (defect free,

smooth interfaces) with well defined magnetic properties represents the challenge for present and future efforts in the field of nanoscale magnetism. Various methods have been presented to control the growth and assembly of nanostructures at surfaces. Artificially built structures at the atomic scale have been done by manipulating adatoms or adsorbed molecules [4, 5]. On the other hand, nature can often help to do parallel assembling processes via self-organization. For instance, linear and two dimensional nanostructures [6], magnetic quantum dots array [7] and ferromagnetic monoatomic chains [8] can be obtained by proper choices of film/substrate system and growth conditions. However, despite the considerable progress and innumerable results on ultrathin films and nanostructures during the last decades, a full and general understanding of the correlation between structure, morphology and magnetic properties has not yet been achieved. One of the best examples of the complexity of this correlation is represented by the system Fe/Cu(100). Structural transitions (with increasing Fe thickness) from tetragonally distorted fcc to fcc and then to bcc have been correlated to different magnetic phases [9]. Despite the huge amount of work on this system [10–29], the correct picture is still under debate. One main reason for the discrepancy between results of different groups is that minor changes in the preparation conditions have significant impact on the obtained film morphology.

One major goal of this thesis is to identify the relevance of structure and morphology at the atomic level for magnetic properties, such as the magnetic anisotropy, domain wall pinning, coercivity or magnetic coupling. I will present an experimental approach to separate reversible and irreversible contributions to the anisotropy of thin films. Furthermore, I explore strategies to manipulate the crystallographic structure and morphology in more complex systems, such as ferromagnetic trilayers and surface supported 3D clusters. Structurally driven and adsorbate-induced changes of the magnetism have been investigated, in some cases even on the same film. The experiments described in this thesis therefore provide basic methods to steer the assembly of structures at the atomic level and may be useful for the construction of more complex layered structures or cluster assemblies.

In this thesis I focus on the following systems:

The magnetic properties of Fe/Cu(100) are investigated during and after thermally-induced morphological modifications. This approach has allowed the separation of reversible and irreversible contributions to the surface anisotropy constant, coercivity, Barkhausen length and domain wall propagation, as described in Chapter 3.

Such fcc-Fe layers have been used as templates to fabricate fcc-Fe/Cu/Fe trilayers. With each preparation step a spin reorientation transition has been observed, underlin-

ing the fundamental role of the interfaces for the magnetic properties of ultrathin films. Also the perpendicular ferromagnetic coupling between the two ferromagnetic Fe layers is governed by the interface roughness, as described in Chapter 4.

In Chapter 5, another model system to study the correlation between structure and magnetism is presented. The morphology and growth mode of Fe films on flat and stepped Pt substrates are determined by the presence of the substrate steps. The steps inhibit the formation of bcc(110)-domains in a particular orientation with respect to the substrate, resulting in a pronounced in-plane anisotropy with easy axis parallel to the step edges. Adsorbate experiments on all layered systems help to probe the role of the electronic structure at the film-vacuum interface for the magnetic anisotropy.

The film-substrate interaction during the growth of nanostructures is suppressed by covering the substrate surface with a noble gas buffer layer, as described in Chapter 6. Relaxed strain-free Fe clusters are formed during Fe deposition onto the buffer layer and, in particular, during the buffer layer desorption. Different magnetic anisotropy is found in the clusters compared to strained islands grown on the bare substrate.

The experiments show that already simple variations of the preparation conditions, substrate orientation or surface morphology yield a variety of different overlayer structures. A combination of methods presented here and other methods may pave the road towards more complex structures, such as three dimensional assemblies, in future experiments.

Chapter 1

Magnetism at ultrathin film limit

Ultrathin films and multilayers display distinct magnetic properties with respect to bulk materials [1]. Exciting phenomena such as perpendicular magnetization [9,30], enhanced magnetic moment [31, 32], modified magnetic anisotropy [33, 34] and magneto-elastic coefficient [35,36], reduced Curie temperature [37,38] have been observed by decreasing the film thickness down to the limit of a few atomic layers.

The magnetic properties are deeply related to the electronic and structural properties. The density of states around the Fermi energy, is a key parameter for magnetism according to the Stoner model. The bandwidth, the relative position to the Fermi energy and the exchange splitting of the relevant d-sub-bands determine the magnetic moment and the existence of long-range magnetic order, i.e. the ferromagnetic behavior. On the other hand, these parameters depend on the structure of the material. The width of the d-band sensitively depends on the atomic coordination, the interatomic distances and the localization. The magnetic properties will thus depend on the local structure. In epitaxial ultrathin films, the film-vacuum and film substrate interfaces strongly influence the magnetism [39]. In such a systems of reduced dimensionality, the atom coordination decreases. The smaller number of neighbors decreases the exchange interaction and, as a consequence, the stabilization of the magnetic ordering. The thermal fluctuations becomes relatively more important and, generally, the Curie temperature decreases with film thickness. The lowering of the symmetry at the surface removes the quenching of the orbital moment, which is also enhanced by the narrowing of the d-band due to the broken bonds at the film-vacuum interface [40]. The substrate plays an important role, as well. Epitaxial strain due to lattice mismatch modifies the structure of the adlayer. Phases with different magnetic properties, which exist in bulk only at very high temperature, such as fcc-Fe, can be found at room temperature in ultrathin films deposited on particular fcc-templates. Strongly interacting substrates with induced magnetic moment

substantially influence the magnetism of the adlayer, as well.

The aim of this chapter is providing the relevant basics for the experimental results presented in this thesis. The correlation between the structural properties and the magnetism of ultrathin films and nanostructures will be pointed out in Sec. 1.1 and 1.2. The magnetic coupling of two ferromagnetic layers through a non-magnetic spacer will be addressed in Sec. 1.3.

1.1 Magnetic anisotropy and spin reorientation

Applications of magnetic materials depend on the tendency of the magnetization to align along certain spatial directions. These preferred directions are called easy axis of magnetization and are determined by the minima in the magnetic anisotropy energy (MAE). The MAE is considered as the energy necessary to deflect the magnetization in a single crystal from the easy to the hard direction (given by the maxima in the MAE).

In the bulk as well as in thin films the magnetic ordering is provided by the long-range exchange interaction between neighboring moments. However, the stabilization of the total magnetization with respect to certain spatial directions is due to the magnetic anisotropy. The magnetic anisotropy determines the presence of magnetic domains and, in competition with the exchange interaction, the width of the domain walls. Within a magnetic domain, the magnetic moments are aligned along the easy magnetization axis, while a transition of the moment direction occurs in the domain wall separating two domains of different magnetization direction. The exchange interaction tries to keep the domain wall width large in order to minimize the angle between adjacent spins, whereas the magnetic anisotropy tends to reduce the width by forcing the spins along the easy magnetization axis. The domain wall width is given by $2\sqrt{A/K}$, where A is the exchange stiffness and K the anisotropy constant. In thin films, the former is smaller while the latter is usually found to be increased. As result, much smaller domain wall width is expected with respect to the bulk. We will see in Sec. 3.1 that this parameter determines the increasing of the coercive field in thin Fe layer grown at 120 K on Cu(100) when, upon annealing, the domain wall width matches the islands size.

Contribution to the magnetic anisotropy arise from both spin-orbit and dipolar interactions. In the following, two major contributions relevant for thin films will be considered: the magneto-crystalline anisotropy energy, E_{MC} , and the magneto-static anisotropy energy, E_{shape} .

Magneto-crystalline anisotropy

The spins interact with the orbital angular moments via the spin-orbit coupling:

$$H_{SO} = \xi \mathbf{S} \cdot \mathbf{L} \quad (1.1)$$

where ξ is the spin-orbit constant. This interaction is isotropic. However, in a crystal, the electronic orbitals are exposed to the inhomogeneous electric field produced by neighboring atoms, i.e. the crystal field. The resulting directional dependence of the 3d-electron orbitals interaction with the crystal field *and* the spin-orbit coupling are the origin of the magneto-crystalline anisotropy (MCA).

The idea that the MCA originates from the coupling between the isotropic spin moment and orbital angular momentum was first proposed by van Vleck [41]. Since ξ is usually much smaller ($\sim 50 \text{ meV}$) than the 3d-bandwidth ($\sim 1 \text{ eV}$), a perturbation approach within a tight binding model can be used to describe the relationship between the MCA and the orbital moment [42]. It has been shown that the E_{MC} is proportional to the difference between the orbital moments along the hard and easy directions. The latter is given by the direction in which the orbital moment is larger. Furthermore, the orbital moment is directly proportional to ξ and inversely proportional to the bandwidth, W [40]. Since the orbital moment direction is perpendicular to the plane of the orbiting electron, in case of thin films the in-plane and the out-of-plane orbital moments will be determined by the bandwidth of the out-of-plane and in-plane orbitals, respectively. More recently it has been shown that the E_{MC} is proportional to the orbital moment only when the majority spin band is completely filled (strong ferromagnets). Otherwise, also the magnetic dipole term, which accounts for the spin-flip contributions in the E_{MC} , has to be taken into consideration [43].

In a crystal, the 3d-electron orbitals are expressed in terms of standing waves, since they can adapt the charge distribution to the crystal field resulting thus electrostatically favorable. Standing waves are described by real wave functions, $|\psi\rangle$. The expectation value of the angular momentum component $L_z = \langle \psi | \hat{L}_z | \psi \rangle$ is zero. The orbital moment is said to be quenched. As a consequence, the orbital contribution to the magnetic moment is quenched, as well. Reducing the number of neighbors in thin film allows running wave orbitals, for which $L_z \neq 0$. As a result, the orbital magnetic moment and the magnetic anisotropy are enhanced. It is generally found that the smaller the coordination, the larger the orbital moment and the MCA [40, 44].

Because of the interaction between the orbitals and the crystal field, the magneto-

crystalline anisotropy reflects the symmetry of the crystal structure. In a phenomenological model, the MCA is assumed to be a function of the direction of the magnetization with respect to the crystallographic axis. Assuming cubic symmetry, the magneto-crystalline energy density can be expressed as:

$$f_{MC} = K_4(\alpha_1^2\alpha_2^2 + \alpha_2^2\alpha_3^2 + \alpha_3^2\alpha_1^2) + K_6(\alpha_1^2\alpha_2^2\alpha_3^2) + \dots \quad (1.2)$$

where K_4 and K_6 are the fourth and sixth order MCA constants, and α_i the cosines between the magnetization direction and the crystallographic axis. For iron, $K_4 = 4.2 \times 10^4 J/m^3$ and $K_6 = 1.5 \times 10^4 J/m^3$ [45]. The easy axis of magnetization are thus given by the [001], [010] and [100] crystallographic directions (Fig.1.1). The order of magnitude of the f_{MC} is typically $\sim 10^{-6} - 10^{-4} eV/atom$ for 3d-metals.

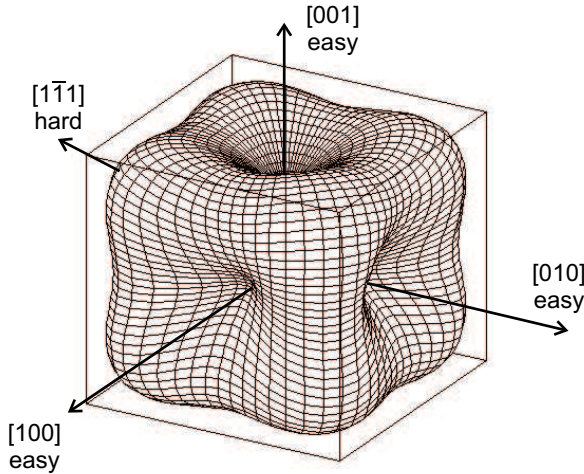


Figure 1.1: f_{MC} as a function of the crystallographic directions of a cubic lattice, in case of $K_4 > 0$. The minima and the maxima of f_{MC} indicate the easy and the hard magnetization axis, respectively.

When an external magnetic field is applied, the spins try to align parallel to the direction of the field. Due to the spin-orbit interaction, a rotation, and as a consequence a variation, of the orbital moment occurs. The re-alignment of the orbital moments changes the overlap of the electron orbits. Because of the Pauli principle, this modification costs energy, which, to some extent, can be compensated by lattice deformation. This effect is known as *magnetostriction*. In the phenomenological model described in the following it is considered as a separate magneto-elastic contribution to the MCA.

Magneto-static anisotropy

An additional contribution to the magnetic anisotropy originates from dipolar interactions. When the magnetic moments are all aligned in one direction, a magnetic stray field is produced outside the sample, due to the accumulation of magnetic charges. This surface charge distribution is the source of an internal demagnetizing field, acting in opposition to the magnetization that produces it (Fig. 1.2). The demagnetizing field,

\mathbf{H}_d , depends on the shape of the sample. As a consequence, the magneto-static energy becomes dependent on the magnetization direction, determining the magneto-static or shape anisotropy energy density:

$$f_{shape} = -\frac{1}{2} \mu_0 \mathbf{H}_d \cdot \mathbf{M} = \frac{1}{2} \mu_0 M^2 (N_a \alpha_1^2 + N_b \alpha_2^2 + N_c \alpha_3^2) \quad (1.3)$$

where $\mathbf{H}_d = -\mathbf{N} \cdot \mathbf{M}$, being \mathbf{N} the demagnetizing tensor. It is $N_a + N_b + N_c = 1$, with $N_c = 1$ in case of thin films. In this case, the shape anisotropy will thus favor in-plane magnetization to avoid magnetic stray field. Such a field in films with perpendicular magnetization is reduced by the formation of magnetic domains. However, the formation of magnetic domains costs both exchange and anisotropy energy because in the domain walls the spins are neither parallel nor aligned along an easy axis.

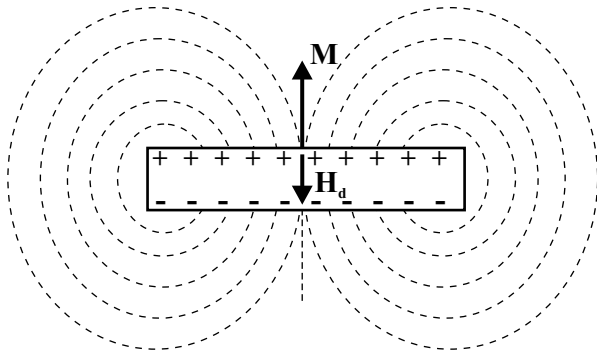


Figure 1.2: Stray field lines for a sample with out-of-plane magnetization. At the surface, magnetic charge of opposite sign are accumulated, giving rise to a demagnetizing field within the sample.

no surface poles are generated. As a consequence, the stray field energy of ideally flat ultrathin films is negligible. However, defects and imperfections in the morphology will result in a stray field outside monolayer thin films. It will be shown in Sec. 1.3 that the roughness is associated with a stray field, which determines a magneto-static interlayer coupling.

Spin reorientation transition in thin films

The magnetic anisotropy in thin films can be markedly different from the respective bulk materials. Interface effects such as modified electronic structure, interlayer relaxation, surface strain, reduced coordination, etc. can alter the magnetic properties.

The presence of domains is thus given by the balance between the gain from the reduced stray field and the energy cost for the domain walls formation. For a perpendicular magnetized film, it was shown that the sum of domain wall energy and magneto-static energy scales as $1/t$ for a single domain configuration and as $1/\sqrt{t}$ for a multi-domain state, being t the film thickness. Hence, below a critical thickness, a single domain configuration prevails [46]. This prediction is supported by the intuitive argument that for $t \rightarrow 0$, also the volume vanishes and thus

Their influence increases with decreasing the film thickness. The often observed perpendicular easy magnetization axis is determined by the interface effect contributions to the MAE, which dominate over the magneto-static energy in the ultrathin limit. A spin reorientation transition (SRT), i.e. a change in the direction of the magnetization easy axis, is often observed in thin films by varying the film thickness, t_F . A rather simple phenomenological model is often used to describe this transition. The total anisotropy energy density, f_{tot} , can be written as the sum of the magneto-crystalline, f_{MC} , the magneto-elastic, f_{ME} , the magneto-static, f_{shape} , energy densities and a surface contribution, f_{surf} , which takes into account of all the interface effects. In the case of lattice with cubic symmetry, neglecting terms higher than the fourth order, and assuming homogeneous in-plane, ε_{\parallel} , and perpendicular, ε_{\perp} , strain, we can write:

$$f_{tot} = K_4(\alpha_1^2\alpha_2^2 + \alpha_2^2\alpha_3^2 + \alpha_3^2\alpha_1^2) + B_1[\varepsilon_{\perp}\alpha_3^2 + \varepsilon_{\parallel}(\alpha_1^2 + \alpha_2^2)] + \frac{1}{2}\mu_0 M^2 \alpha_3^2 - \frac{(K_{f-vac} + K_{f-sub})}{t_F} \alpha_3^2 \quad (1.4)$$

where B_1 is the magneto-elastic coupling constant, K_{f-vac} and K_{f-sub} the surface anisotropy constant for the film-vacuum and film-substrate interface, respectively. A negative sign of B_1 indicates that the energy is lowered with the magnetization along the direction of tensile strain, if the strain is large enough to dominate over the other anisotropy contributions. This aspect will be discussed in Chapter 6, in which the magnetic properties of strained Fe islands are compared with relaxed Fe clusters on the same Pt substrate. The surface anisotropy constants account for the interface effects. Often, for simplicity, $K_{f-vac} = K_{f-sub} = K_S$ is assumed.

The difference between the magnetic anisotropy energy calculated with the magnetization perpendicular ($\alpha_3 = 1, \alpha_1 = \alpha_2 = 0$) and within the plane ($\alpha_1 = 1, \alpha_3 = \alpha_2 = 0$) provides the information about the easy axis of magnetization:

$$\Delta f_{tot} = f_{tot}(\perp) - f_{tot}(\parallel) = B_1(\varepsilon_{\perp} - \varepsilon_{\parallel}) + \frac{1}{2}\mu_0 M^2 - \frac{(K_{f-vac} + K_{f-sub})}{t_F} \quad (1.5)$$

If $\Delta f_{tot} > 0$, the magnetization will be within the film plane, otherwise for $\Delta f_{tot} < 0$ the preferred direction will be out-of-plane. At low thickness, f_{surf} can dominate over the other contribution, thus determining the easy axis of magnetization. A positive value of $K_{f-vac} + K_{f-sub}$ will favor perpendicular easy axis. A change in sign of Δf_{tot} as a function of t_F indicates a SRT (Fig.1.3). The critical thickness, t_{crit} , can be calculated from $\Delta f_{tot} = 0$:

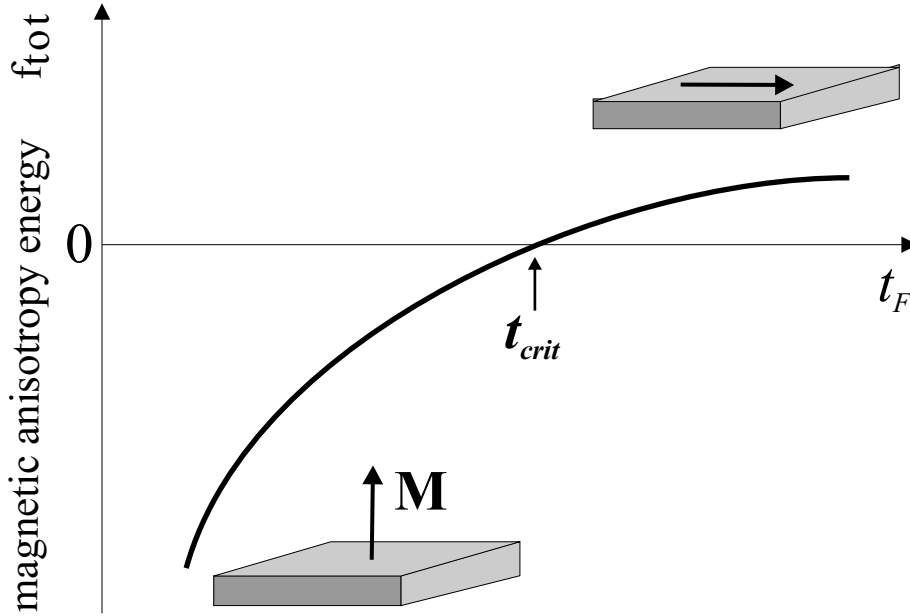


Figure 1.3: Difference between the total magnetic anisotropy energy with perpendicular and in-plane magnetization as a function of film thickness. A change of sign indicates the critical thickness for the spin reorientation transition from out-of-plane to in-plane.

$$t_{crit} = \frac{2(K_{f-vac} + K_{f-s})}{2B_1(\varepsilon_{\perp} - \varepsilon_{\parallel}) + \mu_0 M^2} \quad (1.6)$$

The shift of t_{crit} as a function of temperature observed on ultrathin Fe films grown on Cu(100) will be attributed to a temperature dependence of K_S . By using the Eq. 1.6, reversible and irreversible contribution to K_S will be calculated (Chapter 3). Furthermore, the reorientation transition observed on Fe/Cu/Fe/Cu(100) trilayers by oxygen adsorption on the top Fe layer will be ascribed to a change of K_S due to the modified electronic structure at the Fe-vacuum interface. This result will demonstrate the governing role of the top Fe layer for the magnetism of the whole trilayer (Chapter 4). The importance of the film-substrate interface will be instead addressed in Chapter 5 for Fe films on flat and stepped Pt substrates.

1.2 Correlation between the film morphology and the magnetism

The observation of the evolution of magnetism with structural and morphological changes on the same film/substrate system is very instructive to identify the governing parameters for the magnetism. It will be shown in Chapter 3 that changes in the mag-

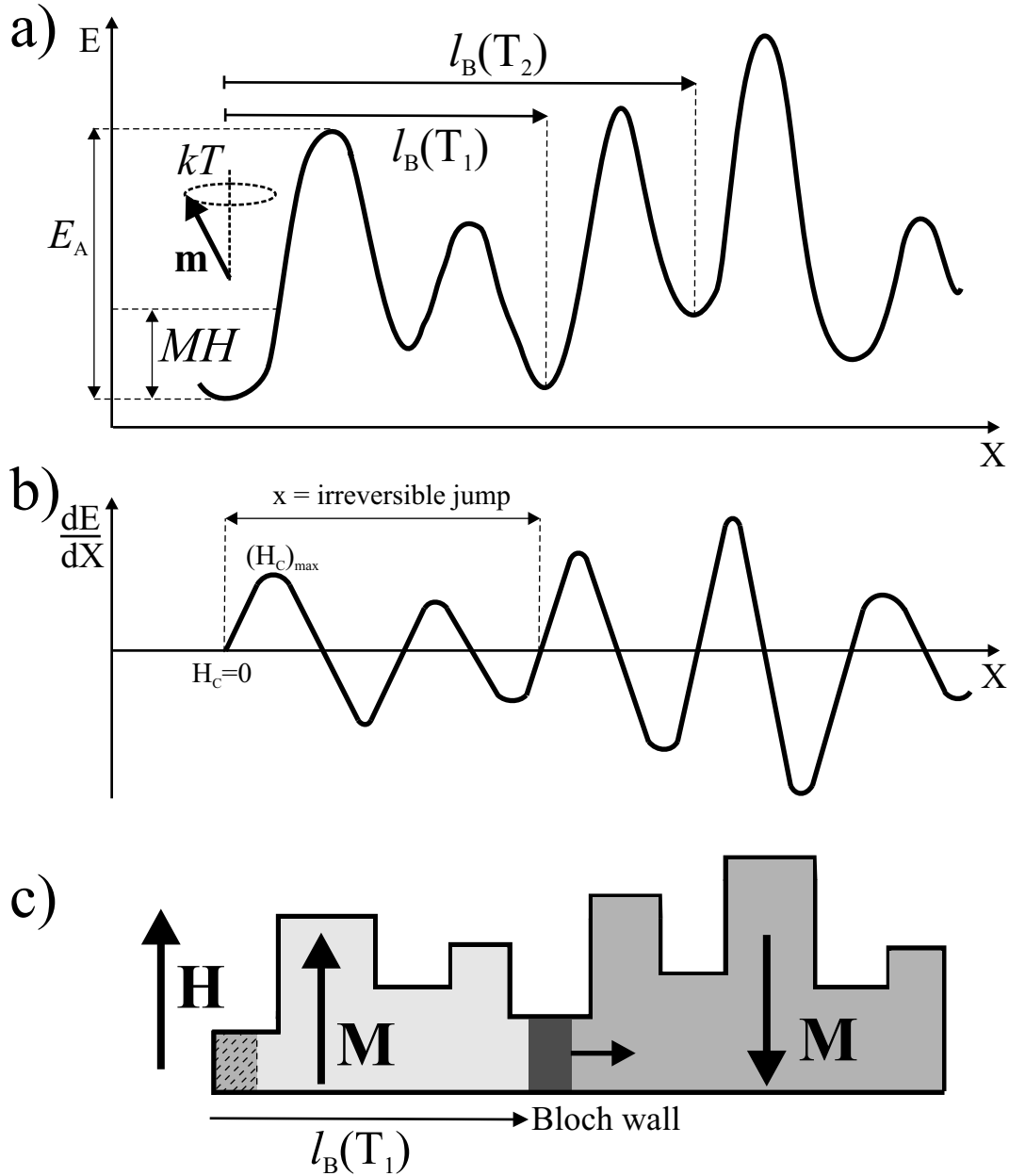


Figure 1.4: Schematic representation of the potential energy surface in 1D. Barkhausen lengths at different temperature are indicated ($T_1 < T_2$). Domain walls move between local minima of the PES.

netic properties, such as anisotropy, coercivity and domain wall motion, are correlated with thermal-induced modification of the morphology of ultrathin Fe films grown at 120 K on Cu(100).

The magnetization reversal process in ultrathin films is determined by the energy of the domain walls as a function of position. It starts with the nucleation of small domains of opposite magnetization at places of reduced anisotropy within an external field and proceeds by domain wall propagation. For an idealized perfectly smooth

and homogeneous film, the domain wall displacement requires only little field energy. In epitaxial films, various effects originating in deviations from the ideal crystalline structure interact in a complex manner and determine the shape of a more or less statistical, irregular Potential Energy Surface (PES) (Fig. 1.4(a)). The dominating contributions to the PES arise from exchange and anisotropy inhomogeneities [47, 48], which are on the other hand directly related to the structure and morphology of the film. The field needed to reverse the magnetization, i.e. the coercive field H_C , is proportional to maxima of the gradient of the PES, $(dE/dx)_{max}$, averaged over the entire sample (Fig. 1.4(b)):

$$H_C \sim \sqrt{\left(\frac{dE}{dx}\right)_{max}^2} \quad (1.7)$$

As we will see in the following, other important magnetic properties, such as the Barkhausen volume, follow directly from the distribution of energy barriers in the PES. The PES thus provides the central link between film structure and magnetism.

A domain wall is pinned at a position of a local energy minimum, usually associated with structural peculiarities (Fig. 1.4(c)). Moving away a domain wall from a pinning center costs energy and overcoming the barrier requires the activation energy, E_A . Both the temperature *and* the applied field decrease the effective barrier height. While the field actually decreases the height, the temperature increases the attempt rate of the spins to overcome the barrier. If the provided energy is sufficiently high, the domain wall jumps (Barkhausen jump) to the next higher barrier, in another local minimum of the PES (Fig. 1.4(b)). The magnetization reversal process depends therefore on the PES, the applied field and the temperature. As a consequence, experiments on the magnetization reversal process as a function of field *and* temperature yield valuable information about the PES as will be demonstrated on the example of Fe films on Cu(100) in Sec. 3.2.

Because of the PES, the magnetization reversal is represented by discrete jumps of the total magnetization, M , as the applied field, H_{ext} , is smoothly increased. The smallest volume which reverses its magnetization in a single activation event is called Barkhausen volume [49]. These irreversible changes in the magnetization are the result of irreversible domain wall motions from different pinning sites (Fig. 1.4). The jump can at finite temperature even if the applied field is lower than H_C . This relaxation of the magnetization at constant applied field is referred to as magnetic after-effect. It determines the long-term stability of magnetic storage media and it is thus of great relevance in applications [50]. Moreover, it underlines the importance of the attempt rate in overcoming the energy barriers for the magnetization reversal, beyond the energy

provided by the applied magnetic field.

Measurements of the magnetic after-effect, also dubbed as magnetic viscosity, have turned out to be very helpful for the investigation of activation events. Such experiments have been performed on thin films with perpendicular [51–57] and in-plane magnetization [48, 57]. The interpretation of the results could be improved substantially by the combination with magnetic imaging techniques, such as Kerr microscopy [53, 55–57] or spin sensitive scanning electron microscopy (SEMPA) [48]. Thus, domain nucleation and wall propagation dominated magnetization reversal could be distinguished [53, 54, 57, 58], as predicted by Fatuzzo’s theory [59]. In some cases the experiments allow to estimate the Barkhausen volume, V_B [51, 54–56], or E_A [48, 51, 52, 56]. The importance of domain pinning mechanisms [57], roughness [51, 60] or preparation conditions [55] has been pointed out. The theoretical description of the observed data could significantly be improved by assuming distributions of E_A or V_B rather than constant values [51, 54]. However, temperature dependent measurements of the magnetic after-effect and the anisotropy allow to improve the understanding of the correlation between film structure and magnetism and yield the determining parameters for the Barkhausen volume, and thus for the PES. The distribution of the relaxation times as equivalent of the energy barrier will be obtained from such experiment on ultrathin Fe films grown at LT ($\sim 120K$) on Cu(100) (Sec. 3.2).

1.3 Interaction between thin magnetic layers

The magnetic coupling between ferromagnetic (FM) layers separated by a non-ferromagnetic spacer has been investigated extensively in the past [61–67]. While systems with in-plane magnetic anisotropy are common and have attracted the interest of many scientists, studies on trilayers with coupled *perpendicular* magnetization are rare [68, 69]. However, such systems might be of particular relevance for giant magnetoresistive or magneto-optical applications [70].

The oscillatory character of the coupling as a function of interlayer thickness observed on many systems can be described by an extension of the theory of the Ruderman-Kittel-Kasuya-Yosida (RKKY) exchange interaction through the non-magnetic spacer [71, 72]. However, other possible coupling mechanisms arising from the particular morphology of the interfaces, such as the magneto-static interaction, do influence the magnetic coupling. This contribution, also known as ”orange peel” coupling, was investigated by Néel more than 40 years ago in case of in-plane magnetic anisotropy [73]. It was shown that a correlated roughness of the interfaces results in a FM configuration of

the magnetizations in the two magnetic layers. For systems exhibiting perpendicular magnetization, the contribution to the coupling arising from magneto-static interaction has been seldom discussed only in very few cases [74].

Epitaxial Fe layers grown at RT on Cu(100) substrates exhibit interesting magnetic phases in the ultrathin film limit [15,75,76], in particular the appearance of perpendicular magnetization below a thickness of ~ 11 ML [9], which is commonly attributed to the contribution of the Fe-vacuum interface to the magnetic anisotropy energy [77]. Because of their perpendicular anisotropy and the layer-by-layer growth mode on Cu(100), ultrathin Fe layers grown at RT on Cu(100) represent an ideal template for the fabrication of Fe/Cu/Fe trilayers to investigate the magnetic coupling in systems with perpendicular magnetization. Our experimental results are reported in Chapter 4.

In the following, an introduction to the two coupling mechanisms, the interlayer exchange and magneto-static interaction, is given. Concerning the first one, the case of two FM layers separated by a non-magnetic spacer is considered. Afterwards, a model to estimate the magneto-static interaction in case of perpendicular anisotropy is described.

Interlayer exchange coupling

The first observation of antiferromagnetic (AF) coupling between Fe layers separated by a Cr spacer [61] stimulated an intensive research on the coupling phenomena in multilayer systems. It has been shown that the spectacular result of oscillatory FM-AF coupling as a function of the interlayer thickness, D , occurs almost independently of the transition metal used as spacer [63].

The interlayer exchange coupling (IEC) can be described as a quantum interference effect arising from multiple spin dependent reflections of the electrons at the interfaces between FM layers and spacer layer [67], similarly to the Ruderman-Kittel-Kasuya-Yosida (RKKY) interaction between magnetic impurities in a non-magnetic host [78–80]. In case of constructive or destructive interference of the electron wave functions, the density of states in the spacer is enhanced or decreased, respectively. As a consequence, also the energy of the system will change depending on D . For certain values of D , the most energetically favorable configuration will be the parallel alignment of the magnetization of both FM layers (FM coupling) and for other ones, antiparallel alignment (AF coupling). A derivation of the IEC is obtained by using the Green's function formalism. It can be shown that the IEC is mainly determined by the Green's function of the non-magnetic layer, which describes the propagation of electrons between the two FM layers, *and* the spin dependent reflectivity at the FM layers-spacer interfaces, which is different for majority or minority electrons. The reflection of electrons with a given spin is dependent

on the matching of the spacer band structure with the majority and minority spin bands in the FM layer. Therefore, it appears clear that the spacer electronic properties and thickness influence the period of the oscillatory IEC, whereas the FM layers determine only the amplitude (coupling strength) and the phase shift of the oscillations. The IEC depends weakly on the FM layer thickness, t_{FM} . The amplitude of the IEC oscillations as a function of t_{FM} is generally much smaller than the oscillations as a function of D , and does not give rise to a change of sign of the IEC. For particular \mathbf{q} -vectors, the electrons are totally reflected at the interfaces and the amplitude and the phase shift of the IEC oscillations are independent of t_{FM} .

The magnetic coupling energy as a function of the angle ϑ between the magnetizations of the two FM layers is described by:

$$E_{IEC} = -J_1 \cos \vartheta \quad (1.8)$$

where J_1 is the so-called "bilinear" interlayer (or indirect) exchange coupling (IEC) constant. Depending on its sign, parallel ($J_1 > 0$) or antiparallel ($J_1 < 0$) alignment of the magnetizations occur.

In the limit of large D , an asymptotic approximation of J_1 can be derived:

$$J_1 = \sum_c \frac{A_c}{D^2} \cos(q_c D + \delta_c) \quad (1.9)$$

where A_c is the coupling strength of the various oscillatory components and is related to the reflection asymmetry of the majority and minority spins. The IEC depends on D as $\frac{1}{D^2}$ times a periodic function of $q_c D$, with the period determined by the reciprocal vectors q_c . It can be demonstrated that only the extremal spanning vectors of the Fermi surface perpendicular to the interface contribute to the IEC. The sum in Eq. (1.9) is therefore done considering only these particular \mathbf{q} -vectors, labelled by the index c . Fig. 1.5 shows a cross-section of the Fermi surface of Cu along the $(1\bar{1}0)$ plane passing through the origin. For the (001) orientation, two stationary spanning vectors are found. Hence, two different periods for the oscillatory IEC are predicted.

This asymptotic approximation leads to a good agreement with experimental data also for very thin spacer thickness, except when the two layers are in direct contact. However, the theoretical description of the IEC in terms of quantum interferences due to electron confinement provides satisfactory predictions only for the periods of the oscillations, while it usually fails in calculating the strength and the phase of the coupling. This is due to the poor description of the interaction (contact interaction) between the

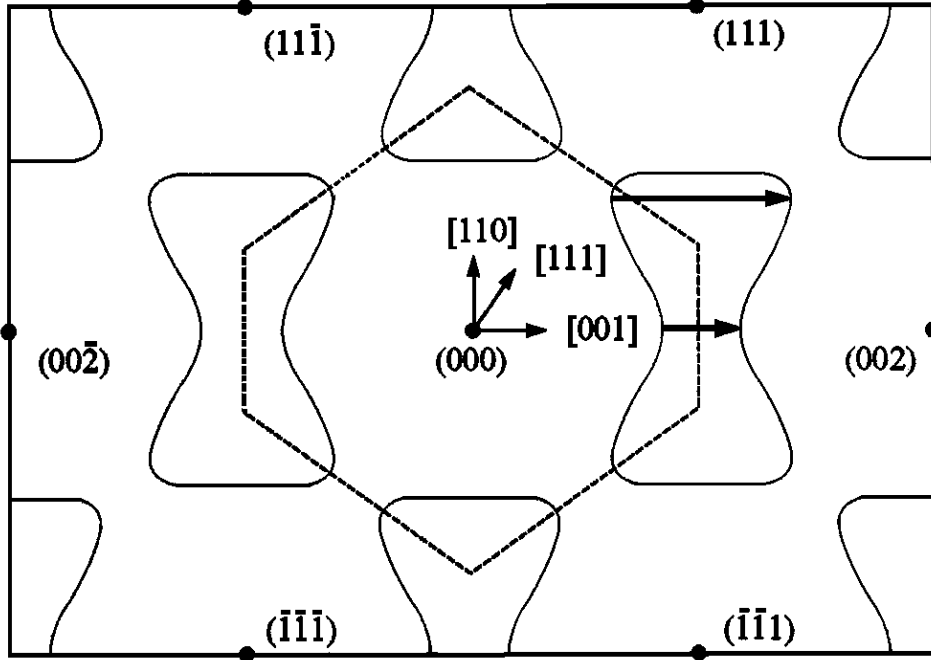


Figure 1.5: Cross section of the Fermi surface of Cu along the $(1\bar{1}0)$ plane passing through the origin. The indicated spanning vectors determine the periods of the IEC for layers with (001) orientation.

d -electrons of the FM layers and the conduction electrons. The model based on the concept of "virtual bond state" [81] has been extended to the case of 2D-FM layers [82]. Here, the d -electrons of the FM layer and the conduction electrons of the spacer are coupled via the so-called $s - d$ hybridization. This approach provides an interpretation of the period, phase, and intensity of the oscillatory IEC.

The "bilinear" coupling discussed so far favors either FM or AF coupling between the two FM layers. To interpret non-collinear magnetization state observed experimentally [83, 84], it is useful to expand E_{IEC} in a phenomenological series:

$$E_{IEC} = -J_1 \cos \vartheta + J_2 \cos^2 \vartheta + J_3 \cos^3 \vartheta \dots \quad (1.10)$$

where J_2 is the "biquadratic" term which, if negative, favors also 90° coupling. Experimentally, only $J_2 < 0$ has been observed [85]. Usually, J_1 is much larger than J_2 and thus often governs the spin configuration. However, for particular systems, as for example Fe/Cr/Fe on GaAs(100) [83] or NiFe/Cu multilayers [84], J_2 is not negligible and actually determines a non-collinear magnetic state.

The origin of J_2 was proposed by Slonczewski and attributed to two different mechanisms. At the FM layers-spacer interfaces localized-electron states with unpaired spin

are present. The spins are weakly coupled (loose spins) to the remainder of the ferromagnets and mediate a non-Heisenberg exchange coupling between them which includes a biquadratic term [86]. According to this model, the biquadratic coupling should be considered intrinsic to the ideal multilayer structure rather than due to impurities or structural defects. Successively, it was found that the "loose spins" are probably FM atoms (defects due to intermixing) in the spacer very close to the interface [87]. The second mechanism is ascribed to thickness fluctuations (roughness) of D , and the fact that the intrinsic J_1 oscillates as a function of D [87].

Perfectly flat and smooth interfaces and defect-free spacer are an ideal case. A certain

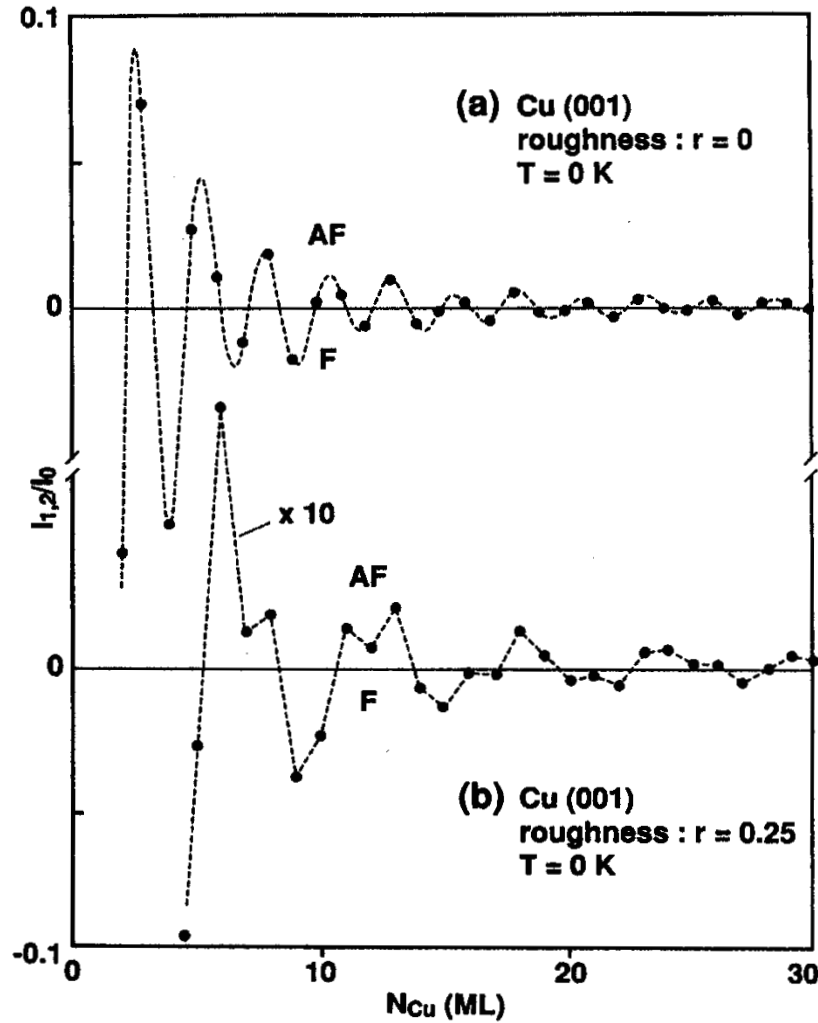


Figure 1.6: Calculated interlayer coupling constant J_1 (in the reference is called $I_{1,2}$) for a Cu(001) spacer, as a function of the Cu thickness N_{Cu} , at $T = 0 K$. The solid circles correspond to physically achievable thickness (N_{Cu} integer). (a) Zero roughness and (b) roughness $r = 0.25$. Figure from ref. [71].

degree of roughness and some intermixing are very often present and may influence, more or less strongly, the IEC. This effect was studied by Bruno *et al.* [71] and Levy *et al.* [88]. On one hand, the coupling must be averaged over the fluctuations Δz of the spacer thickness. Coupling oscillations with a period shorter than Δz are smoothed out. On the other hand, the in-plane translational invariance is broken. The coupling is suppressed for D larger than the lateral correlation length of Δz . As example, let assume an average D of N layers and portions of $N - 1$, N , $N + 1$ layers ($\Delta z = \pm 1$) with weights of r , $1 - 2r$ and r , respectively. In case of a roughness parameter $r = 0.25$, the short period oscillations are almost suppressed, resulting in a strongly reduced coupling strength (by a factor 10!) and an apparent increased period [71, 89]. These results are illustrated in Fig. 1.6 in case of zero roughness (a) and a roughness $r = 0.25$ (b). At $T = 0 K$ and for a Cu thickness $D = 5$ ML, for the case of flat interfaces, $J_1 \simeq 0.16 \text{ meV/atom}$ has been calculated. This value is in good agreement with the experimental result obtained from ex-situ measurements on 60 ML Cu/3 ML Fe/ x -Cu/3 ML Fe/Cu(100) [68]. In case of AF coupling, two minor hysteresis loops appear, shifted with respect to the $H = 0$ -axis. The strength of the IEC was estimated by using $J = M_S H_S t / 2$, being M_S the saturation magnetization, t the Fe layer thickness and H_S the saturation field taken at

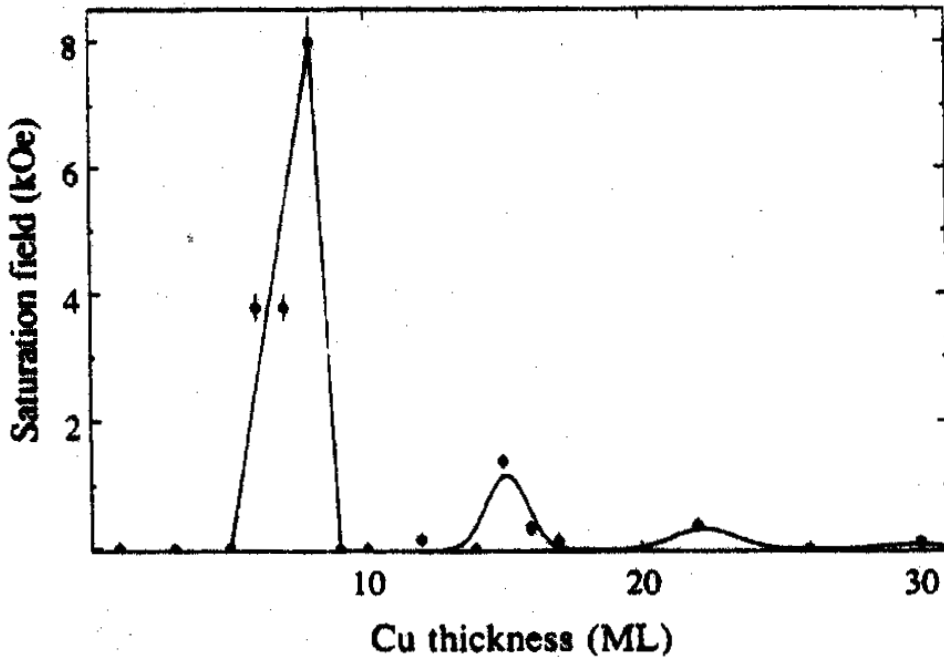


Figure 1.7: The saturation field, H_S , in epitaxial fcc-60 ML Cu/3 ML Fe/ x -Cu/3 ML Fe/Cu(100) structures as a function of the Cu spacer thickness, x . The solid line is a guide to the eye. Figure from ref. [68]

the center of the loops. A maximum exchange coupling energy $J \simeq 0.13 \text{ meV/atom}$ was obtained from the saturation field shown in Fig. 1.7. Unfortunately, this technique does not provide any information of J if the coupling becomes ferromagnetic.

Magneto-static or "orange peel" coupling

Besides the reduction of the IEC, the interface roughness gives rise to an additional interaction between the FM layers of magneto-static nature. A model to evaluate the "orange-peel" coupling for systems exhibiting *perpendicular* anisotropy was proposed only very recently to explain the experimental results on spin-valves comprising (Pt/Co) multilayers [74]. A correlated in-phase roughness described by a cosine waviness is assumed (Fig. 1.8). For large wavelength T with respect to the peak-to-peak amplitude $2h$, the angle θ between the surface normal and the vertical direction z takes the form:

$$\theta(x) = hp \cos px = \theta_0 \cos px \quad (1.11)$$

with $p = \frac{2\pi}{T}$ and $\theta_0 = hp$. The local anisotropy axis is assumed parallel to the surface

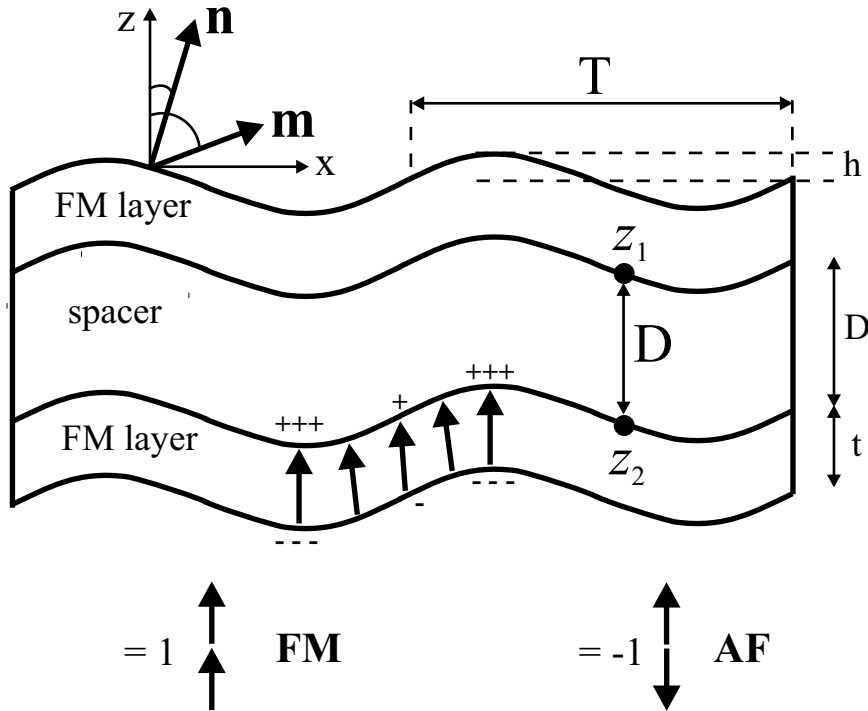


Figure 1.8: Schematic picture of a trilayer with rough interfaces. The positive and negative signs indicate the magnetic charges.

normal. The angular variation of the magnetization direction with respect to the z -axis can be described by $\psi(x) = \psi_0 \cos px$, where ψ_0 must be calculated by minimizing the total energy of the system with respect to ψ_0 . Neglecting the IEC, the total energy is given by the sum of the exchange energy, the uniaxial anisotropy energy and the magneto-static energy, as was explained in Sec. 1.1. The first two can be calculated per surface unit as follows:

$$f_{ex} = \frac{2t}{T} \int_0^T A \left(\frac{\partial \psi}{\partial x} \right)^2 dx = At p^2 \psi_0^2 \quad (1.12)$$

$$f_{ani} = -\frac{2tK}{T} \int_0^T \cos^2(\theta(x) - \psi(x)) dx = Kt(\theta_0 - \psi_0)^2 \quad (1.13)$$

where A is the exchange constant, K the uniaxial anisotropy constant and t the film thickness of the FM layers. To calculate the magneto-static energy, the magnetic charges at the interfaces, σ_s , and within the FM layers, σ_v , have to be considered:

$$\sigma_s = \vec{m} \cdot \vec{n} = M \cos[(\theta_0 - \psi_0) \cos px] \approx \sigma_0 - \sigma_1 \cos 2px \quad (1.14)$$

$$\sigma_v = \sigma_2 \sin px \quad (1.15)$$

with $\sigma_0 = M[1 - \frac{(\theta_0 - \psi_0)^2}{4}]$, $\sigma_1 = \frac{M}{4}(\theta_0 - \psi_0)^2$, and $\sigma_2 = pM\psi_0 t$, respectively. The σ_v is approximated to a surface charge in the middle of the FM layers because of very low thickness. The magneto-static energy per surface unit can thus be deduced from the magneto-static potential generated by these surface charge densities and is given by the following expression:

$$f_{shape} = \frac{\mu_0}{2} \left[-\epsilon \frac{\sigma_1^2}{8p} \exp(-2pb) [1 - \exp(-2pt)]^2 + \epsilon \frac{\sigma_2^2}{4p} \exp(-p(b+t)) + \sigma_0^2 t - \frac{\sigma_1^2}{4p} \exp(-2pt) \right] \quad (1.16)$$

where D is the spacer layer thickness. The total energy $f_{tot} = f_{ex} + f_{ani} + f_{shape}$ is then minimized with respect to ψ_0 for both FM ($\epsilon = 1$) and AF ($\epsilon = -1$) configuration, yielding the equilibrium magnetic distortion $\psi_0(\epsilon = \pm 1)$ and energy for the two cases. The preferred magnetic configuration is thus given by the sign of:

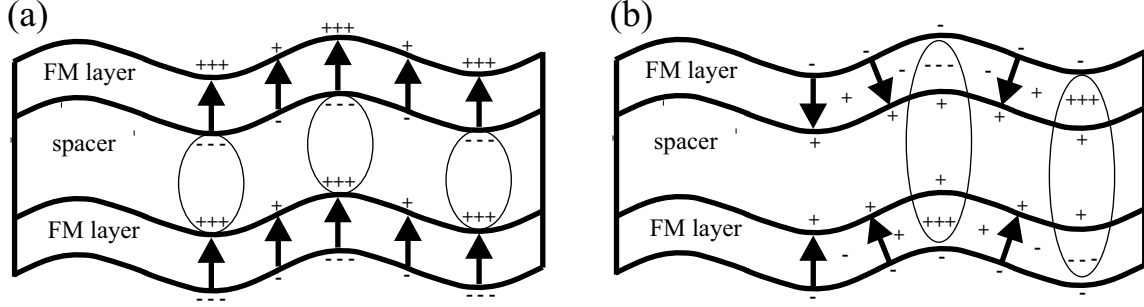


Figure 1.9: (a) Orange peel coupling in the case of weak anisotropy. The magnetization is along the z axis. For FM coupling between the magnetic layers magnetic charges of opposite sign appear at the interfaces. (b) In the case of strong anisotropy, the magnetization is along the surface normal. A lower magneto-static energy is obtained for AF coupling between the magnetic layers (volume charges of opposite sign fronting each other).

$$\Delta f_{tot} = f_{tot}(\psi_0(\epsilon = 1)) - f_{tot}(\psi_0(\epsilon = -1)) \quad (1.17)$$

If $\Delta f_{tot} > 0$, the magnetic coupling favors antiparallel alignment of the magnetizations, otherwise, for $\Delta f_{tot} < 0$, a FM configuration is found. As expected, for flat interfaces ($T \rightarrow \infty$, $h = 0$) the f_{shape} , and as a consequence the f_{tot} , is independent of ϵ , i.e. there is not a preferential FM or AF configuration of the magnetization.

Two special cases are discussed in the following. For very weak anisotropy, the magnetization is uniformly parallel within the FM layer because of the exchange stiffness and to reduce the charge density (Fig. 1.9(a)). The lowest magneto-static energy is obtained for parallel magnetization in the two FM layers, when an accumulation of opposite charges at the interfaces appears. The situation is different in case of very strong anisotropy (Fig. 1.9(b)). Here the magnetization always points along the surface normal. Hence σ_s is uniform and generates no coupling, whereas σ_v oscillates. Opposite large volume charges in the two FM layers, and thus reduced f_{shape} , are obtained in case of antiparallel alignment of the magnetizations. Hence, depending on the value of the magnetic anisotropy energy, the magneto-static interaction can lead to an oscillatory magnetic coupling. Differently from what was described previously on the IEC, here the sign of the coupling is more likely dependent on the FM layer thickness rather than on the spacer thickness.

Since in epitaxial films flat interfaces rarely exist, the magnetic coupling is determined by the interplay of *both* the interlayer exchange and magneto-static interaction. If the roughness is such that the strength of the magneto-static interaction becomes larger

than the IEC and thus dominates the coupling, no oscillations between FM and AF configuration of the two magnetic layers are observed as a function of the spacer thickness. The absence of interlayer coupling in Co/Cu/Co trilayers was indeed ascribed to interface roughness [90], which strongly influences also the coupling mechanism in Co/Cu(100) superlattices [91]. More recently, non-collinear magnetization in Fe/Cr/Fe trilayers [92] and strong magneto-static interaction in magnetic tunnel junctions [93] have been also attributed to the surface roughness. It will be shown in Chapter 4 that the interface roughness influences the magnetic coupling in fcc-Fe/Cu/Fe trilayers which was found to be dominated by the magneto-static interaction.

The assumption of correlated roughness described by a cosine waviness is obviously a simplification. However, it's useful to estimate the order of magnitude of the magneto-static interaction and make a comparison with the maximum value of the IEC calculated by Bennett *et al.* from the experiments on 60 ML Cu/3 ML Fe/x-Cu/3 ML Fe/Cu(100) [68] (see previous subsection). Let's consider a fcc-Fe/Cu/Fe trilayer formed by two Fe layers and a Cu spacer of the same thickness, $t = D = 3$ ML and assume a peak-to-peak amplitude of the cosine waviness of 2 ML ($h = 1$ ML) and a period $T = 50$ ML ~ 9 nm. Furthermore, the case of weak anisotropy for which a FM configuration is preferred ($\epsilon = 1$) and the fluctuations in the magnetization are zero ($\psi_0 = 0$) is assumed. A magneto-static energy $f_{shape} \simeq 1 \times 10^{-7}$ J/cm² is thus calculated. As we will see in Chapter 4, both Fe layers grow pseudomorphically, hence we can consider the atomic surface density of the Cu(100) ($\delta_{surf} = 1.53 \times 10^{15}$ atom/cm²) in order to find $f_{shape} \simeq 0.4$ meV/atom. This value is larger than 0.13 meV/atom, i.e. the IEC calculated by Bennett *et al.*, underlining the importance of magneto-static interaction for the magnetic coupling in trilayers and multilayers in case the presence of interface roughness.

Chapter 2

Experimental setup and methods

When the physics is studied at atomic level, any interaction with the external world can drastically change the electronic, chemical and magnetic properties of the system under investigation. This is the reason why experiments on nanostructures are often carried out in ultra high vacuum (UHV) systems, in which contamination with atmosphere gases are reduced due to the very low pressure ($< 10^{-10} \text{ mbar}$). Nevertheless, until the middle of 90s, most of the studies of the magnetic properties of thin film and nanostructures were performed ex-situ. The samples were prepared in UHV chamber equipped with the standard tools for substrate preparation, film deposition and structural characterization, and afterwards were transferred to a different system for the investigation of the magnetic properties. Before the transport, the samples were covered with a capping layer to protect them and avoid contaminations. Dielectric antireflection coating were often used to enhance the contrast [94, 95] for magnetic domain imaging. In-situ experiments and studies of adsorbate effects on thin films showed that properties such as the Curie temperature, the coercive field and the magnetic anisotropy are extremely sensitive to modifications of the electronic structure at the film-vacuum interface. In other words, the magnetic properties can be altered by the presence of a capping layer and in-situ experiments often give different results compared to ex-situ measurements. Hence, for basic research, it is mandatory to perform the experiments directly in-situ. Studying the structure, morphology and magnetism in-situ on one and the same film is crucial to make a correlation between structure and magnetic properties. For all the experiments described in this thesis, it has been used a UHV system equipped with tools for sample preparation, structural and morphological characterization and investigation of the magnetic properties. This system was built within this PhD project. Details of the UHV system and the experimental methods used for the experiments are described in this chapter.

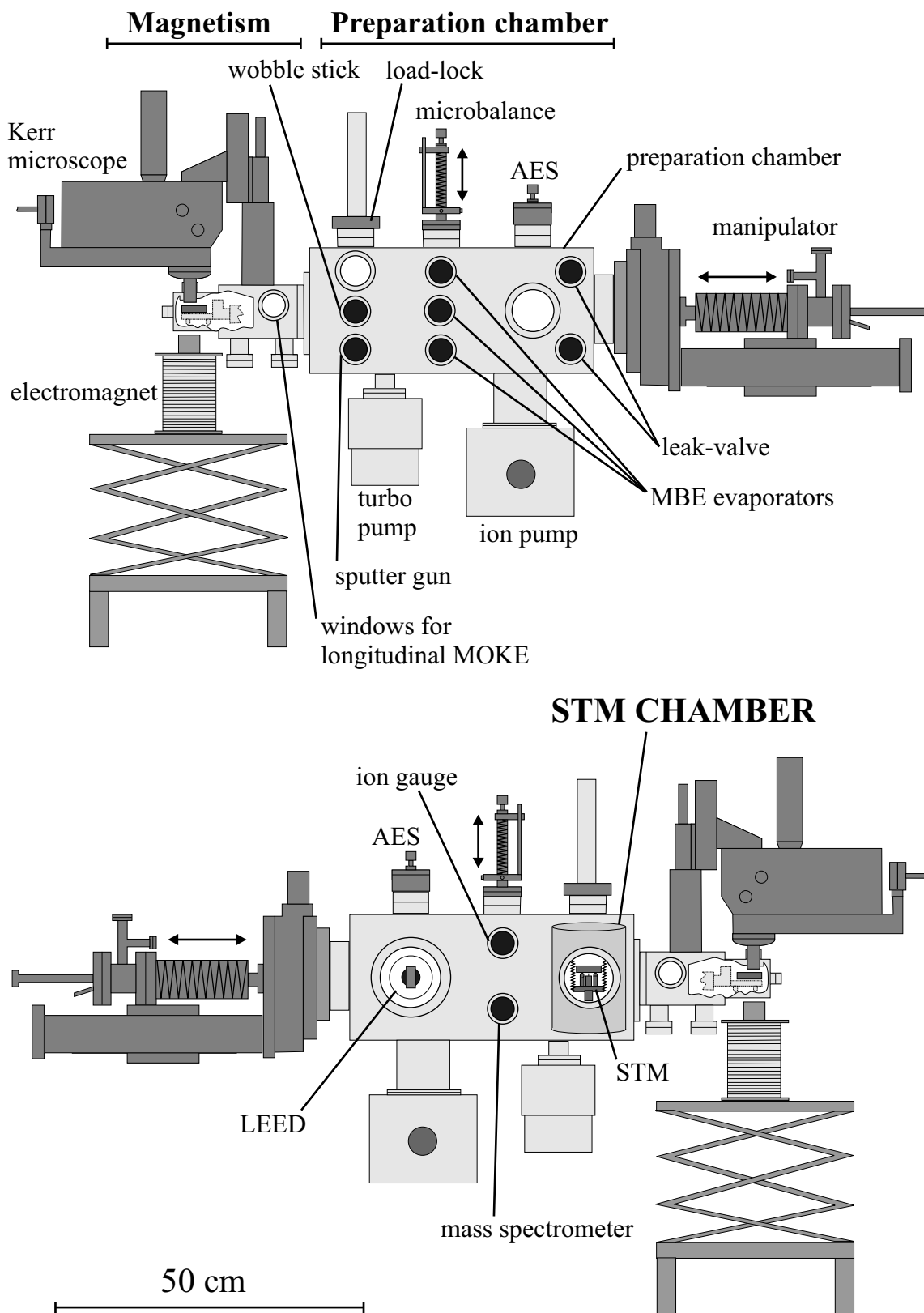


Figure 2.1: Schematics of the UHV system with views from left and right side.

2.1 The UHV system

Most of the experiments presented in this thesis have been performed in an existing UHV system built by Peterka and coworkers [96,97]. In parallel, I have set up a new UHV system which will be described in the following. A schematic of the chamber is shown in Fig. 2.1. The system consists of three main parts: a preparation chamber, a Scanning Tunnelling Microscope (STM) chamber and a magnetism chamber (MOKE chamber). The sample can be transferred in-situ between the different experiments by means of a long travel-range manipulator. The sample temperature can be varied from 900 K by electron bombardment heating down to 85 K by liquid nitrogen cooling and 35 K by liquid helium cooling during preparation as well as characterization. Standard tools for substrate preparation and film growth are available. Three Omicron evaporators are employed for the Molecular Beam Epitaxy (MBE). A quartz microbalance is used to calibrate the deposition rate. For chemical analysis and to check the cleanliness of

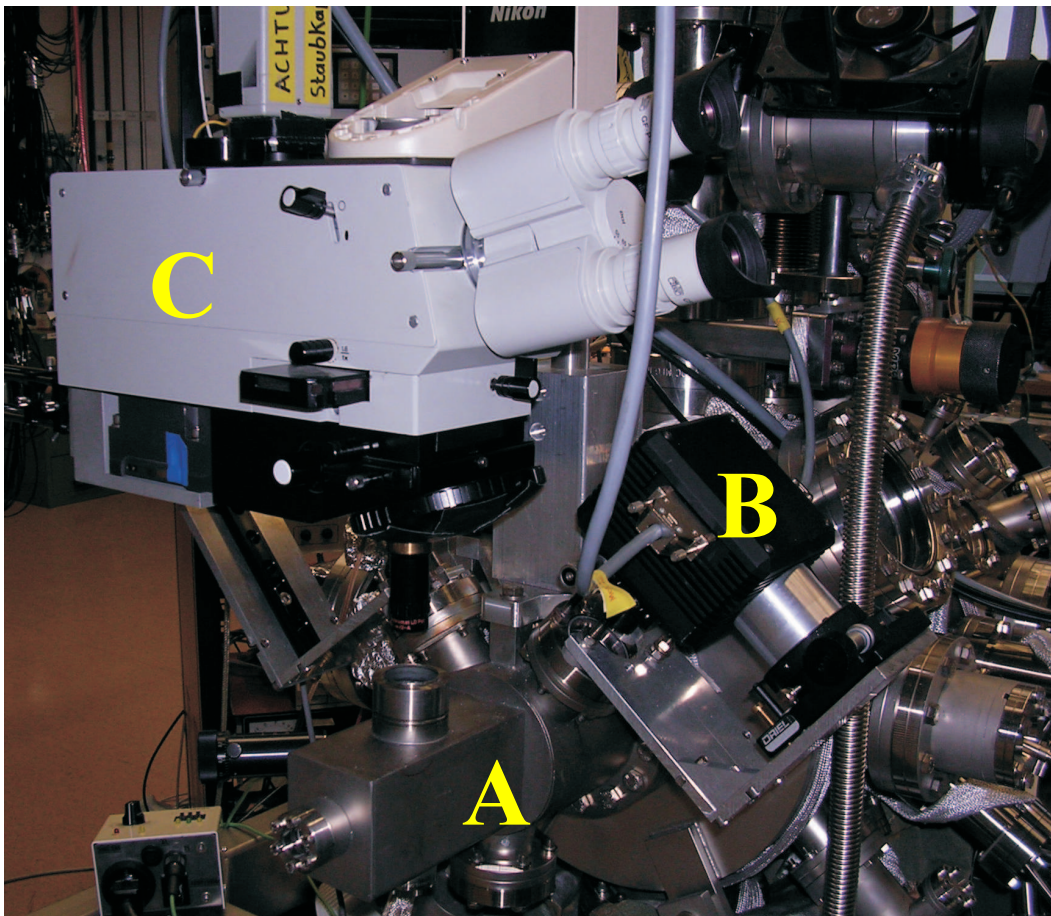


Figure 2.2: Picture of the MOKE chamber. (A) Magnetism chamber. (B) Setup for longitudinal MOKE. (C) Kerr microscope. The MOKE setup can also be adapted instead of the microscope to increase the sensitivity in polar geometry.

the sample before and after the sample growth, an Auger Electron Spectrometry (AES) is available. The surface structure can be studied by Low Energy Electron Diffraction (LEED).

The sample can be transferred into the magnetism chamber (Fig. 2.2(A)). Here, Magneto-Optical Kerr Effect (MOKE) measurements can be done to investigate the magnetic properties of the samples. Integral MOKE (Fig. 2.2(B)) and laterally resolved Kerr microscopy (Fig. 2.2(C)) are used to acquire hysteresis magnetization loops and for magnetic domain imaging (see Sec. 2.2). Two electromagnets produce external magnetic fields at the sample position up to 70 mT within the film plane and 40 mT perpendicular to the film plane. The magnetic field is measured by a Hall probe situated between the magnet and the chamber. A calibration has been done to convert the measured field with the magnetic field at the sample position.

For STM measurements, the sample can be placed in the adjacent STM chamber by using a specially adapted wobble stick for the investigation of the morphology. A more detailed description of the Variable Temperature-STM (VT-STM) is given in Subsec. 2.1.2.

The UHV in the chamber is obtained by a turbo molecular backed by a rotary pump, an ion getter ionization pump, a Ti-sublimation pump and an H_2 -getter pump. A base pressure of $7 \times 10^{-11}\text{ mbar}$ is achieved. A load-lock system allows the storage of four different sample holders which can be inserted into the preparation chamber. The load-lock is pumped separately by a small turbo pump. The advantage is that new crystals can be located in the preparation chamber without breaking the vacuum. Two leak-valves allow the the filling of the chamber with gases for adsorption experiments.

2.1.1 The sample holder

A new sample holder was designed for the new UHV-chamber. This sample holder was necessary to allow a broad sample temperature range on one hand, and to fit the sample into the STM on the other hand. The sample is clamped between a ramp plate and a base plate, both made of molybdenum. The ramp plate has three identical ramps which are used for the coarse approach during STM measurements (see Subsec. 2.1.2). These two parts (as referred to in the following as "sample-holder"), are kept together by three small titanium screws. A top and a bottom view are shown in Fig. 2.3(a) and Fig. 2.3(b), respectively. The electrical insulation between the ramp plate (and the sample as well) and the base is provided by a sapphire ring (green ring in Fig. 2.3(c)), which, on the other hand, makes the thermal contact. The sample is in electrical contact with the ramp plate through a molybdenum ring (grey ring in Fig. 2.3(c)). Due to this design,

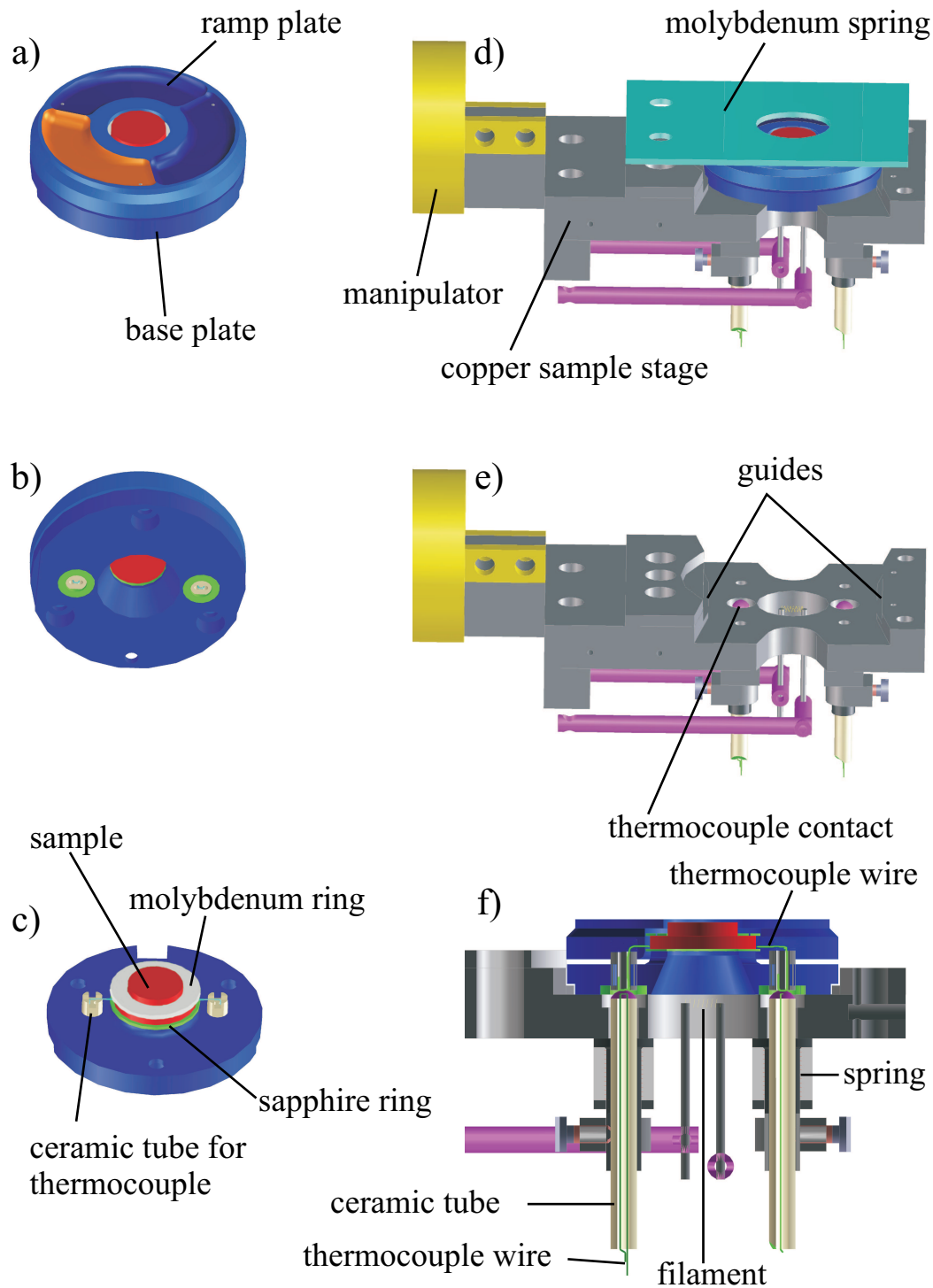


Figure 2.3: (a-c) The sample-holder: (a) Top view of the ramp plate. (b) Bottom view of the base of the sample-holder. (c) Thermocouple connections to the sample. (d-f) Manipulator sample stage: top (d,e) and section (f) views.

high voltages can be applied to the sample for electron bombardment heating through a Mo-spring in contact with the ramp plate, while the base plate sitting on the manipulator is grounded. A thermocouple is integrated in the base plate. The thermocouple wires are insulated from the base plate by ceramic (Al_2O_3) tubes (Fig. 2.3(b,c)). The sample temperature can thus be read out with good accuracy at the sample position.

The sample-holder is integrated into the manipulator sample stage (Fig. 2.3(d-f)) by using a wobble stick. Two small guides support the insertion of the sample-holder (Fig. 2.3(e)). After the insertion, the sample holder is held in position by a spring made of a thin molybdenum sheet (Fig. 2.3(d)). A round hole in the sheet allows access to the sample surface. The Cu sample stage has a central bore in which the filament for the sample heating is placed (Fig. 2.3(e,f)). The electrons are accelerated from the filament to the sample due to the high positive potential applied to the sample. Next to the central hole, electric feedthroughs for the thermocouple wires are located (Fig. 2.3(f)). Due to a spring mechanism, the two insulator ceramics cylinders can move when the sample-holder slightly in and make contact once the sample holder is at the right central position. The Cu-body is directly attached to the front end of cryo-stage of the manipulator. The compact design allows a minimum temperature of 32 K by liquid helium cooling. As mentioned, the sample-holder can be removed by the wobble-stick and placed in the STM chamber for structural characterization.

2.1.2 The VT-STM

The STM was invented by Binnig, Rohrer and coworkers in the 1980s [98, 99]. It allows the investigation of the geometric and electronic structures of flat surfaces with atomic resolution. Since its invention, the STM has been rapidly and considerably developed and it has been employed even to manipulate adatoms or absorbed molecules at surfaces [4, 5]. Visualizations of dynamics processes on surfaces in real space are also possible [100, 101].

The home-built microscope implemented in the new UHV chamber is shown in Fig. 2.4. The design is based on a VT-STM by Stipe *et al.* [102]. It allows Variable Temperature (VT) measurements in the range between 10 K and RT. The cooling is provided by a helium flow cryostat.¹ To reduce mechanical vibrations caused by the liquid He flow, the cold-plate of the cryostat is decoupled from the microscope by three CuBe springs. These springs also ensure the thermal contact with a Cu disk on which the piezo tubes are attached. The microscope is a beetle-type [103] with a tip exchange

¹KONTI-UHV-Kryostat 4-474 K, Cryovac, 53842 Troidorf, Germany

mechanism which allows the removal of the tip for preparation or substitution. Three bronze balls are glued to the approach piezo tubes and hold the molybdenum ramp plate of the sample holder, with the sample surface facing down. The oscillations of the CuBe springs are damped out by an eddy current damping system. This solution helps to damp out mechanical vibrations during the measurements. The coarse approach of the sample towards the tip is done by a "stick and slip" motion of the ramp plate on the three bronze balls. It is stopped once a tunnelling current is detected. The scanning of the surface is done by a fourth piezo (scan-piezo) with the tip pointing upwards. The scan-piezo tube is attached in a central position to the STM base plate. Gold-coated oxygen free Cu radiation shields around the microscope prevent from the heating of the sample by thermal radiation.

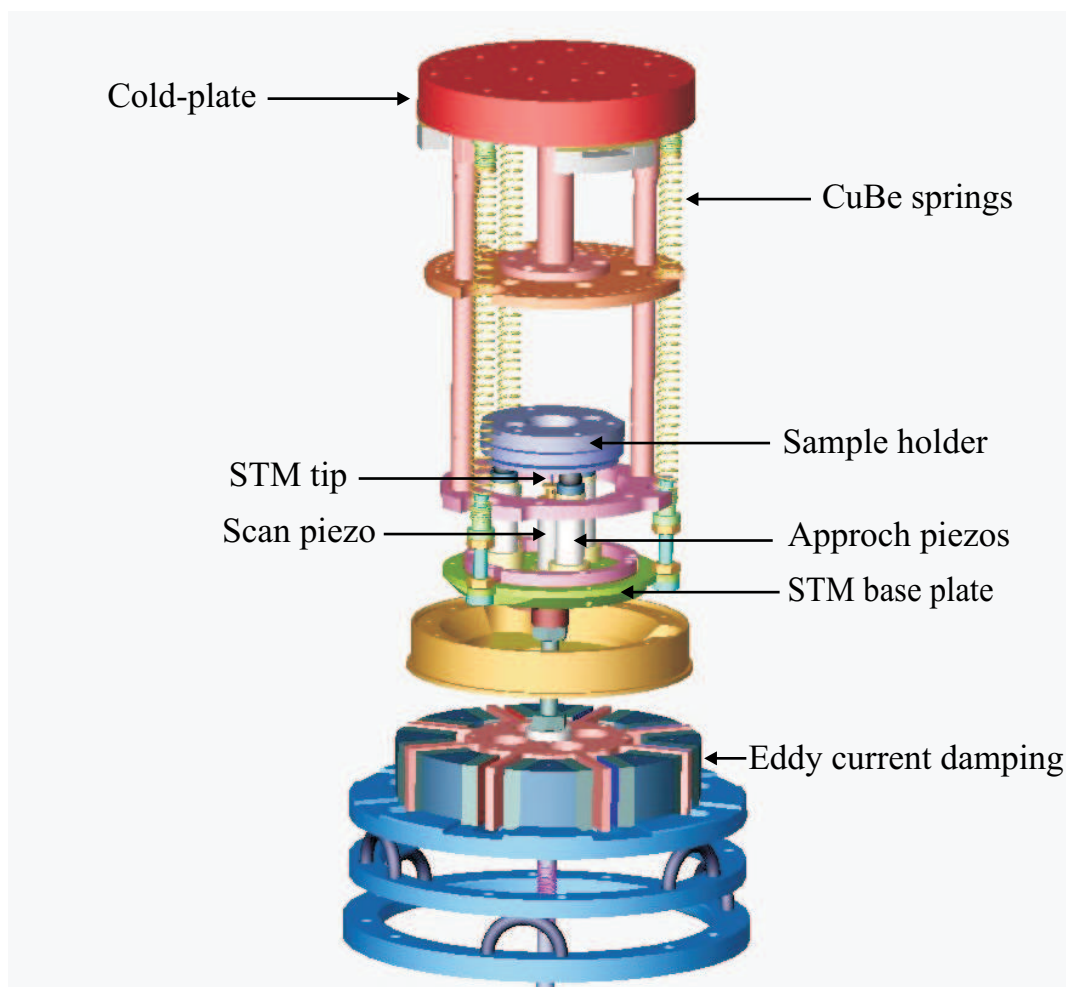


Figure 2.4: Variable Temperature-Scanning Tunneling Microscope (VT-STM).

2.2 Magneto-optical measurements

The interaction between electromagnetic radiation and magnetic matter is described by *magneto-optics*. The optical response of a ferromagnetic sample when its electrons are excited by the light depends on the relative orientation of the magnetization to the light polarization. A light beam incident on the sample surface is partially transmitted and partially reflected. In case of ferromagnetic samples, the polarization state of the incoming light is modified. In case of linearly polarized incident beam, the transmitted and the reflected beam will be elliptically polarized, with the main axis of the polarization ellipse rotated with respect to the linear polarization of the incoming beam. This effect can be detected in reflection, called Kerr effect [104], or in transmission, called Faraday effect [105]. For the reflected beam, this angle is called Kerr rotation, θ_K . The ratio between the major and minor axis of the ellipse is denominated Kerr ellipticity, ϵ_K . Measurements of θ_K and ϵ_K provide information on the magnetic state of any metallic or otherwise light-reflecting magnetic material with a sufficiently smooth surface.

The Kerr effect can be described theoretically by considering the quantum characteristic of the dielectric susceptibility tensor [106]. However, a phenomenological description using Maxwell's equations and Lorentz's force on the excited electrons of the sample in a magnetic field is often sufficient for experimentalists to describe the experimental results [107].

MOKE measurements and Kerr microscopy are far-field techniques, thus limited by the diffraction limit. Since visible light is used, a maximum resolution of a few hundreds of nanometers is usually achieved. While MOKE measurements give an integral information over a sample area of about 0.2 mm^2 , Kerr microscopy allows laterally resolved magnetic domain imaging with resolution $\approx 1 \mu\text{m}$.

2.2.1 Integral MOKE measurements

The setup for MOKE measurements is schematically shown in Fig. 2.5. A laser diode (visible light, $\lambda = 670 \text{ nm}$) is used as light source. The light is linearly polarized by passing through a Glan-Thompson prism (polarizer) and then focused on the sample surface. A spot of approximately 0.2 mm^2 is thus achieved. The result obtained from the MOKE measurements is therefore an average over the illuminated area of the sample. Different sample areas are investigated by moving the sample laterally along the in-plane directions. Either s- or p-polarized incoming light were adjusted for the measurements. The reflected beam goes through a second prism (analyzer), whose polarizing axis is crossed by 90° with respect to that one of the polarizer. Then, it is focused on the

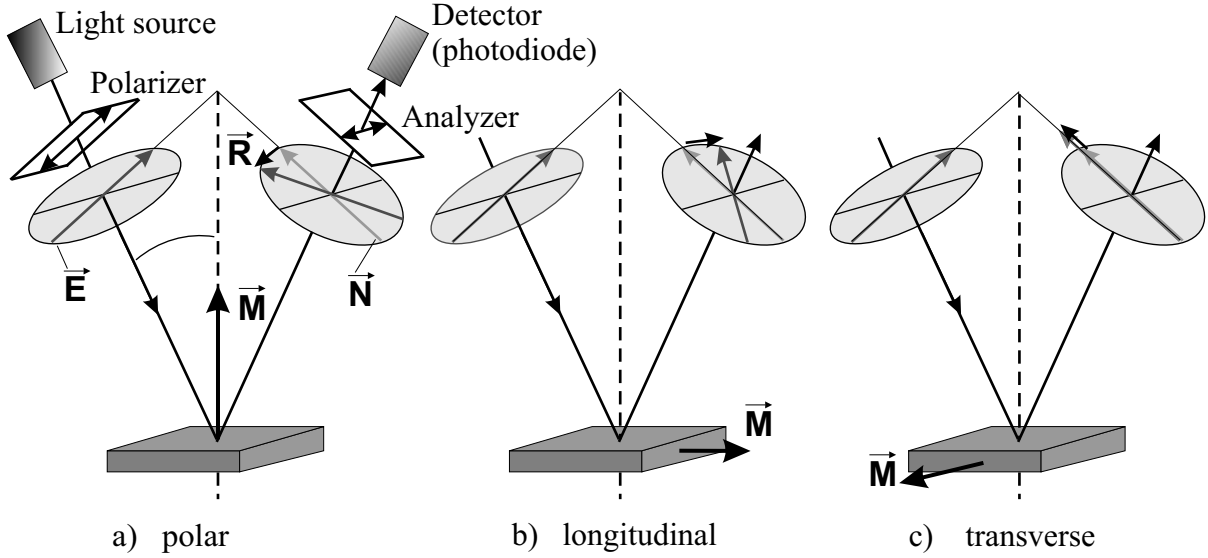


Figure 2.5: The three MOKE geometries: (a) polar, with out-of-plane magnetization. (b) longitudinal, with in-plane magnetization parallel to the incidence plane. (c) transverse, with in-plane magnetization perpendicular to the incidence plane. \vec{E} denotes the incident polarization vector, \vec{N} the unmodified component of the reflected light and \vec{R} denotes the perpendicular part of the Kerr amplitude after reflection.

photodiode detector, which provides a photocurrent according to the intensity of the incoming light. The signal is converted in a voltage, amplified and finally read out by a digital multimeter. The extinction ratio of the polarizers is of the order of 10^6 . The signal of the detector depends on the relative orientation of the polarizer and analyzer *and* the direction of the axis of the linearly polarized incoming beam with respect to the sample crystallographic directions. The polarizer and analyzer are iteratively rotated with respect to each other in order to find the minimum extinction signal. Going a little off from this "global" intensity minimum with the analyzer allows to measure the Kerr rotation. The Kerr ellipticity, on the other hand, is measured directly in a "local" minimum, which must not be the "global" minimum. A change of the detector signal is observed if a variation in the polarization (θ_K , ϵ_K) of the incident beam occurs during magnetization reversal.

The light source, polarizer, analyzer and the detector are mounted on an optical table attached directly to the chamber. Depending on the relative orientation between the incidence plane and the sample magnetization, three different Kerr geometries can be realized. In the *polar* geometry, the sample magnetization is perpendicular to the surface (Fig. 2.5(a)). In this case the Kerr effect is the larger the smaller the angle between the incident beam and the surface normal, θ . In the *longitudinal* MOKE, the magnetic field is applied parallel to the sample surface and parallel to the incidence plane

(Fig. 2.5(b)). In this case, the Kerr effect is roughly proportional to $\sin \theta$. Last, in the *transverse* MOKE the magnetization lies also in the sample plane but is perpendicular to the incidence plane (Fig. 2.5(c)). In this geometry, only changes in the signal amplitude can be detected as no light components propagate in the direction of the magnetization. The longitudinal and the transverse effect are both largest for grazing light incidence. In order to account for the angular dependence of MOKE, different angles θ are chosen in the experiments for different MOKE geometries. For polar MOKE, the incident and the reflected beam pass through the same window and $\theta \simeq 15^\circ$. For longitudinal MOKE, two different windows are used and $\theta = 45^\circ$. In the experiments presented in this thesis, when not explicitly specified, the ellipticity changes of the incident beam in polar and longitudinal geometries have been measured and referred to as polar and longitudinal Kerr signals, respectively.

MOKE hysteresis loops are taken by a computer which controls the power supply for the coils and reads out the Kerr signal and the magnetic field as a function of the applied current. To improve the signal to noise ratio, hysteresis loops have been averaged over several magnetization cycles. From the hysteresis loop shape, the easy magnetization axis of the sample can be identified. With the magnetic field applied along an easy axis, square loops are obtained (Fig. 2.6(a)), whereas zero remanence loops are measured when the field is applied along an hard direction (Fig. 2.6(b)). *S*-shaped loops with no remanence can also be the result of samples which decay in a multi-domain state at zero field. As a consequence, the net magnetization of the probed area is zero and no magnetic signal is detected. However, the field needed to saturate the sample is typically much smaller than the saturation field along a hard direction. If sufficiently high fields are not available, the saturation magnetization can not be achieved. The magnetization

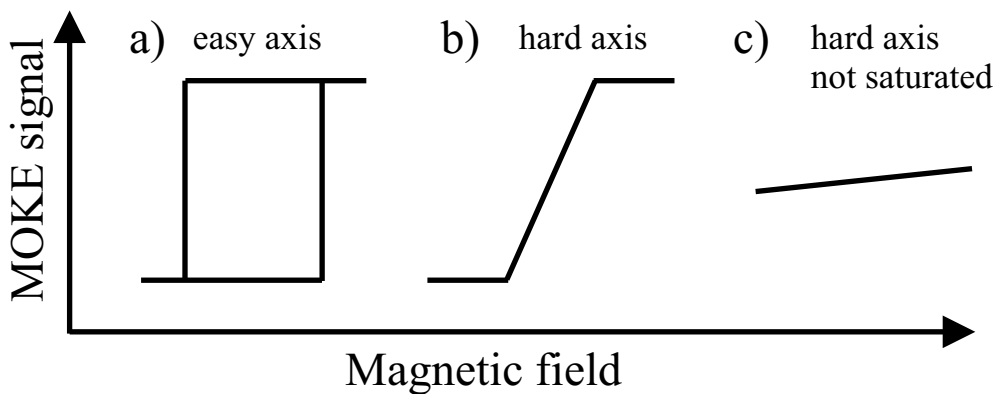


Figure 2.6: Characteristic MOKE hysteresis loops with the magnetic field applied along: (a) An easy magnetization axis. (b) An hard magnetization axis. (c) An hard magnetization axis, but not sufficient to saturate the sample.

loop appears as a straight, slightly oblique line (Fig. 2.6(c)).

The interpretation of the experimental results can sometimes be misleading in case of inhomogeneous magnetic field. Let assume to apply an in-plane field which has also an out-of-plane component to a sample with perpendicular easy axis. For large in-plane field, its out-of-plane component can eventually become large enough to switch the magnetization along the sample normal. An hysteresis loop is thus measured and could be misinterpreted as in-plane signal. The effect of this cross-talk is very pronounced for $\theta = 45^\circ$, since in this case the MOKE setup is for out-of-plane magnetization just as sensitive as for in-plane magnetization. To identify such a cross-talk, measurements along several sample directions are usually performed. The easy magnetization axis can be identified by the directional dependence of the coercivity and remanence.

A drawback of MOKE measurements is that no direct quantitative information, such as the magnetic moment per atom, can be obtained. The MOKE signal intensity depends on the angle of incidence, optical alignment and other parameters. Furthermore, it is not element-specific and contains integral magnetic information from the film *and* the substrate (if magnetic or with an induced moment). However, for a given sample and MOKE setup and assuming no variations of the magnetic moment per atom and crystal structure, changes of the saturation signal at different sample position are proportional to the relative film thickness.

2.2.2 In-situ Kerr microscopy

The Kerr microscope allows direct imaging of the magnetization state of the sample within an area of $400 \mu\text{m} \times 300 \mu\text{m}$. It is based on a commercially available Jenapol polarization microscope. To achieve high optical resolution, a setup suggested by Hubert [108] is adopted. Sufficient sensitivity for domain imaging in thin films of few monolayers is obtained by replacing the sheet polarizers by Glan-Thompson prisms in order to improve the light extinction ratio. The sample is placed directly in front of an U-shaped strain-free window with flat bottom. Antireflective coating on the window reduces the loss of sensitivity due to depolarizing effects by the window itself. The shape of the UHV window allows to realize a distance between sample surface and microscope objective as small as 8 mm. A lateral resolution of $\approx 1 \mu\text{m}$ and optical magnification of 10 is achieved. Images are read out by a computer controlled CCD camera with an acquisition rate of 0.3 s/image . The advantage of the setup is that changes in the magnetization state can be observed directly as a function of the experimental parameters, such as magnetic field, sample temperature or gas adsorption. The microscope is attached to a solid tripod directly to the UHV chamber. This type of setup allows

convenient position adjustment as well as the removal of the microscope for the bake out of the chamber.

Proper illumination plays an important role in order to achieve high quality images. A 1 W Ar ion laser ($\lambda = 514 \text{ nm}$) has been used as light source. It ensures high intensity and stable output power [109]. The laser light is coupled into a 30 m long quartz-quartz multimode fiber (MMF) with a diameter of $200 \mu\text{m}$ and a numerical aperture (NA) of 0.20. The output of this fibre provides an easy to handle monochromatic, stabilized, high intensity light source of small size, ideally suited for Kerr microscopy.

Further technical details about the adjustment of the optical path and the method used to avoid strong speckle patterns due to coherence of the laser light are described elsewhere [97].

Fig. 2.7 shows a Kerr image of a multi-domain state of 3 ML Fe on Cu(100). Black and white areas correspond to magnetic domains with perpendicular magnetization pointing in opposite out-of-plane directions. It is also possible to obtain hysteresis loops with the Kerr microscope. It needs to acquire images during a full cycle of the magnetic field. Afterwards, the average color of each image has to be calculated and plotted as a function of the applied field. This procedure is slower than that one used by MOKE measurements, but yields a direct correlation between sample magnetization state and hysteresis loop.

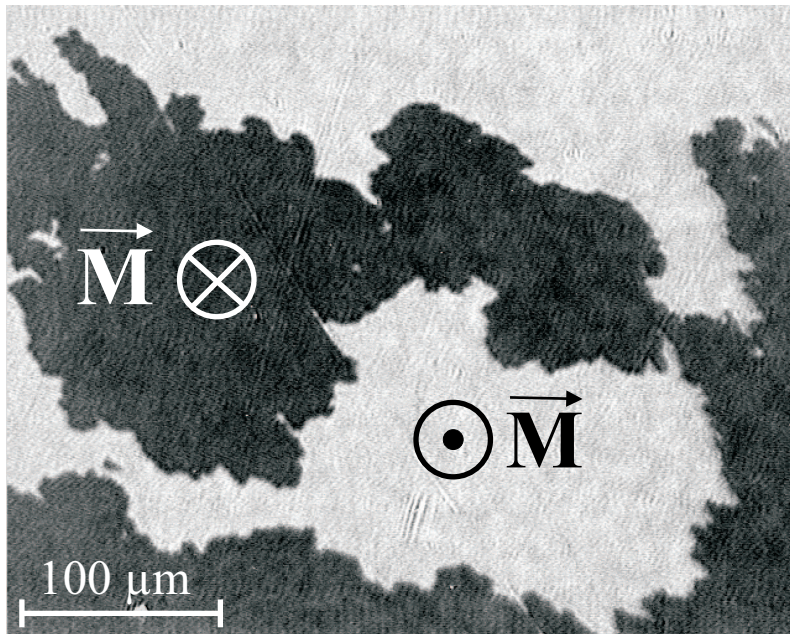


Figure 2.7: Kerr microscope image taken on 3 ML Fe/Cu(100). Dark and white area correspond to magnetic domains with opposite magnetization perpendicular to the film plane. Image size: $400 \mu\text{m} \times 300 \mu\text{m}$.

2.3 Sample preparation

The samples investigated in this thesis have been grown in-situ by Molecular Beam Epitaxy (MBE). The film materials are evaporated by electron bombardment heating from a rod or a crucible and deposited on a crystal which has been properly prepared. The structure and morphology of the adlayer depend on many parameters, such as the evaporated element, the substrate material and orientation, the substrate temperature, the deposition rate, the pressure and the residual gases inside the preparation chamber. In particular, the choice of the substrate is fundamental. The atoms, once they reach the surface, are mobile (if the temperature is not too low) and tend to arrange themselves in order to minimize the free surface energy of the substrate-adlayer system [110]. In general and on flat surfaces, three different growth modes can be distinguished: A layer-by-layer growth (Frank van der Merwe), in which the second atomic layer only starts to nucleate after the first one is complete. This occurs when the free surface energy of the substrate is larger than that one of film. A 3D-growth (Volmer-Weber), in which the second layer starts to grow before the first one is complete. In this case, several open layers can be present during the growth. A combination of the first two gives rise to the third growth mode (Stranski-Krastanov). Here a layer-by-layer growth of the first atomic layers (wetting layer) is followed by the formation of 3D-islands. When the lattice mismatch between the substrate and adlayer structures is small, pseudomorphic growth is often observed. The films assume thus the crystallographic structure of the substrate. This is, for instance, the case for Fe/Cu(100) grown at room temperature ($RT \sim 298 K$) [75, 111]. The growth mode can also be modified by controlling the surface orientation. By choosing a different crystal orientation, a completely different growth mode can sometimes be obtained. As an example, 3D-islands are observed in case of Fe/Cu(111) [112]. While Fe grows on Pt(111) in a Volmer-Weber mode [113], in case of vicinal Pt(997) substrate (stepped surface with (111) terraces), a step flow growth has been observed for the first atomic layer for deposition temperatures between 200 K and 400 K [114].

Cu substrates

In the experiments presented in the chapters 3 and 4, Cu(100) crystals have been used as substrates. The crystals were mechanically polished ex-situ and are commercially available. After insertion in the UHV system, the Cu(100) substrates have been prepared in-situ by repeated sputtering/annealing cycles [12, 115]. The kinetic energy of the Ar^+ ions for sputtering is set to 500 eV. The ions hit the sample under an angle of incidence

of 45° . Sputter damages on the surface are removed by heating the sample up to 840 K between the sputter cycles. At least three cycles of sputtering/annealing have been done before the film deposition. During the last annealing the sample is heated only to 650 K . From this temperature the sample is slowly cooled down to RT with a rate of $\sim 0.5\text{ K/s}$. The cleanliness of Cu substrates during and after the preparation has been checked by AES.

Pt substrates

In the experiments presented in the chapters 5 and 6, Pt(111) and Pt(997) crystals have been used as substrates. The Pt substrates have been prepared in-situ by repeated sputtering/annealing cycles. The kinetic energy of the Ar^+ -ions for sputtering is set to 1 keV . Sputter damages on the surface are removed by heating the sample up to 870 K between the sputtering cycles. From this temperature, the sample is slowly cooled down to RT with a rate of $\sim 0.5\text{ K/s}$. The vicinal Pt(997) surface is formed by a regular array of terraces of 20.1 \AA width (8 atomic rows) with (111) orientation, separated by monatomic steps (height of 2.26 \AA). The cleanliness of Pt substrates during and after the preparation has been checked by AES. The presence of regular periodic steps along the whole surface has been checked by LEED. The preparation was finished after the characteristic superstructure of the (997) surface with diffraction sharp spots was observed.

Film growth

Iron is evaporated from a rod with a purity of 99.99% by electron bombardment. During the film growth, the pressure in the chamber is less than $2 \times 10^{-10}\text{ mbar}$. The Fe ion flux is kept constant during deposition by adjusting the electron acceleration voltage. The evaporation rate of the source is typically 1 \AA/min as calibrated by depositing on a quartz microbalance just before the film preparation. The calibration with the microbalance is based on the density of bulk Fe. A bcc-Fe layer corresponds to a thickness of 1.43 \AA ($\rho_{Fe}^{bcc-100} = 1.214 \times 10^{15}\text{ atoms/cm}^2$). For the measurements of Fe on Cu substrates (chapters 3 and 4), the Fe thickness are given in monolayers (ML) without any conversion. Here, 1 ML Fe corresponds to a reading of 1.43 \AA on the microbalance display.

Copper is evaporated from a molybdenum crucible heated by electron bombardment. In this case the emission current is kept constant by adjusting the electron acceleration voltage. The deposition rate is typically $0.5 - 1\text{ \AA/min}$. For the conversion in ML

of the Cu thickness, it has been considered 1 ML Cu = 1.805 Å ($\rho_{Cu}^{fcc-100} = 1.535 \times 10^{15} \text{ atoms/cm}^2$).

For Fe on Pt substrates (chapter 5, the Fe coverage has been converted to monolayers (ML) by considering the actual areal density of the adlayers and assuming pseudomorphic fcc-structure for all the layers ($\rho_{Pt}^{fcc-111} = 1.503 \times 10^{15} \text{ atoms/cm}^2$). One pseudomorphic fcc-Fe layer on Pt(111) corresponds to 1.78 Å.

For the study of the magnetic properties of the samples as a function of film thickness, it is usually convenient to grow wedge-shaped films. Films of varying thickness are prepared either by moving a metal shutter placed between sample and evaporator or by moving the sample. The height and length of the wedges are determined by the evaporation rate and the speed by which the sample or shutter are moved. The standard wedge length used in the experiments presented in this thesis was 4 mm.

Chapter 3

Temperature dependence of the magnetism of Fe/Cu(100)

The magnetic properties of epitaxial Fe films grown at low temperature ($\sim 100\text{ K}$) on Cu(100) is of particular interest for experimentalists due to the coexistence of interesting structural and magnetic phases. The easy magnetization axis is found perpendicular to the surface below the critical film thickness of $t_{crit} = 4.3\text{ ML}$, at which a spin reorientation transition (SRT) is observed [116]. Thicker films show in-plane magnetization. The perpendicular magnetization is ascribed to the dominating surface anisotropy contribution arising at the film-vacuum interface, K_{f-vac} [77].

Within this work, changes of the magnetic properties due to thermally-induced modification of the film morphology have been studied on the same film, allowing for a direct correlation between structure and magnetic properties. Moreover, after the morphological changes have been accomplished during annealing, the purely reversible temperature dependence of the magnetism can be studied in subsequent repeated annealing cycles by in-situ MOKE measurements and Kerr microscopy. The main results of these studies are: (i) The separation and identification of reversible and irreversible contributions to the magnetic anisotropy as a function of temperature (Sec. 3.1). (ii) The determination of the distribution of the energy barriers that controls the coercivity, the Barkhausen volume and the domain wall propagation (Sec. 3.2).

This project was started by D. Peterka and it has been continued during my PhD. For completeness of discussion, the Fig. 3.1 and 3.2, already published in his PhD thesis [97], have been included also in this chapter.

3.1 Thermally-induced spin reorientation transition

Temperature driven reversible and irreversible changes of the magnetic properties of Fe on Cu can separately be identified by monitoring the magnetism during annealing/cooling cycles. In particular, the temperature dependence of the surface anisotropy is determined from measurements of the critical film thickness between 127 K and 300 K by means of Kerr microscopy and MOKE measurements [117]. The change of the magnetization state of Fe/Cu(100) with temperature is shown in Fig. 3.1. The Kerr images are taken on a Fe wedge in a thickness range around t_{crit} and show the SRT from perpendicular (dark area) to in-plane magnetization (bright area). Before capturing the image in Fig. 3.1(a) at 127 K (after annealing at 270 K), the sample has been magnetized by an external field pulse to obtain a single domain magnetization state. The SRT shifts towards smaller Fe thickness (β) when the temperature is gradually increased to 280 K with a rate of approximately 5 – 10 K/min (Fig. 3.1(b)). No further shift is observed

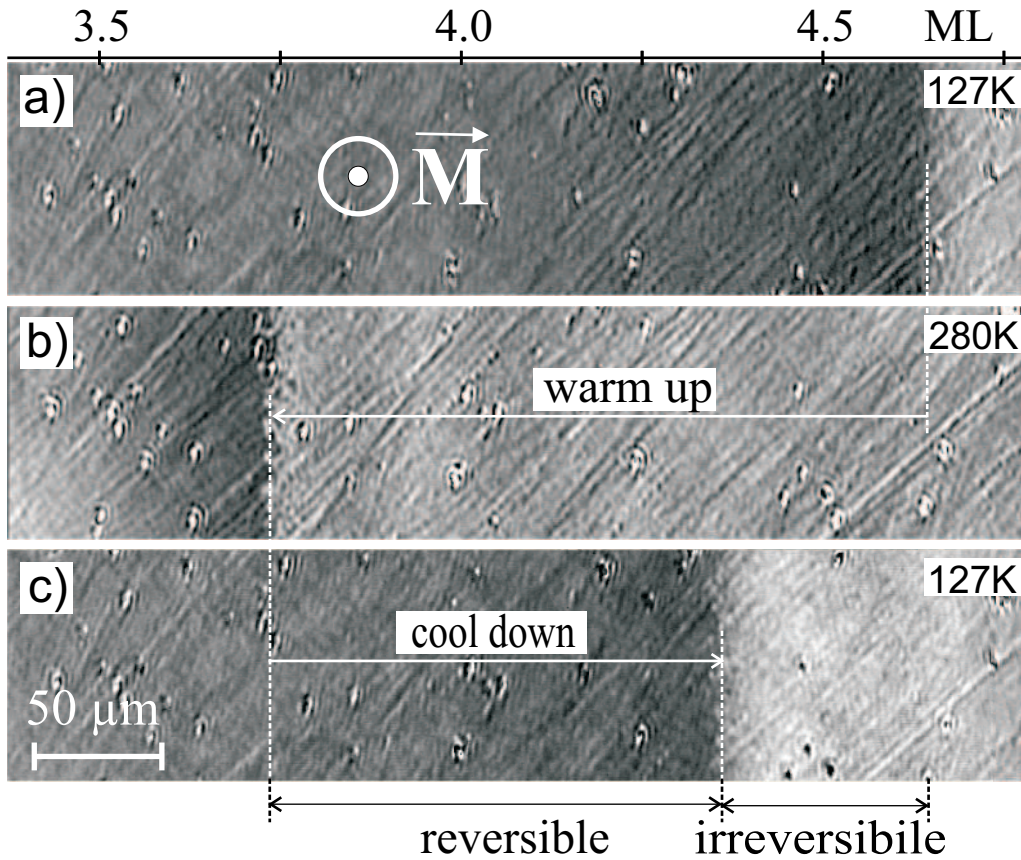


Figure 3.1: Thermally-induced shift of the reorientation transition of an Fe wedge. (a-b) t_{crit} changes from α to β when raising the temperature from 127 K to 280 K. (c) Cooling back to 127 K shifts the reorientation transition to $\gamma \neq \alpha$. Size of each image: $400 \mu\text{m} \times 90 \mu\text{m}$. Drawn from D. Peterka's PhD thesis [97].

when the sample temperature is held constant at the annealing temperature, T_a . Reversing the experiment, i.e. cooling the sample back to 127 K, causes a shift of the SRT back to higher film thickness (γ) (Fig. 3.1(c)), but the $t_{crit} = \alpha$ as in Fig. 3.1(a) cannot be achieved again. Repeating the experiment, i.e. annealing to 280 K followed by cooling to 127 K, now shifts the SRT fully reversible between β and γ . In other words, at a given Fe thickness, the easy axis of magnetization can be switched reversibly between in-plane and out-of-plane by changing the temperature. Clearly, the magnetic anisotropy of the Fe films depends partly reversible (for $\beta < t_F < \gamma$), and partly irreversible ($\gamma < t_F < \alpha$) on the temperature.

The advantage of the experiment is that during subsequent annealing the reversible change of the magnetic anisotropy can solely be observed since irreversible changes have already been accomplished during the preceding annealing/cooling cycle, allowing for a separation of reversible and irreversible contributions.

The full temperature dependence of t_{crit} in the temperature range between 127 K and 300 K is shown in Fig. 3.2(a). The t_{crit} measured at T_a is plotted as solid symbols (\bullet). Plotted at the same temperature as an open symbol (\circ) is the shifted t_{crit} measured at 127 K after the sample has been cooled down from the respective T_a . All data in this figure have therefore been measured under the same experimental conditions, i.e. the same temperature. The *difference* between adjacent data points in this data set corresponds to irreversible shifts of t_{crit} upon annealing, equivalent to the change from α to γ in Fig. 3.1. The data set represents irreversible changes in the spin reorientation transition with increasing temperature. On the other hand, the difference between the two data sets in Fig. 3.1(a) corresponds exclusively to reversible changes in t_{crit} , analogous to the shift from β to γ .

The observed temperature dependence of the magnetism is ascribed to a temperature dependence of the surface anisotropy constant, $K_S = K_{f-vac} + K_{f-s}$, which is the origin of the perpendicular magnetization for Fe films thinner than 4.3 monolayer (ML). The K_S summarizes contributions to the total magnetic anisotropy of the films arising at the film-vacuum, K_{f-vac} , and film-substrate, K_{f-s} , interface. As already seen in Sec. 1.1, the magnitude and sign of K_S determines the critical thickness at which the magnetization reorients from out-of-plane to in-plane:

$$t_{crit} = \frac{2(K_{f-vac} + K_{f-s})}{2B_1(\varepsilon_{\perp} - \varepsilon_{\parallel}) + \mu_0 M_S^2} \quad (3.1)$$

Here, B_1 is the bulk magneto-elastic coupling constant, ε_{\parallel} and ε_{\perp} being the in-plane and out-of-plane strain, and M_S the saturation magnetization. The observed $t_{crit} = 4.3$ ML

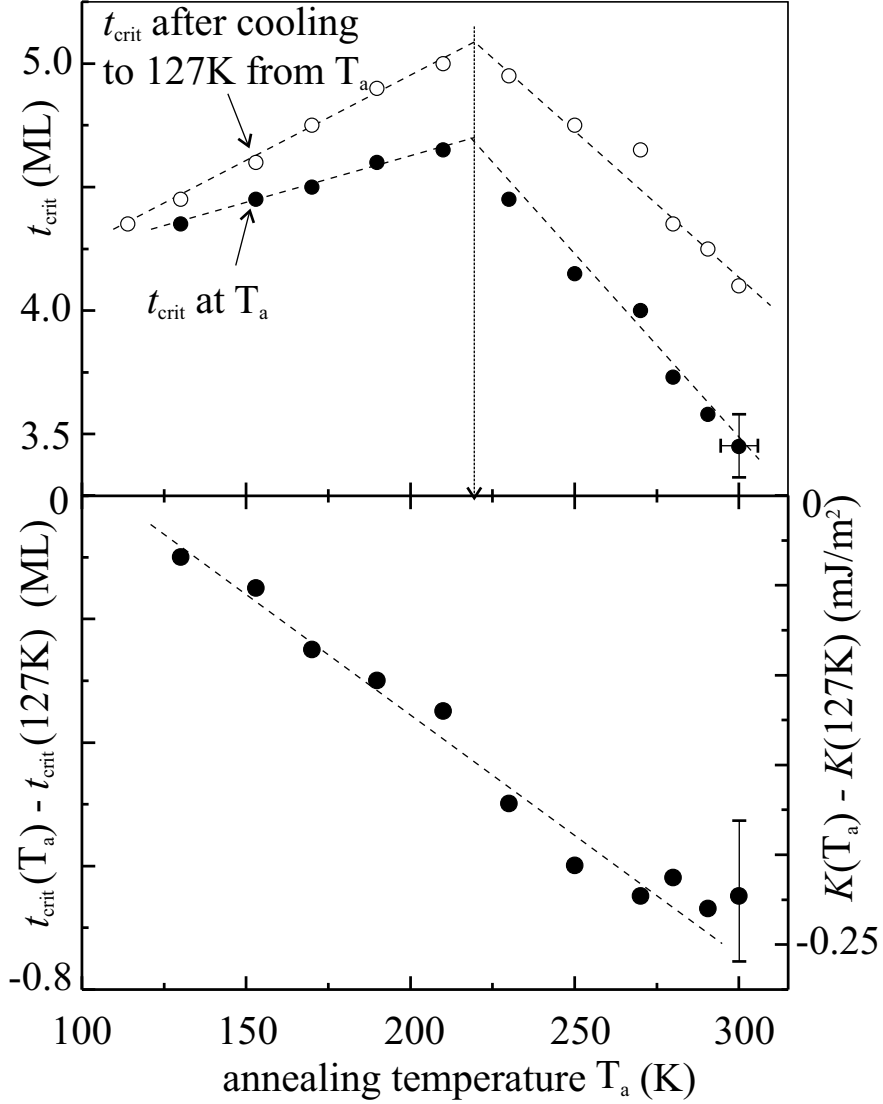


Figure 3.2: (a) Temperature dependence of the critical thickness in the temperature range between 127 K and RT. (b) The difference of both data sets in (a) is proportional to $K(T)$. *Drawn from D. Peterka's PhD thesis [97].*

of the as-grown film is reproduced by inserting $K_{f-vac} = 0.89 \text{ mJ/m}^2$ [118], $K_{f-s} = 0.6 \text{ mJ/m}^2$ [2], $M_S = 1751 \text{ kA/m}$, $\varepsilon_{\parallel} = 5\%$ and $\varepsilon_{\perp} = 1.54\%$. The strain is calculated by using the lattice constant for Cu, $a_{Cu} = 3.61 \text{ \AA}$ [119], fcc-Fe, $a_{Fe}^{fcc} = 3.59 \text{ \AA}$ [120], and the average Fe interlayer spacing, $d = 1.87 \text{ \AA}$ [20]. An effective $B_1^{eff}(\varepsilon_{\parallel}) = 13.5 \text{ MJ/m}^3$ has been used to account for the strain dependence of the magneto-elastic coupling [121]. Assuming the effective epitaxial strain and the B_1 to be independent of the film temperature, as it is for bulk below 300 K [122], changes in t_{crit} can solely be attributed to a temperature dependence of K_S . This approximation is based on the fact that the surface anisotropy is the dominant energy contribution, and changes in B_1^{eff} during the growth of already existing islands are small. As will be

discussed later, the irreversible shift of t_{crit} from α to γ will be correlated with thermally activated structural changes in the film. Based on our experimental observation, the K_S may be separated into a temperature dependent reversible and an irreversible contribution:

$$K_S = K(T) + K_{irr} \quad (3.2)$$

The $K(T)$ corresponds to the surface anisotropy if there were no structural changes in the film. Both contributions, $K(T)$ and K_{irr} , could be separately determined for the first time. $K(T)$ is calculated from the shift of t_{crit} during cooling, $t_{crit}(T_a) - t_{crit}(127\text{ K})$, by using Eq. (3.1), and plotted in Fig. 3.2(b). Only changes in $K(T)$ with respect to its value at 127 K can be determined. After the structural changes are fully accomplished (we will see in the following that this happens at $\sim 240\text{ K}$), K_{irr} is zero in the subsequent cycle. Thus the reversible shift with T can exclusively be recorded. It can be seen that within the temperature range below 300 K a linear decrease of the $K(T)$ with increasing temperature is observed.

Qualitatively, the result agrees with theoretical models that predict a reduced anisotropy as the thermally-induced jiggling of the spins reduces the expectation value of the magnetization [123,124]. A quantitative comparison of our data with such models requires an analysis in terms of T/T_C . For the films investigated the Curie temperature, T_C , is well above 300 K, and could therefore not be measured due to the onset of intermixing at the Fe-Cu interface. However, similar results of decreasing surface anisotropy with temperature have been found by other authors for Ni/Re(0001) [37] and Ni/W(110) [125]. The trend of the few data available suggests that the destruction of the perpendicular ferromagnetic ordering of the spins by the thermal agitation at the Curie temperature is always preceded by a spin reorientation into the plane.

In contrast to the linear dependence of $K(T)$ as deduced from the reversible shift of t_{crit} , the irreversible shifts depend non-linearly on temperature. The t_{crit} measured at 120 K increases after annealing to $T_a \leq 220\text{ K}$, but decreases for higher annealing temperatures (Fig. 3.2). The data clearly reflect a competition of anisotropy contributions of different sign. It is therefore reasonable to attribute these irreversible changes to the anisotropy contribution, K_{irr} , arising from thermally activated structural changes in the film. To identify such structural changes we performed, in collaboration with N. Lin and A. Dmitriev (Kern's group, Max Planck Institute, Stuttgart), VT-STM experiments on 3 ML Fe grown at 120 K on Cu(100). Representative STM images taken in the temperature range between 165 K and room temperature are shown in Fig. 3.3(a-

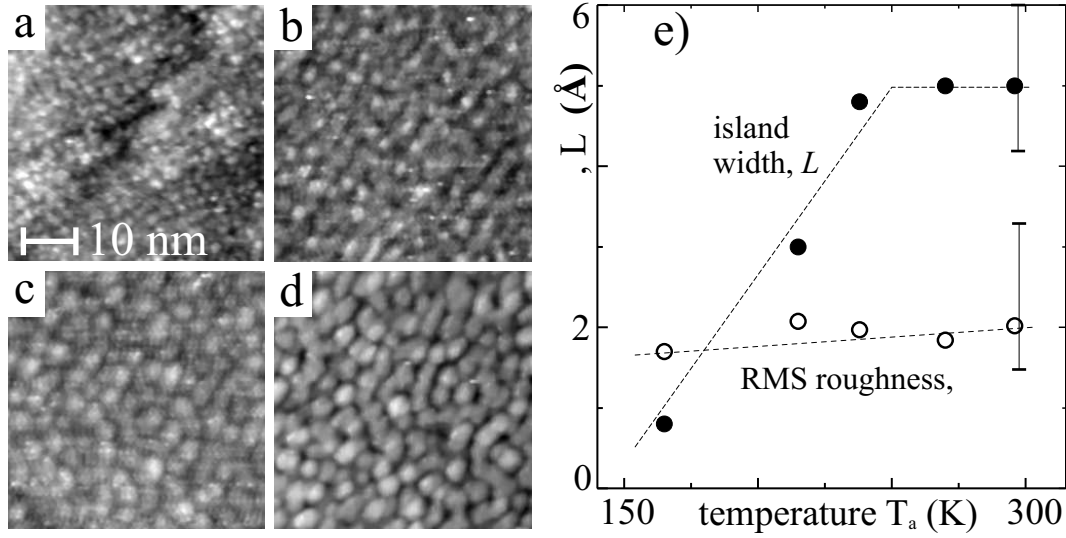


Figure 3.3: (a-d): STM images of a 3 ML Fe film grown on Cu(100) at 120 K, at 165 K (a), 215 K (b), 238 K (c), and 296 K (d). (e) Island width and RMS roughness as a function of annealing temperature. *In collaboration with N. Lin and A. Dmitriev, Nanoscale Department, MPI Stuttgart*

d). The image in Fig. 3.3(a) reveals that as-grown films exhibit a rather high density of very small islands of width $L \leq 1 \text{ nm}$. The morphology of the film changes visibly with increasing temperature Fig. 3.3(b-d). The island width, L , and the RMS roughness, σ , have been extracted from the STM images, and are plotted as a function of T_a in Fig. 3.3(e). Three important information can be concluded from the data: (i) Below $T_a = 240 \text{ K}$ the island width increases with temperature from $\leq 1 \text{ nm}$ up to $\approx 5 \text{ nm}$. (ii) No further change in the island size is observed above 240 K. (iii) The RMS roughness does not significantly change during annealing. In other words, visible improvements of the film quality mainly affect the island diameter and are accomplished below 240 K.

Based on these results the increase of t_{crit} below 220 K is correlated with the increase of the island width, L , in the same temperature range. In this interpretation the enlargement of L causes an increase of K_{irr} . This conclusion therefore strongly supports calculations given by Bruno *et al.* which show that any surface roughness, σ , and islands of width, L , diminish the surface anisotropy with respect to the value of the ideally flat film by $\Delta K_S/K_S = -2\sigma/L$ [126]. For the Fe films shown here it is the increase of L that increases the effective surface anisotropy while the RMS roughness remains almost unchanged.

After the island growth is accomplished at about 240 K no further increase of t_{crit} is expected according to this model. Instead, the data in Fig. 3.2(a) show that for $T_a > 240 \text{ K}$ a decrease of t_{crit} is observed. Presumably, this decrease of K_{irr} is caused

by structural changes in the film of different nature, not visible in our STM images. One might speculate if the formation of bcc-crystallites in the fcc-Fe film, as have been discovered recently with high resolution STM on RT grown Fe films [76], reduce the perpendicular anisotropy by gradually making the film more bcc like. This idea is supported by experiments showing drastic changes of the morphology of such films on Cu(100) after cooling and subsequent warming up to 300 K, also ascribed to a transition of the film towards bcc-structure [29]. Thermally activated interdiffusion between Fe and Cu, which is known to alter the magnetic anisotropy energy [22], does not have to be considered here since it is found to be negligible below 300 K [127].

In conclusion, the observed temperature dependence of $t_{crit}(T_a)$ is the result of a non-linear irreversible anisotropy changes due to competing thermally activated changes in film structure and morphology, superimposed by the linear reversible $K(T)$ -dependence. It will be shown in the following that also the coercive field, H_C , of the Fe films is governed by the island structure.

The temperature dependence of H_C measured on a 3 ML Fe film grown on Cu(100) at 120 K is shown in Fig. 3.4. The data measured on the as-grown film during the

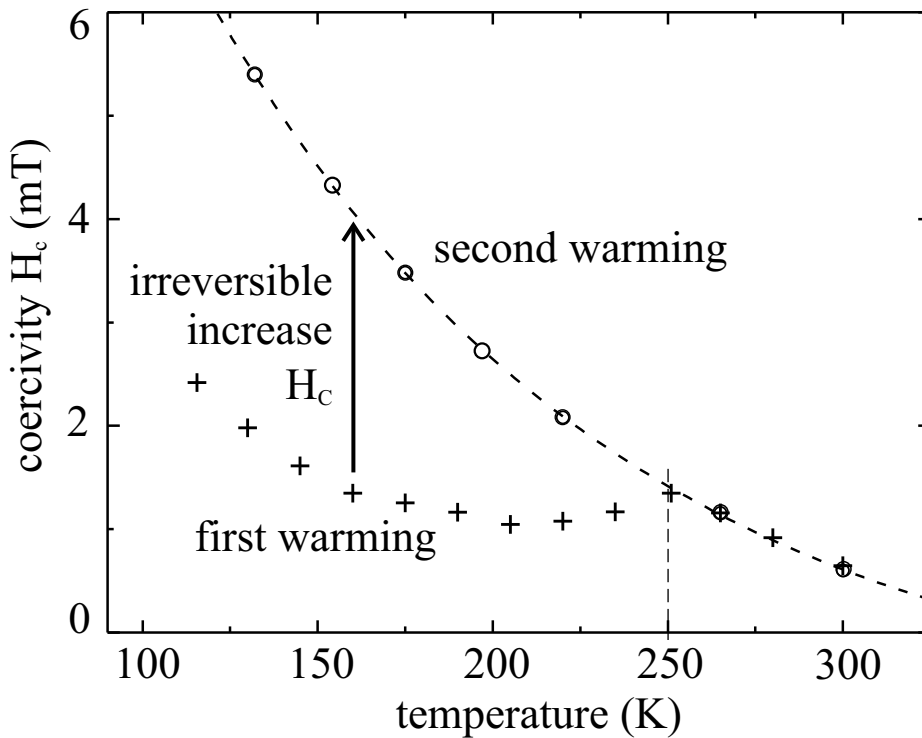


Figure 3.4: Temperature dependence of the coercivity of 3 ML Fe grown at 127 K during the first (+) and subsequent (o) annealing.

first annealing after the growth (+) are markedly different from the temperature dependence of H_C found for subsequent annealing (o). The coercivity increases irreversibly after annealing to $T_a < 250 K$, while the two data sets match above $250 K$. The irreversible increase of H_C is attributed to the observed change in the film morphology. As mentioned in Sec. 1.2, the energy and thus the field needed to reverse the magnetization in the sample are determined by the variation of the free energy of the domains, $H_C \sim \partial E / \partial r$. The islands introduce energy barriers for domain wall propagation due to exchange and anisotropy inhomogeneities [47], thus determining the coercivity. The film morphology in Fig. 3.3 can be used to estimate the wall exchange energy variation, $\Delta\gamma$, at the island sites. By using $\gamma = 4\sqrt{At_F K_S}$, the variation of the film thickness, $\Delta t_F = 4.8 \text{ \AA}$, results in $\Delta\gamma = 1 \times 10^{-11} \text{ J/m}$. Among this exchange effect, also the magnetic anisotropy energy and the strain vary with the island size, further contributing to the energy barriers at the island sites. This means that it is less favorable for the domain wall to enter the 3D islands due to the enhanced wall energy there.

The Bloch domain wall width can be estimated using the expression, $\delta = \sqrt{At_F / K_S}$. By inserting the film thickness, $t_F = 5.4 \text{ \AA}$, $A = 2 \times 10^{-11} \text{ J/m}$ and $K_S = 1.49 \text{ mJ/m}^2$ the wall width of $\delta = 6 \text{ nm}$ is obtained. The use of bulk exchange stiffness, A , is a good approximation for films thicker than 1 ML; calculations for bcc-Fe(110) layer indicate that A is somewhat increased only at the surface of thin films [128], in contrast to pure 2D systems [129]. It now becomes clear that it is mainly the increase of the island width during annealing which enhances the trapping of domain walls and causes an increase of H_C . The mechanism is illustrated in Fig. 3.5. In the as-grown film, at low temperatures, the islands are considerably smaller than δ . The wall therefore stretches over several islands and domain wall propagation is comparatively easy. As their width increases with temperature, eventually at $240 K$ the islands become comparable in size to the Bloch wall width, $L \approx \delta$. Now, the wall is being trapped most efficiently between

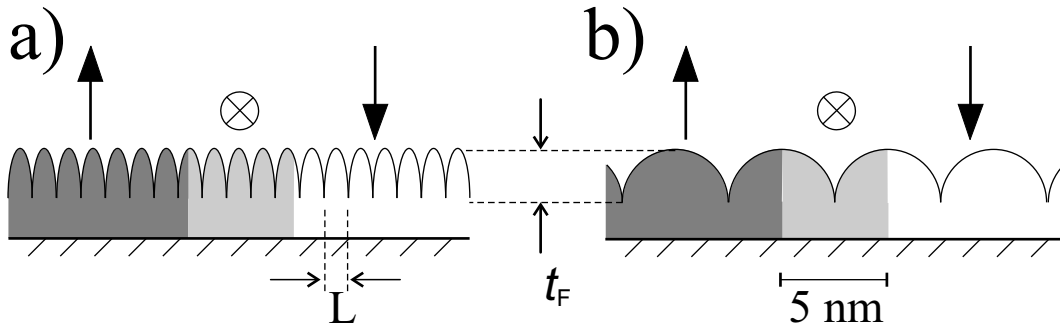


Figure 3.5: Model of the Bloch domain wall (BW) width with respect to the island size. Annealing of the as-grown film (a) results in island sizes comparable to the BW width (b).

adjacent energy barriers and higher fields are necessary for wall displacement. Repeating the annealing cycle does not further change the island size. The resulting dependence of $H_C(T_a)$ (dashed line) is characteristic for a thermally activated overcoming of the energy barriers.

3.2 Temperature dependence of the magnetization reversal process

3.2.1 Magnetic after-effect

The results discussed in the Sec. 3.1 show clearly that the coercivity is determined by the distribution of energy barriers which mainly originate from the microstructure of the film, such as the Fe islands. Detailed information about the potential energy surface (PES) in Fe/Cu(100) can be obtained by measuring the time dependence of the magnetization reversal process for applied fields $H < H_C$ as a function of temperature [130].

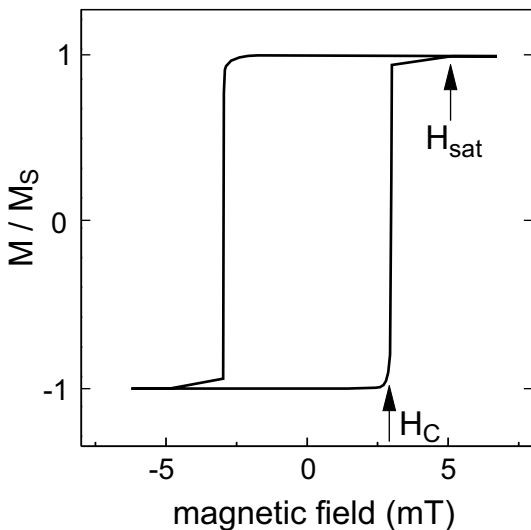


Figure 3.6: MOKE magnetization loop of 3 ML Fe/Cu(100) at 120 K.

The experimental parameters for the after-effect measurements, that are the pre-magnetization field, H_{pre} , and the coercivity, H_C , are chosen from MOKE hysteresis loops recorded prior to the experiment. A characteristic MOKE loop for 3 ML Fe/Cu(100) at 120 K is shown in Fig. 3.6. Typically, at H_C a magnetization somewhat smaller than the saturation magnetization, M_S , is achieved. A saturation field of $H_{sat} \sim 2H_C$ is required to achieve the fully saturated magnetization state, leading to characteristic tails in the hysteresis loop. It will be shown in the Sec. 3.2.2 by means of domain images that these tails are due

to the formation of 360° domain walls which slow down the magnetization reversal process.

Prior to the viscosity experiment, the sample is magnetized by an external field of $H_{pre} = +1.05 \times H_C$, to achieve a well-defined initial magnetization state, where domains of opposite magnetization are already nucleated. At $t = 0$, a field of opposite direction,

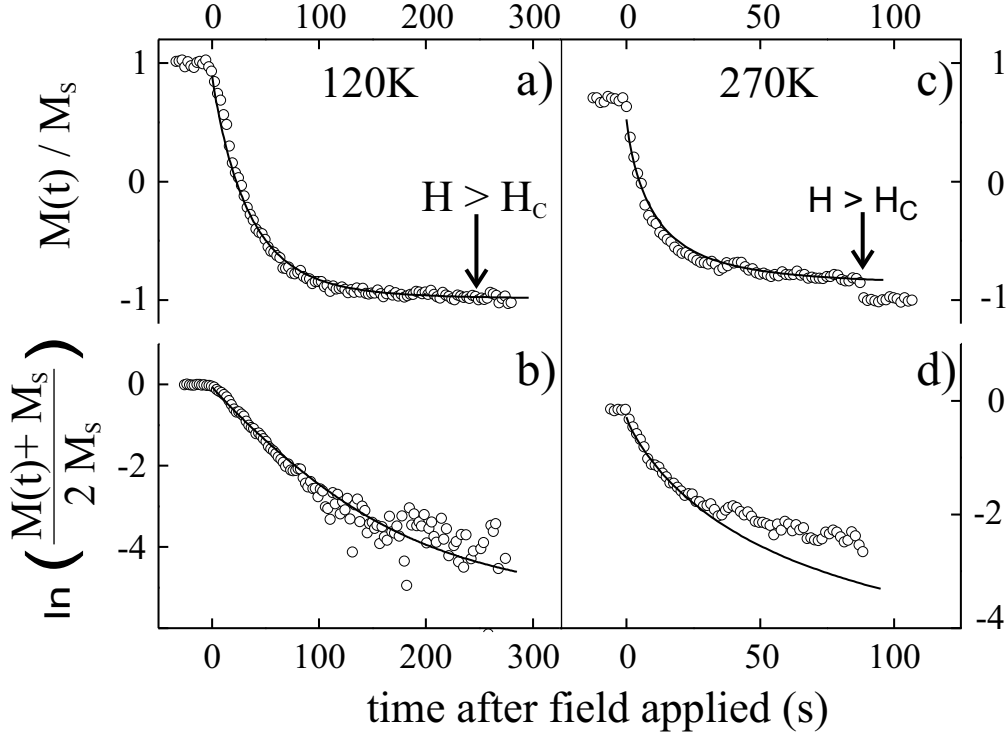


Figure 3.7: Magnetic after-effect of 3 ML Fe/Cu(100). (a,b) $T = 120\text{ K}$, $H = -0.74 \times H_C$, (c,d) $T = 270\text{ K}$, $H = -0.77 \times H_C$.

$-H_C < H < 0$, is applied and kept constant for the duration of the experiment. The evolution of the sample magnetization with time, $M(t)$, is recorded with MOKE measurements. At the end of the experiment, the field is increased above H_{sat} to achieve the opposite saturated magnetization state as reference.

The time dependent MOKE signal measured on 3 ML Fe at 120 K is shown in Fig. 3.7(a). At $t = 0$ an external field of $H = -3.2\text{ mT} = 0.74 \times H_C$ was applied. The magnetization reverses from $+M_\infty$ to $-M_\infty$ as a function of time due to thermally activated domain wall propagation. As was shown in previous work [52], the time dependence $M(t)$ can be described by the following expression:

$$M(t) + M_\infty = 2M_\infty \exp\left(-\frac{t}{\tau}\right) \quad (3.3)$$

The M_∞ refers to the equilibrium or anhysteretic magnetization, and of course depends to some extent on the H_{pre} . The exact value for M_∞ is not known, but a reasonable approximation is given by $M_\infty = M_S$. The time constant τ should follow an Arrhenius law:

$$\tau = \tau_0 \exp\left(\frac{E_A}{k_B T}\right) \quad (3.4)$$

and can be obtained by fitting $M(t)$. The measurements in Fig. 3.7 are performed as a function of H , and the τ for each experiment is determined. The obtained data for $\ln \tau(H)$, measured at 120 K, are plotted as a function of field in Fig. 3.8. The data show linear dependence on H . The slope is directly related to the activation energy:

$$\ln \tau = \ln \tau_0 + \frac{E_A}{k_B T} \quad (3.5)$$

which has to be a function of field if $\ln \tau_0$ is assumed to be field independent:

$$E_A = M_S V_B (H + H_P) \quad (3.6)$$

This expression is valid for $-H_P \leq H \leq 0$. In this equation the propagation field H_P is introduced. It corresponds to the field needed without any activation process, and reflects the local slope of the PES, as was thoroughly discussed in Ref. [52]. Temperature dependent measurements of $M(t)$ should in principle yield H_P , as will be discussed later in this paper.

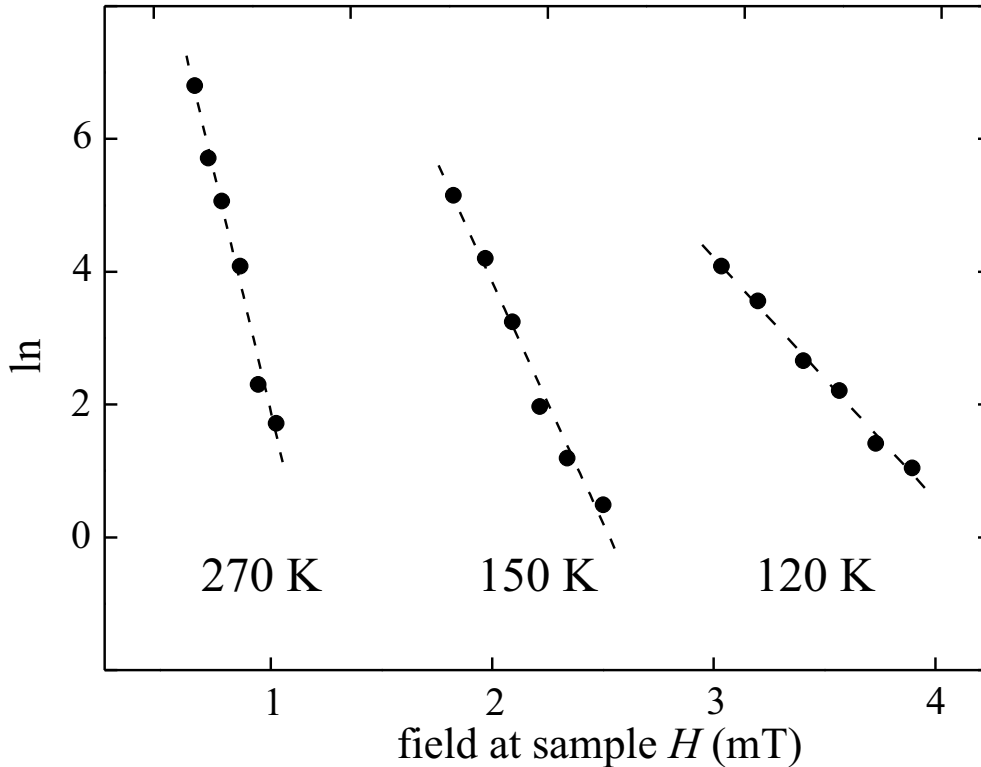


Figure 3.8: Relaxation times as a function of temperature, for 3 ML Fe/Cu(100) grown at 127 K.

By substituting E_A , the Eq. 3.5 becomes:

$$\ln \tau = \ln \tau_0 + \frac{M_S V_B H_P}{k_B T} + \frac{M_S V_B}{k_B T} H = y_0 + \alpha H \quad (3.7)$$

with $\alpha = M_S V_B / k_B T$, corresponding to the slope of the data in Fig. 3.8. It directly yields the Barkhausen volume, V_B . For two-dimensional systems, such as the monolayer thin films presented here, it is more appropriate to use the expression "Barkhausen length", l_B , rather than the volume. The film thickness, t_F , is required for conversion:

$$l_B = \sqrt{\frac{V_B}{t_F}} \quad (3.8)$$

Following this recipe, a Barkhausen length of $l_B = 80 \text{ nm}$ is determined for the 3 ML Fe film on Cu(100) at 127 K.

Temperature dependent measurements of the magnetic after-effect are performed between 127 K and 300 K to obtain l_B as a function of temperature. Since the coercivity changes with temperature (see Fig. 3.4), smaller external fields are necessary to reverse the magnetization in the sample with increasing T . The recorded $M(t)$ at 270 K is shown in Fig. 3.7(c). Here, at $t = 0$ the field $H = -0.95 \text{ mT} = 0.77 \times H_C$ was applied. As in the measurement at 120 K the magnetization reverses as a function of time. The main difference between both measurements is that the magnetization is almost completely reversed at 120 K at the end of the experiment, while at 270 K the $M(t = \infty)$ remains significantly smaller than M_S at 270 K.

The l_B as a function of T is shown in Fig. 3.9 for 3 ML Fe grown at 127 K (\bullet), 3 ML Fe grown at 300 K (\circ) and 2 ML Fe grown at 127 K (\square). The data show that: (i) the Barkhausen length is a linear function of temperature. We find for 3 ML Fe grown at 127 K an increase by a factor of 3, from $l_B = 80 \text{ nm}$ at 127 K up to 240 nm at 296 K. The temperature dependence is fully reversible; after cooling the sample from $T_a = 300 \text{ K}$ down to 127 K the $l_B = 80 \text{ nm}$ is again found. The reversible increase of the measured Barkhausen length is a result of the reduced effective barrier height at elevated temperatures. (ii) As a tendency, l_B increases with film thickness. (iii) The preparation condition influences l_B only a little. The atomically flat, high quality Fe films prepared at 300 K show a l_B only slightly larger than that one of the rough Fe films grown at 120 K. On the first glance, this results might suggest that the Barkhausen length is not determined by the morphology of the film. A possible explanation could be an avalanche-like switching of many volumes, i.e. a domain wall overcomes ballistically many energy barriers once it is in motion, after the activation event. The measured l_B

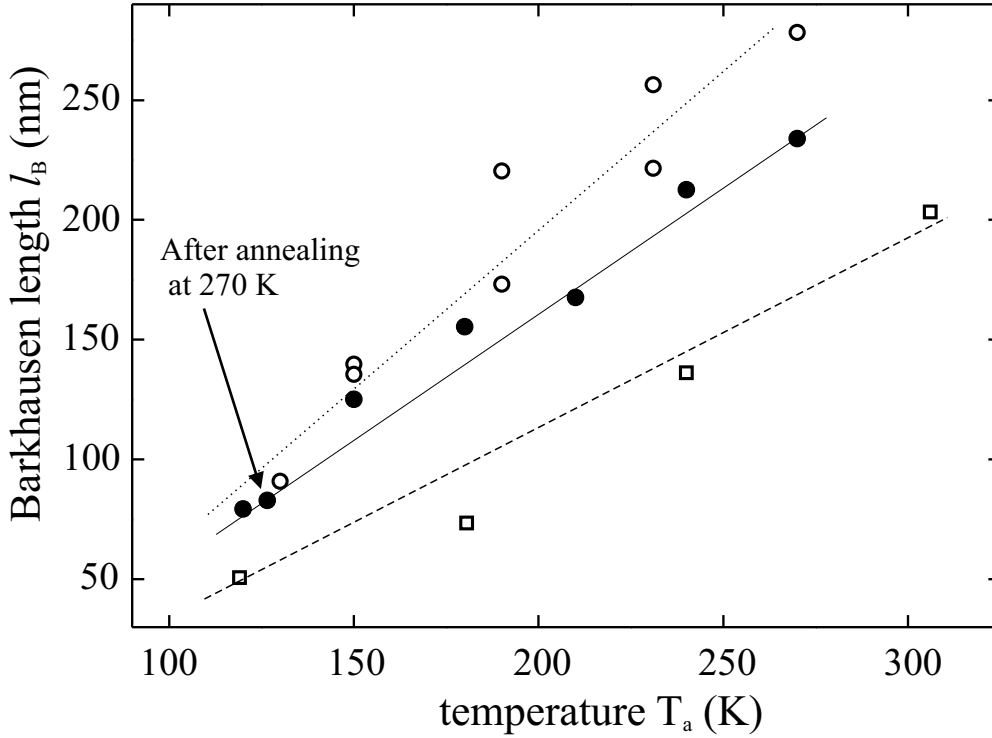


Figure 3.9: Temperature dependence of the Barkhausen length, l_B , for Fe/Cu(100): 2 ML Fe grown at 127 K (\square), 3 ML Fe grown at 127 K (\bullet), 3 ML Fe grown at 300 K (\circ).

is therefore much larger than the intrinsic Barkhausen length, l_B^* , determined by the morphology, and thus insensitive to barriers on the atomic scale. As a consequence, changes in the film morphology during annealing influence the measured l_B only a little, if at all.

3.2.2 The magnetization reversal process

Details about the magnetization reversal process are revealed by in-situ Kerr microscopy. The sequence of Kerr images in Fig. 3.10 shows the propagation of magnetic domains in 3 ML Fe during a viscosity measurement at 131 K. The dark/bright contrast in the images corresponds to magnetic domains in the film with opposite magnetization along the film normal. The elapsed time after the external magnetic field was applied is indicated within the images. Already nucleated domains barely visible at $t = 0$ s start to grow with time, until the magnetization is almost completely reversed. As the Bloch walls of adjacent domains approach each other, they are unable to merge, which slows down and finally stops the reversal process. Small lines of original magnetization of width $d \approx 5 \mu\text{m}$ remain. These non-reversed areas of original magnetization are the result of the formation of 360° walls out of two adjacent 180° Bloch walls, as discussed

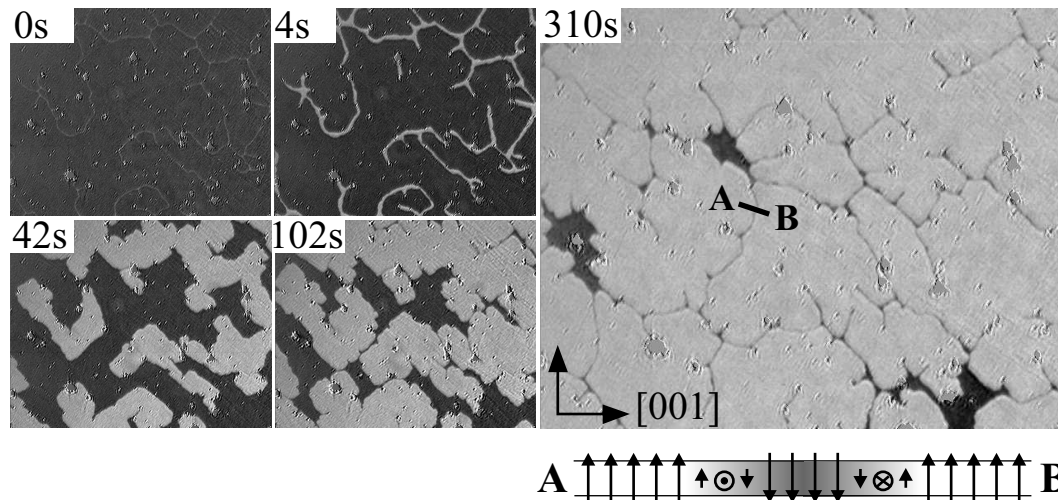


Figure 3.10: Evolution of the magnetization of 3 ML Fe/Cu(100) at 131 K after a magnetic field of $H = -0.97 \text{ mT}$ was applied at $t = 0 \text{ s}$. After 310 s narrow lines of original magnetization remain due to the formation of 360 degree walls preventing the fully saturated opposite magnetization state. Image size: $400 \mu\text{m} \times 300 \mu\text{m}$.

by Bauer *et al.* for the case of Ni/Cu(100) [56]. Removal of these walls is energy-costly. A field almost twice the coercivity is required to form a fully saturated single domain state, leading to the characteristic tails in the magnetization loop in Fig. 3.6.

The Kerr images clearly show that the magnetization reversal is a propagation dominated process. The activation energy for domain nucleation is significantly larger than the activation energy for wall propagation.

For a more compact and informative presentation of the time evolution of the domain state, the sequence in Fig. 3.10 is reduced into the color-coded chart in Fig. 3.11(a). The colors represent subsequent areas occupied by the domains of majority magnetization at the indicated time interval. For comparison, the magnetization reversal at 131 K (Fig. 3.11(a)) and 291 K (Fig. 3.11(b)) are shown. At low temperature the domain walls propagate continuously in all directions. The propagation velocity is determined by the in-plane anisotropy of the Fe, thus the domain shape reflects a four-fold symmetry after some time. The nucleation sites for the domains are determined by macropins on the surface.

The domain propagation changes completely at elevated temperature (Fig. 3.11(b)). Here, the four-fold in-plane anisotropy does not show up in the domain shape. More strikingly, the wall propagation is discontinuous. On many positions, such as those ones marked by arrows, the domain propagation grinds to a halt and proceeds jump-like only after a long pause. The transition from continuous to discontinuous wall propagation indicates a change in the activation process due to competing pinning mechanisms

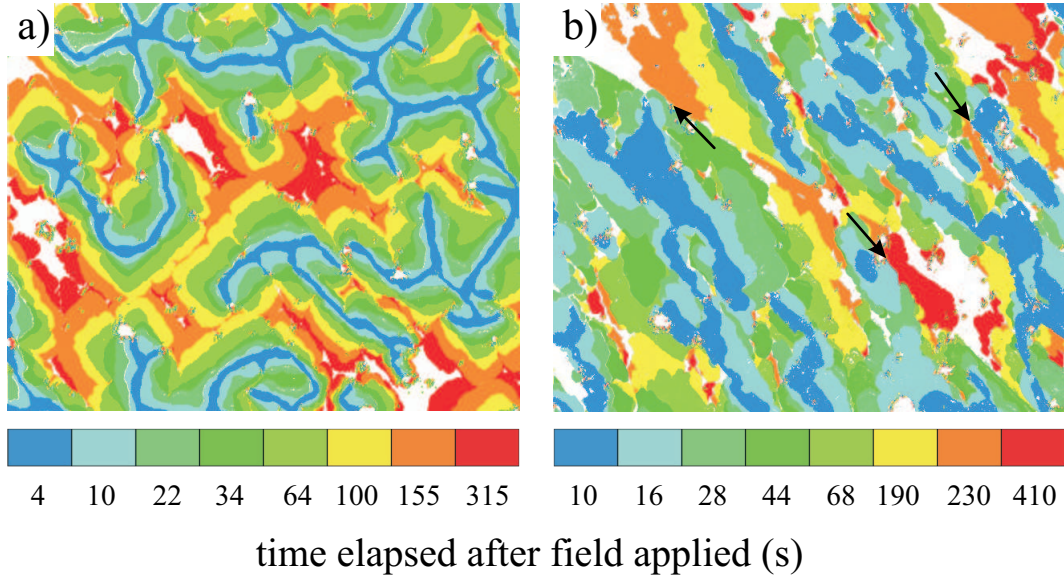


Figure 3.11: Comparison of the domain wall propagation in 3 ML Fe/Cu(100) within a constant field at 131 K (left) and 291 K (right). The evolution of the domain size with time is color-coded. Image size: $400 \mu\text{m} \times 300 \mu\text{m}$.

predominant at different temperatures.

The sequence of Kerr images in Fig. 3.10 reveals that besides the micropins, which are intrinsic defects in the film correlated with its morphology, also macropins significantly influence the domain propagation. Such macropins are extrinsic defects spatially distributed on a $10 - 50 \mu\text{m}$ scale and directly recognizable in the Kerr images [57]. They visibly act as pinning centers for the domains. As can be seen, these macropins provide insurmountable obstacles in the temperatures range up to 300 K. As was discussed already in Sec. 3.1, bcc-crystallites are formed within the fcc-Fe during cycling of temperature. These crystallites do not only change the anisotropy, but also introduce new energy barriers into the potential energy surface (PES) and might add additional pinning centers. Hence, the dominating wall pinning mechanism changes with temperature. As a result, a transition from continuous to discontinuous wall propagation at $\approx 250 \text{ K}$ is observed, when the micropins provided by the Fe islands become unimportant compared to the macropins.

3.2.3 Energy barriers and relaxation times

The data on the film structure, the magnetic after-effect and the domain wall propagation will be compared in the following to obtain the determining parameters for the magnetization process. The calculation of the activation energies, E_A , requires the intrinsic propagation field H_P (Eq. (3.6)), which can be deduced from the field and

temperature dependent measurement of the relaxation times in Fig. 3.8. The intercept y_0 of each fit with the y-axis at $H = 0$ is according to Eq. (3.7):

$$y_0 = \ln(\tau_0) + \frac{M_S V_B H_P}{k_B T} \quad (3.9)$$

From the temperature dependence of y_0 a system of equations is obtained with H_P as one solution. For the Fe/Cu(100) in Fig. 3.8 the y_0 turns out to be constant for all measurements, and thus independent on T . The slope, α , on the other hand, is clearly a function of T . A solution for H_P other than $H_P = 0$ can therefore not be found. This means that the intrinsic propagation field itself changes with temperature. This proposed dependence, $H_P(T)$, is independent of the film structure since identical values for α and y_0 are found after repeating annealing cycles for the same film. Although H_P can not easily be calculated within this model, we can say that H_P has to depend inversely and reversibly on T .

To circumvent the difficulty of determining H_P we consider relaxation times, τ , rather than activation energies in the following. The relaxation times can be determined from the experiment directly and are equivalent to the activation energies, with the advantage that H_P and τ_0 are not required.

We use an approach introduced by Bruno *et al.* to obtain the distribution of τ as a function of field [51]. Starting from Eq. (3.3), the viscosity measurements in Fig. 3.7(a,c) are plotted as the logarithm of $(M(t) + M_S)/2M_S$. In such a presentation the data should depend linearly on t if there was no distribution of τ . As can be seen in Fig. 3.7(b,d), this is clearly not the case here. The data are therefore approximated by assuming a Lorentz distribution of τ :

$$\sigma(\tau) = \frac{\Gamma}{2\pi[(\tau - \tau^*)^2 + (\Gamma/2)^2]} \quad (3.10)$$

The τ -distribution of width Γ is centered around τ^* . At a time t the total magnetization of the sample exposed to the field $H < H_C$ is the sum of the magnetization of all Barkhausen volumes with Lorentz-distributed τ :

$$M(t) = 2M_\infty \int_0^\infty \sigma(\tau) \exp\left(-\frac{t}{\tau}\right) d\tau - M_\infty \quad (3.11)$$

The resulting fit to the viscosity measurement at 120 K, shown in Fig. 3.7(a) and (b) as a solid line, is in fairly good agreement with the data. The distribution $\sigma(\tau)$ determined

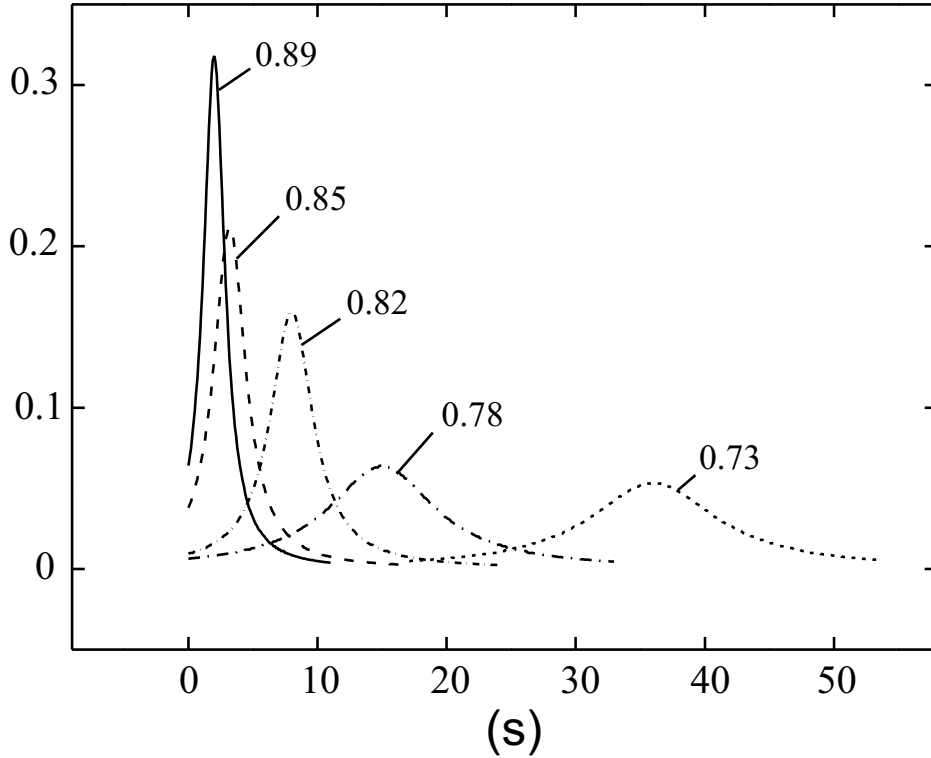


Figure 3.12: Distribution of τ for 3 ML Fe/Cu(100) at 120 K for different H/H_C .

from the data at 120 K as a function of field are shown in Fig. 3.12. The ratios H/H_C are indicated in the figure. One can see that the closer the field to H_C the smaller the parameters τ^* and Γ of the fitted distribution.

The model yields a good description of the viscosity at 120 K, but it fails to describe the measurements at higher sample temperatures: although a satisfying fit to $M(t)$ can be achieved (Fig. 3.7(b)), the same fit matches the data in the logarithmic presentation in Fig. 3.7(d) only in the early stage of the experiment. As time elapses the discrepancy between the viscosity data and the fit from the applied model becomes significant. This discrepancy is clearly related to the transition from continuous to discontinuous wall propagation at ≈ 250 K, when additional pinning centers with different sensitivity to temperature are present (see previous subsection). The applied theoretical model does not consider competing activation mechanisms and therefore works best at low temperatures, where the micropins govern the magnetization reversal. A theoretical description of the viscosity experiments is only possible for continuous wall propagation as found at low temperatures. The Kerr images in Fig. 3.11 visualize the difference between the magnetization reversal process at low and room temperature, and help further to explain the failure of the model at higher temperatures.

The Fe islands have been found to dominantly shape the potential energy surface,

which is seen by a domain wall during the magnetization reversal process. Thus, the PES is providing the link between structure and important magnetic properties.

The activation energy could not be calculated directly within this work due to the difficulties in determining the intrinsic propagation field. However, a rough approximation for H_P can be obtained by assuming $H_P = H_C(T = 0)$. Extrapolation from Fig. 3.4 gives $H_P \simeq 36 \text{ mT}$, resulting in $E_A \simeq 1 \text{ eV}$. This value is comparable to the activation energy found for Ni/Cu(001) with $E_A \simeq 0.7 \text{ eV}$ [56], or for Au/Co/Au films where $E_A \simeq 0.9 \text{ eV}$ [51]. It is interesting to note that the activation energy is thus orders of magnitude larger than the thermal energy ($\sim 10 \text{ meV}$) and the field energy ($\sim 0.3 \mu\text{eV}$). The observed relaxation times on the other hand suggest that the ratio between the activation energy and the barrier height must be smaller than 1:10. This discrepancy suggests that the model for the calculation of E_A provides only an estimate. The result underlines the importance of the attempt rate of a spin to overcome energy barriers, besides the barrier height itself, for the magnetization reversal process.

Chapter 4

Coupled perpendicular magnetization in Fe/Cu/Fe trilayers

I have used fcc-Fe films on Cu(100) as templates for the fabrication of fcc-Fe/Cu/Fe trilayers. The structure of these films is studied by LEED and Reflection High Energy Electron Diffraction (RHEED). The magnetism is investigated in-situ by integral MOKE measurements and Kerr microscopy.

Perpendicular coupling between the Fe layers and magnetic domain formation have been found and ascribed to a magneto-static interaction [131]. Furthermore, the governing role of the Fe-vacuum interface for the magnetism of the whole trilayer is demonstrated by oxygen adsorption experiments [132].

4.1 Fabrication of fcc-Fe/Cu/Fe trilayers

Fe films were grown by molecular beam epitaxy with deposition rate of 0.3-0.5 ML/min, as calibrated with the quartz microbalance. The substrate was held at RT during Fe deposition for *both* layers and cooled to 125 K for deposition of the Cu spacer layer. However, Cu spacer layers have been also deposited at RT and no significant changes were observed in the magnetic properties of the systems.

The fcc-structure of the Fe/Cu/Fe trilayer is confirmed by LEED performed during the fabrication (Fig. 4.1). The characteristic first-order diffraction spots of the clean fcc-Cu(100) surface are visible in Fig. 4.1(a). The deposition at RT of 3 ML Fe does not substantially alter the LEED pattern (Fig. 4.1(b)). Only the background intensity has increased a little, probably due to some structural disorder of the film. The position of the spots does not change after the deposition of 3 ML Cu at LT and of the second Fe layer on top (Fig. 4.1(c,d)). Only weak broadening of the spots is observed, in particular

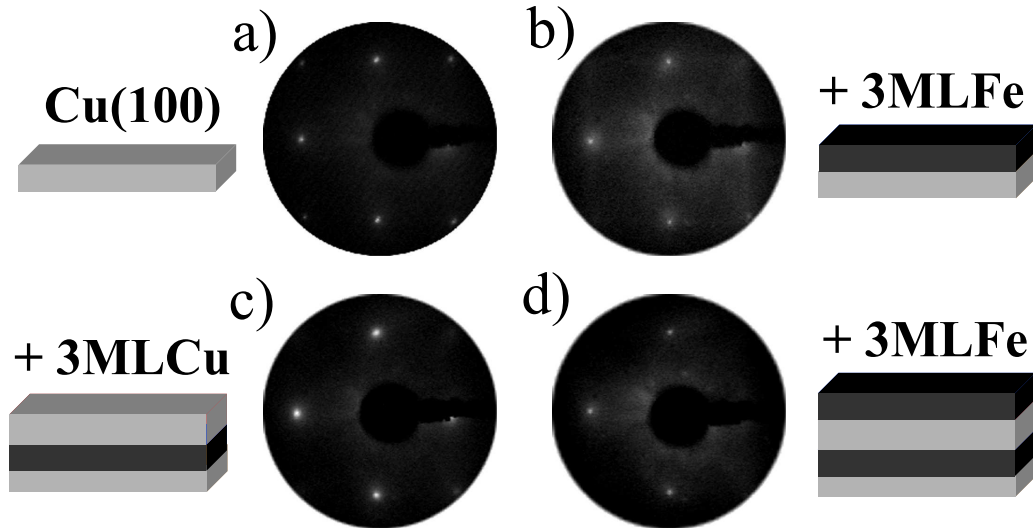


Figure 4.1: LEED images taken at 156 eV on: clean Cu(100) substrate (a), 3 ML Fe/Cu(100) (b), 3 ML Cu/3 ML Fe/Cu(100) (c), 3 ML Fe/3 ML Cu/3 ML Fe/Cu(100) (d).

after the growth of the Cu spacer layer. The LEED data thus show that heteroepitaxial Fe/Cu/Fe trilayers on Cu(100) substrate with fcc-structure are formed. This structure is favored because the epitaxial strain is small. Assuming a lattice constant of fcc-Fe, $a_{fcc}^{Fe} = 3.59 \text{ \AA}$ [120], and of Cu, $a_{fcc}^{Cu} = 3.61 \text{ \AA}$, the tensile strain in the first Fe layer results to be only of 0.6%!

In collaboration with Heinrich's group (Simon Fraser University, Burnaby, BC, Canada), we have furthermore investigated the growth mode of the films by RHEED. The results indicate that a layer-by-layer growth only occurs for the first atomic layers. During the deposition of 6.5 ML Fe on Cu(100), the specular spot signal intensity is recorded as a function of time, which is equivalent to the amount of Fe deposited on the substrate. Is it possible to associate to each oscillation in the signal intensity the formation of one atomic layer. A perfect layer-by-layer growth would show all maxima with the same intensity. We have found for Fe/Cu(100) that the oscillation amplitude decays with coverage and only up to 4 oscillations are visible. Above 4 ML thickness, a transition from layer-by-layer to three dimensional (3D) growth occurs. Oscillations of only small amplitude can be identified during the subsequent deposition of 6 ML Cu first and 9 ML Fe afterwards on top of the 6.5 ML Fe/Cu(100). Such small RHEED oscillations are attributed to increasing surface roughness of the the first Fe layer (6.5 ML).

The evolution of the magnetic anisotropy of the films after the deposition of each

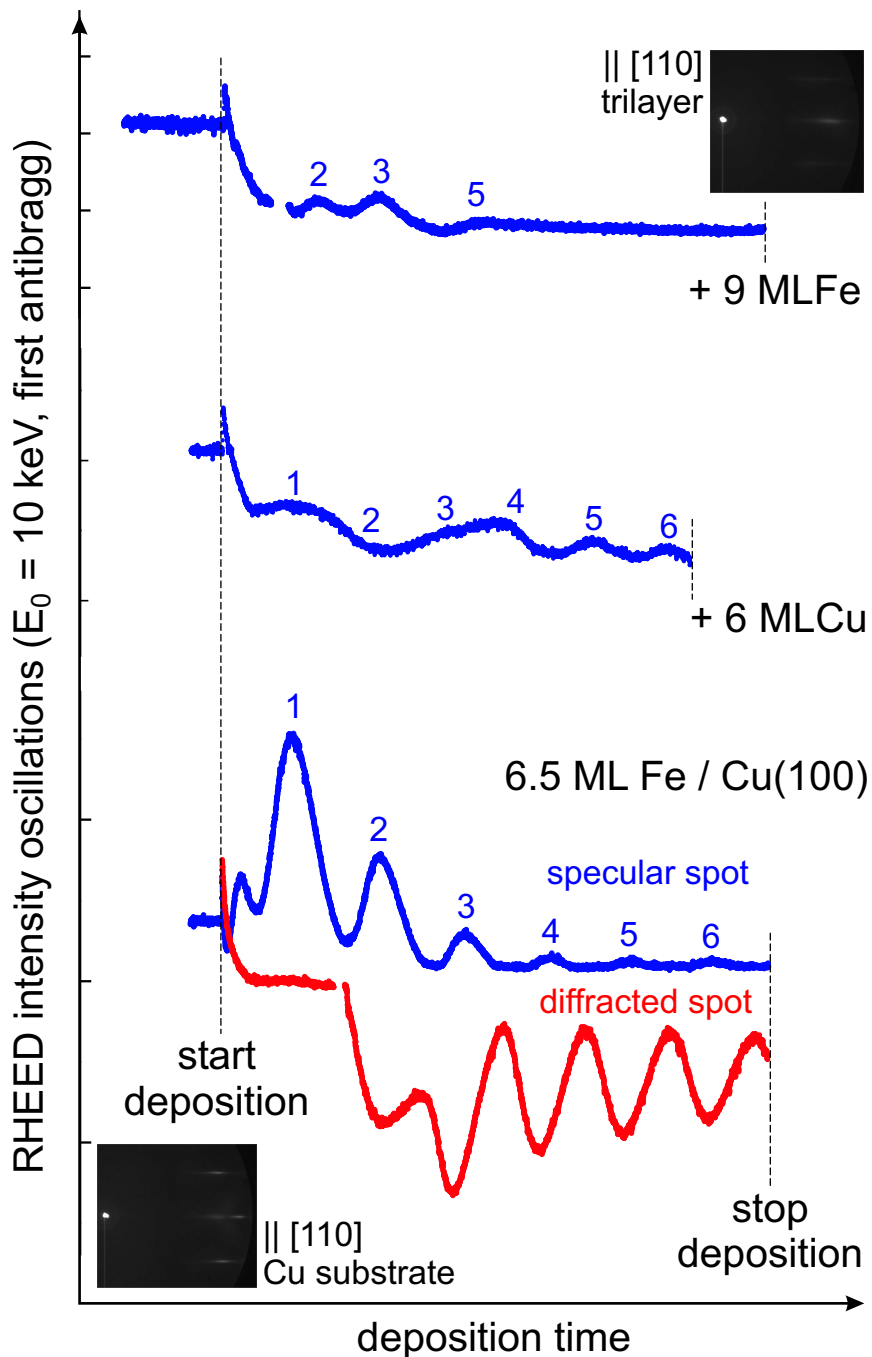


Figure 4.2: RHEED measurements taken during the fabrication of Fe/Cu/Fe trilayers. Specular spot signal intensity recorded as a function of time during the deposition of: 6.5 ML Fe/Cu(100) at RT, 6 ML Cu on 6.5 ML Fe/Cu(100) at RT, 9 ML Fe on 6 ML Cu/6.5 ML Fe/Cu(100) at RT. *In collaboration with O. Mosendz, B. Kardasz, and B. Heinrich, Simon Fraser University, Burnaby, BC, Canada*

individual layer of the Fe/Cu/Fe trilayer is summarized in Fig. 4.3. The hysteresis loop of 3 ML Fe/Cu(100) grown at RT in Fig. 4.3(a), as observed by a polar MOKE loop taken at 110 K, shows the known result of perpendicular magnetization of this system. The deposition of 2 ML of Cu on top of this film causes a spin reorientation into the plane, as concluded from the longitudinal MOKE loop in Fig. 4.3(e) and the absence of a polar Kerr signal (Fig. 4.3(b)). A detailed study of this spin reorientation as a function of the Cu thickness is given in the Sec. 4.1.3. The easy axis of magnetization switches again out-of-plane after the deposition of the second Fe layer of 3 ML thickness. The magnitude of the observed polar Kerr signal in Fig. 4.3(c) is approximately twice the signal of the 3 ML Fe in Fig. 4.3(a) and thus corresponds to the sum of the signals of both individual Fe layers. Clearly, it is the presence of the top Fe layer that induces a

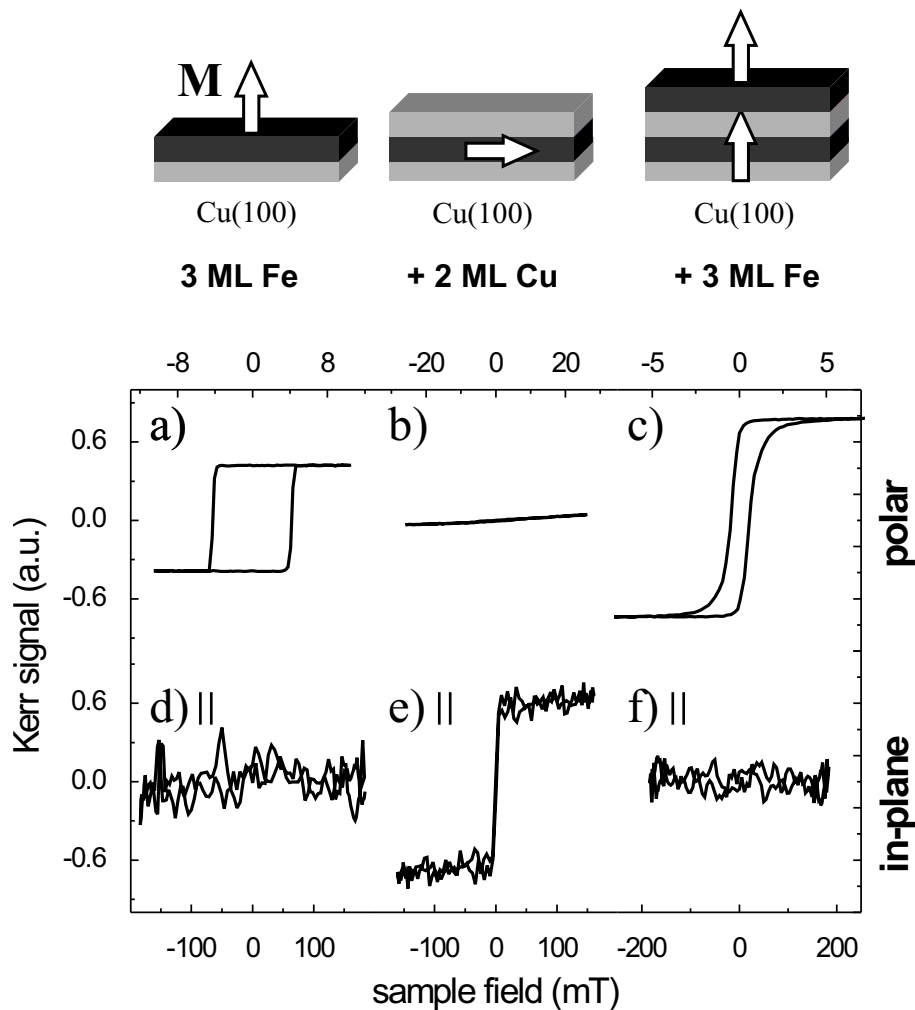


Figure 4.3: Polar (a-c) and longitudinal (d-f) MOKE hysteresis loops of 3 ML Fe (a,d), 1 ML Cu/3 ML Fe (b,e), 3 ML Fe/1 ML Cu/3 ML Fe (c,f) films on Cu(100).

perpendicular magnetization also in the bottom Fe layer. On the trilayer, no in-plane magnetic signal was recorded (Fig. 4.3(f)).

I have investigated the dependence of the trilayer magnetization on the thickness of the Fe layers and the Cu spacer. The results are presented in the following sections.

4.1.1 Bottom Fe layer of variable thickness

The magnetization of the trilayer was investigated first as a function of the bottom Fe layer thickness, t_1 , with the thickness of the top Fe layer, t_2 , and of the Cu spacer, t_{Cu} , kept constant.

A wedge of $t_1 = 0-15$ ML Fe was grown at RT on Cu(100) and investigated by MOKE at 200 K. The remanent (\blacktriangle) and saturation (\triangle) Kerr signals of polar MOKE loops as a function of t_1 are shown in Fig. 4.4. The well-known magnetic phase transitions from

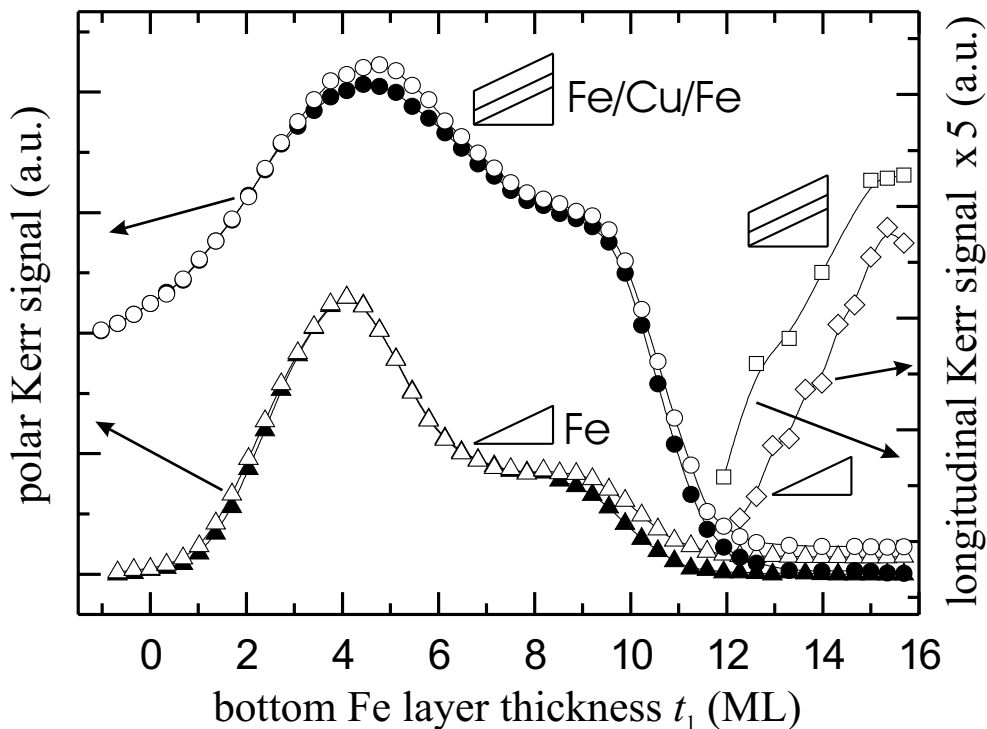


Figure 4.4: Polar remanent (\blacktriangle), polar saturation (\triangle) and longitudinal saturation (\diamond) Kerr signals of MOKE loops of a t_1 ML Fe-wedge grown at RT on Cu(100), as a function of the Fe thickness, t_1 . Polar remanent (\bullet), polar saturation (\circ) and longitudinal saturation (\square) Kerr signals of MOKE loops of a 3 ML Fe/2 ML Cu/ t_1 ML Fe/Cu(100) trilayer as a function t_1 , taken at 90 K.

FM polar to partly antiferromagnetic (AF) polar ordering at ~ 4 ML and to in-plane magnetization (\diamond) at $t_1 \sim 12$ ML can be recognized [75]. For $4 \text{ ML} < t_1 < 12 \text{ ML}$, only the two top Fe atomic layer are coupled with the magnetization pointing out-of-plane, whereas the other layers are antiferromagnetically coupled giving a zero net MOKE signal. Above 12 ML the magnetization reorients into the plane. The polar saturation signal (Δ) drops to zero since the available field was not sufficient to saturate the film along the hard magnetization axis. By applying an in-plane magnetic field, square hysteresis loops were obtained, thus indicating an easy magnetization axis within the film plane. The longitudinal MOKE signal (\diamond) linearly increases as a function of t_1 .

Based on this sample, a trilayer of 3 ML Fe/2 ML Cu/ t_1 ML Fe/Cu(100) was formed. The polar (\bullet) and saturation (\circ) Kerr signal, measured at 90 K, of the trilayer in Fig. 4.4 is clearly the sum of the signal of the Fe wedge plus a constant offset corresponding to the contribution of the top Fe layer. Since the Cu covered Fe wedge showed in-plane magnetic anisotropy, it is obvious that the top Fe layer controls the anisotropy in the bottom Fe layer. Both layers are ferromagnetically coupled and exhibit perpendicular magnetization for all thickness $t_1 < 12$ ML. However, although the magnetic interaction is sufficient to align out-of-plane the magnetic moments of the two top most atomic layers of the bottom layer, it does not influence the AF arrangement. Above $t_1 = 12$ ML, both layers show in-plane magnetization (\square). The structure of the top Fe layer, and hence the magnetic anisotropy, is probably influenced by a transition from fcc to bcc in the structure underneath [18].

4.1.2 Top Fe layer of variable thickness

To further probe the role of the top Fe layer on the total magnetic anisotropy of the trilayer, samples with varying top layer thickness, t_2 , and constant t_1 and t_{Cu} were analyzed. For the MOKE measurements at 135 K shown in Fig. 4.5, a Fe wedge of $t_2 = 0 - 4$ ML was grown at RT on top of a 2 ML Cu/3 ML Fe bilayer. The top Fe layer causes perpendicular magnetization in the trilayer, after in-plane anisotropy was observed for the Cu/Fe bilayer. The polar remanent (\bullet) and saturation (\circ) Kerr signals of the trilayer are shown in Fig. 4.5(a). The data clearly show that: (i) For $t_2 > 1.3$ ML Fe, the saturation signal (\circ) of the trilayer is larger than the polar MOKE signal of the Fe bottom layer (Δ and dashed line). This means that also the magnetization in the bottom layer partially contributes to the polar MOKE signal of the trilayer. (ii) For $t_2 > 2$ ML Fe, the intensity of the Kerr signal of the trilayer corresponds to the sum of the signals of both individual Fe layers, assuming a linear proportionality between the thickness of the Fe layers and the MOKE signal. The magnetizations of the two layers

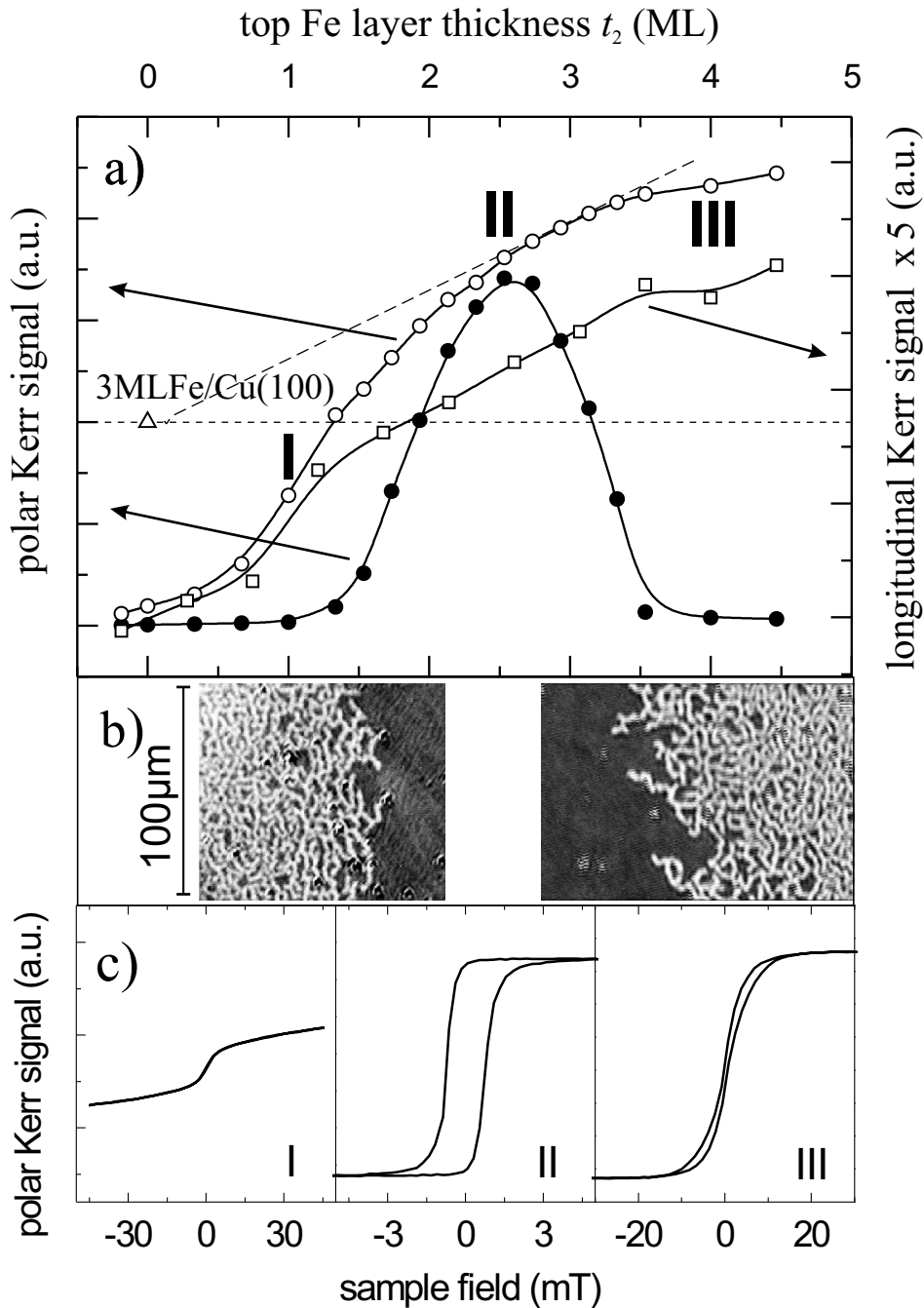


Figure 4.5: (a) Magnetization of a trilayer, t_2 ML Fe/2 ML Cu/3 ML Fe/Cu(100), as a function of the top Fe layer thickness, t_2 . Remanent (\bullet) and saturation (\circ) Kerr intensities of polar MOKE loops before O_2 adsorption, taken at 135 K. Saturation (Δ and dashed line) Kerr intensity of polar MOKE loop of 3 ML Fe/Cu(100) (bottom Fe layer). Saturation (\square) Kerr intensity of longitudinal MOKE loops after O_2 adsorption. (b) Kerr images of the remanent state at $t_2 = 2.5$ ML (left) and $t_2 = 3.5$ ML (right) taken at 140 K on a similar sample. (c) Polar MOKE hysteresis loop of: $t_2 = 1$ ML (I), $t_2 = 2.5$ ML (II), $t_2 = 4$ ML (III) on 2 ML Cu/3 ML Fe/Cu(100).

are aligned out-of-plane. Extrapolation of the saturation to $t_2 = 0$ yields the polar Kerr signal of the bottom layer. (iii) Saturation and remanence have the same value only in the thickness range between $2.2 \text{ ML} < t_2 < 2.8 \text{ ML}$. Within this thickness range, square shaped hysteresis loops are observed (Fig. 4.5(II)) and clearly prove that the easy axis of magnetization for the whole trilayer is perpendicular. The magnetizations of the two Fe layers are ferromagnetically coupled. Outside this region, S-shaped magnetization loops were measured (Fig. 4.5(I) and (III)). For $t_2 > 3.5 \text{ ML Fe}$ and $t_2 < 1.5 \text{ ML Fe}$ the remanence is zero. This thickness region of t_2 strongly depends on the relative thickness t_1, t_2, t_{Cu} and on the sample temperature. By lowering the temperature, the interval of t_2 in which remanence and saturation have the same value becomes broader.

A spin reorientation of the whole trilayer into the plane was observed for $t_2 > 5.7 \text{ ML}$. This thickness represents the critical thickness for perpendicular magnetization in the top Fe layer when grown on the Cu/Fe bilayer and, as a consequence, in the bottom layer as well.

In-situ Kerr microscopy was used to analyze the magnetization of the trilayer more in detail. The Kerr images in Fig. 4.5(b) were taken at 140 K on a similar sample. They show the magnetic domain configuration of the remanent state at position corresponding to a top layer thickness of around $t_2 = 2.5 \text{ ML}$ (left) and $t_2 = 3.5 \text{ ML}$ (right) at the center of each image. Within these images the t_2 is increasing from left to right by $\sim 0.2 \text{ ML}$. The black and the white contrast in the image represents magnetic domains with opposite magnetization perpendicular to the plane. At $t_2 < 2 \text{ ML}$ and $t_2 > 2.8 \text{ ML}$ a transition from single domain magnetization state to a multi-domain state with domains of a few micrometers in size is observed. The appearance of S-shaped magnetization loops can thus be identified as the result of the formation of domains with zero net magnetization. Such a transition into a multi-domain state is not uncommon for single films with perpendicular anisotropy at a thickness just below the critical thickness, t_{crit} , for the spin reorientation transition into the plane [133]. It is the result of the competition between the energy needed to introduce domain walls, γ , and the gain of magneto-static energy, E_{shape} , when the sample's stray field is reduced. On the other hand, the domain state transition below 2.5 ML is unusual.

We observed that a transition towards a multi-domain state occurs if the t_2 is small compared to the bottom Fe layer thickness t_1 , as it is the case in Fig. 4.5 for $t_2 < 2 \text{ ML}$. The ratio t_1/t_2 seems to be decisive for the domain state. The total magnetic anisotropy energy, E_{tot} , of the trilayer is made up of the anisotropy energy contributions of *both* Fe layers. With increasing ratio t_1/t_2 , the E_{tot} is reduced due to the in-plane anisotropy contribution of the bottom layer. As a result, for large ratio t_1/t_2 the domain wall energy

$\gamma \sim \sqrt{A \cdot E_{tot}}$ becomes small and the formation of domains energetically favorable since it decreases E_{shape} . Domains are thus created in two cases: if t_1 is large compared to t_2 due to the reduced perpendicular E_{tot} , and for large t_2 close to t_{crit} due to the large E_{shape} .

4.1.3 Cu spacer of variable thickness

The coupling between two Fe layers is best investigated by varying the thickness of the Cu spacer, t_{Cu} . As shown already in Sec. 4.1, the deposition of a Cu layer on Fe films with perpendicular magnetic anisotropy causes a reorientation of the magnetization into the plane. In Fig. 4.6, polar MOKE loops of 2 ML Fe without (a) and with (b) the Cu layer are shown. After the deposition of the top Fe layer, the magnetization switches again out-of-plane, but the magnitudes of the resulting polar MOKE loops are different and depend on t_{Cu} (Fig. 4.6(c) and (d)).

To find out the amount of Cu needed to switch the easy axis of magnetization, I grew a Cu-wedge on a 3 ML Fe film, which exhibits perpendicular magnetic anisotropy. As

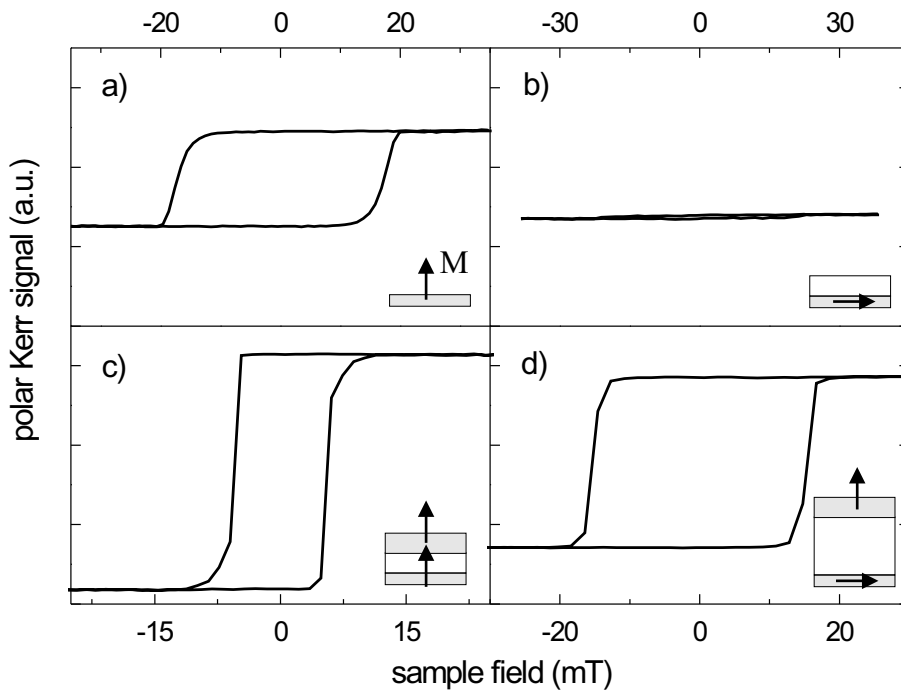


Figure 4.6: Polar MOKE hysteresis loop of: 2 ML Fe (a), 3.5 ML Cu/2 ML Fe (b), 3.5 ML Fe/3.5 ML Cu/2 ML Fe (c), 3.5 ML Fe/18 ML Cu/3 ML Fe (d) films on Cu(100).

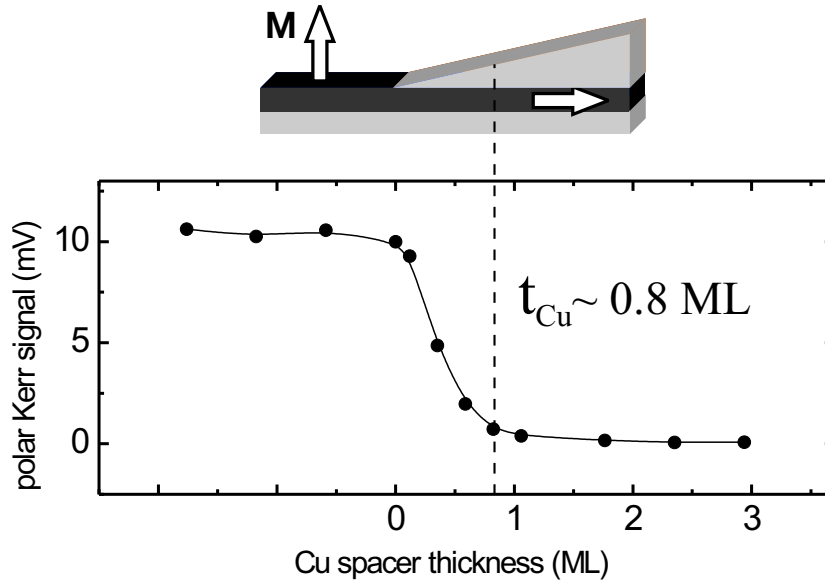


Figure 4.7: Saturation Kerr intensity of polar MOKE hysteresis loop of t_{Cu} ML Cu/3 ML Fe film on Cu(100).

shown in Fig. 4.7, just 0.8 ML of Cu is sufficient to reorient the magnetization of the film into the plane completely.

Although this is apparently in contrast with other experiments [27], it can be explained by a change in the magnetic surface anisotropy energy due to a modification of the electronic structure at the film-vacuum interface, as observed for Cu adsorption on Ni/Cu(100) [134] and on Co/Cu(100) [135,136]. The difference to the results by Vollmer *et al.* is probably due to different substrate and film morphologies, as discussed further in the following.

A 3 ML Fe/ t_{Cu} ML Cu/3 ML Fe/Cu(100) has been fabricated. In Fig. 4.8(a) we show the remanent (\bullet) and saturation (\circ) Kerr intensity of polar MOKE loops of the trilayer as a function of t_{Cu} . The Kerr signal increases with increasing t_{Cu} and reaches a maximum for $t_{Cu} \sim 2.5$ ML. Assuming a linear proportionality between the MOKE signal and the film thickness, the signal of 3 ML Fe/2.5 ML Cu/3 ML Fe corresponds to the sum of the signals of 3 + 3 ML Fe (which is not the same as 6 ML of Fe as a single layer!), approximately twice the intensity of polar loop taken on the bottom Fe layer (\square) Fig. 4.8(a)). We conclude that the magnetization of the Fe layers are coupled and aligned perpendicular to the plane. Then, the saturation and remanent signals decay with t_{Cu} and above a critical thickness $t_{crit} \sim 12$ ML the two layers are decoupled. The saturation signal is about the same of that one measured on the bottom layer (\square) Fig. 4.8(a)). Here only the top layer shows perpendicular magnetization and contributes

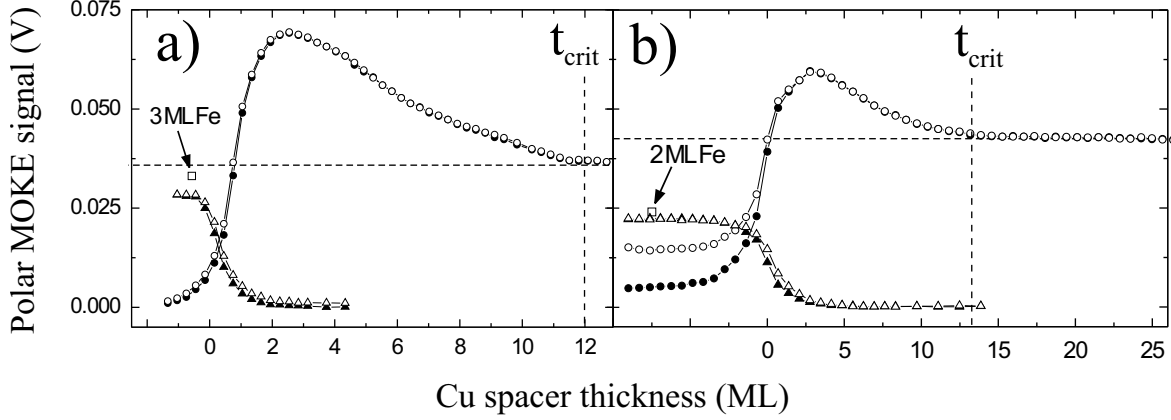


Figure 4.8: (a) Saturation (\square) Kerr intensity of polar MOKE loop of 3 ML Fe/Cu(100). Remanent(\blacktriangle) and saturation (\triangle) Kerr intensity of polar MOKE loops of t_{Cu} ML Cu/3 ML Fe/Cu(100) as a function of Cu spacer thickness, t_{Cu} . Remanent (\bullet) and saturation (\circ) Kerr intensity of polar MOKE loops of 3 ML Fe/ t_{Cu} ML Cu/3 ML Fe/Cu(100) as a function of t_{Cu} . (b) Saturation (\square) Kerr intensity of polar MOKE loop of 2 ML Fe/Cu(100). Remanent(\blacktriangle) and saturation (\triangle) Kerr intensity of polar MOKE loops of t_{Cu} ML Cu/2 ML Fe/Cu(100) as a function of Cu spacer thickness, t_{Cu} . Remanent (\bullet) and saturation (\circ) Kerr intensity of polar MOKE loops of 3.5 ML Fe/ t_{Cu} ML Cu/2 ML Fe/Cu(100) as a function of t_{Cu} .

to the observed polar MOKE signal, while the magnetization of the bottom layer lies in the film plane, as concluded from longitudinal MOKE loops. To make sure that it is the top Fe layer which exhibits perpendicular magnetization, I have repeated the experiment with Fe layers of different thickness, 2 ML and 3.5 ML for the bottom and the top layer, respectively.

MOKE hysteresis loops have been taken on such trilayer as a function of t_{Cu} (Fig. 4.8(b)). The remanent(\bullet) and saturation (\circ) Kerr intensity of polar MOKE loops reach a maximum for $t_{Cu} \sim 2.8$ ML and then decay with t_{Cu} . It is important to note that: (i) The value of the maximum signal corresponds roughly to the sum of the signals of 2 + 3.5 ML of Fe. (ii) Above $t_{Cu} \sim 14$ ML, the signal reaches a plateau which is now larger than the intensity of polar MOKE loop measured on the bottom Fe layer (\square) Fig. 4.8(b)). The observed value corresponds to a film thickness of 3.5 ML, i.e. t_2 , and demonstrates that, above t_{crit} , only the top Fe layer exhibits perpendicular magnetization.

4.2 Oxygen adsorption and spin reorientation

The governing role of the top Fe layer surface magnetic anisotropy for the trilayer magnetization is demonstrated in the following by gas adsorption experiments. The adsorption of small amounts of oxygen causes a modification of the electronic structure of the Fe-vacuum interface, and thus of the magnetic surface anisotropy. Changes of the easy axis of magnetization are observed by taking MOKE hysteresis loops before and after the adsorption either in polar or longitudinal geometry, while changes in the magnetic domain configuration are monitored by Kerr microscopy directly during the adsorption process. This technique has already proven to be very successful on single Fe layers on Cu(100) [77].

As it has been demonstrated in Sec.4.1.2, the trilayer has perpendicular magnetization (Fig.4.9(a)). The easy axis of magnetization of the whole trilayer reorients into the plane after the adsorption at 125 K of 1.8 L (1 *Langmuir* = 1×10^{-6} Torr · s) of O₂, as deduced from the polar (b) and longitudinal (c) MOKE hysteresis loops shown in

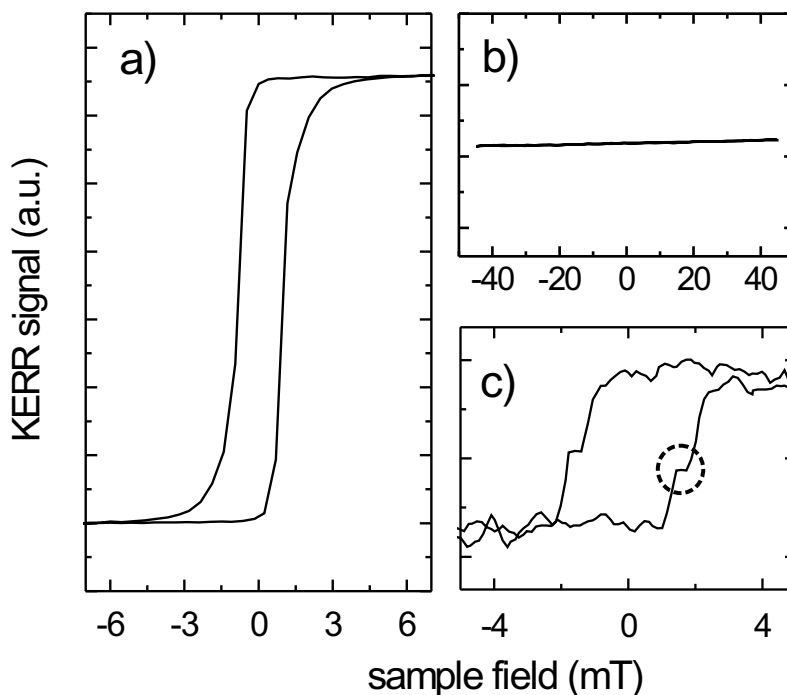


Figure 4.9: (a) Polar MOKE hysteresis loop of 2.4 ML Fe/2 ML Cu/3 ML Fe/Cu(100), taken before O₂ adsorption. Polar (b) and longitudinal (c) loops after O₂ adsorption. The two Fe layers exhibit in-plane magnetization and different coercive field.

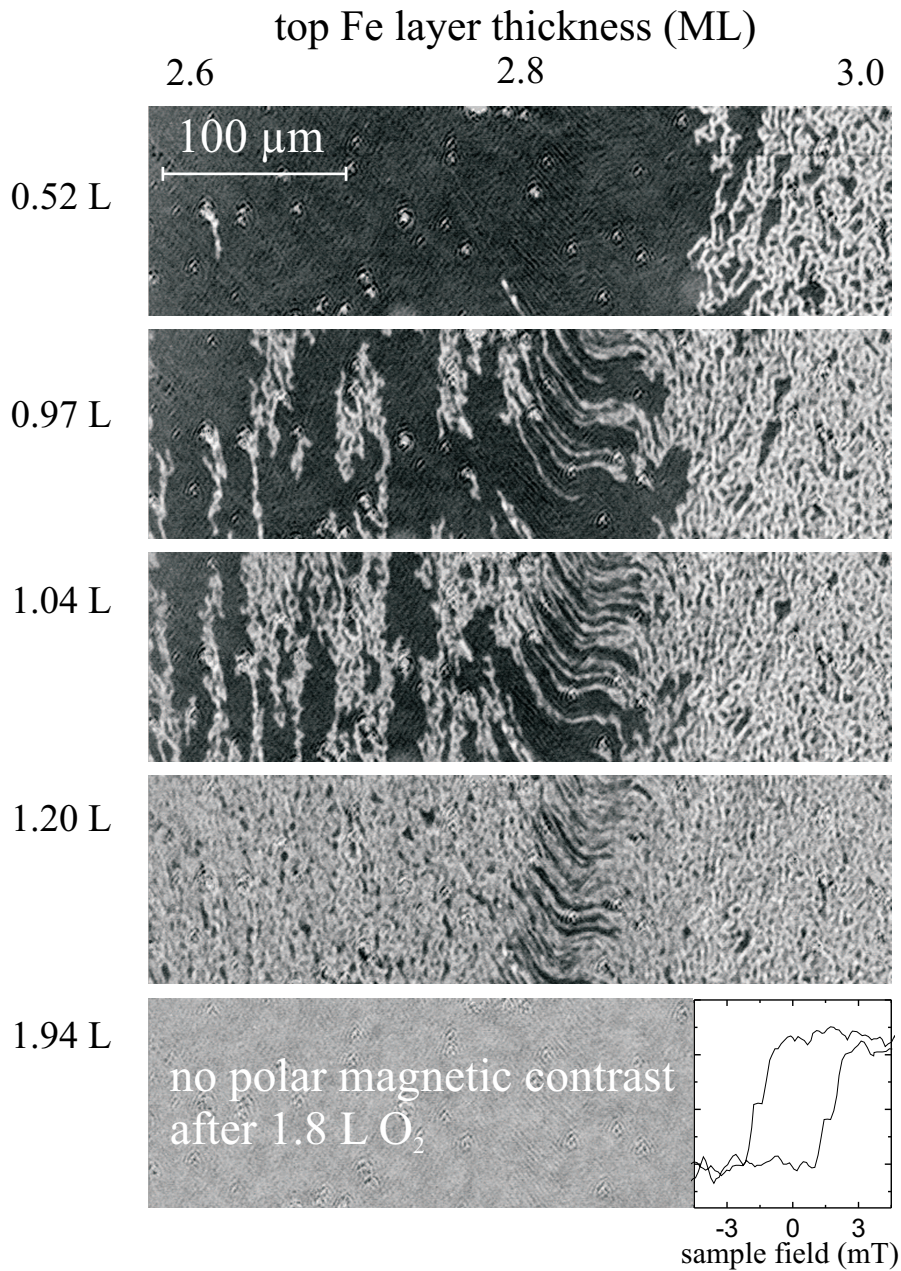


Figure 4.10: Kerr images of t_2 ML Fe/2 ML Cu/3 ML Fe captured during oxygen adsorption at 125 K. Inset: longitudinal MOKE loop of the trilayer taken after the adsorption of 1.94 L of O_2 . Image size: $400 \mu\text{m} \times 110 \mu\text{m}$.

Fig.4.9. In particular, the longitudinal loop evidences that both layers exhibit in-plane magnetization with slightly different coercive fields.

Oxygen-induced changes in the magnetization of t_2 ML Fe/2 ML Cu/3 ML Fe with increasing O_2 exposure are shown in the Kerr images in Fig. 4.10. Within these images, taken at zero field, the top layer thickness increases from ~ 2.6 ML to 3 ML. The transition from single to multi-domain state is visible at $t_2 = 2.9$ ML. Exposure of

the trilayer to oxygen initially causes a transition of the whole sample into a multi-domain state after $\sim 1.1 L$. The magnetic contrast disappears at $1.8 L$ of O_2 . The magnetization loop depicted in the inset of Fig. 4.10 was taken after O_2 adsorption by longitudinal MOKE.

In Fig. 4.5, the saturation signal (\square) of longitudinal MOKE loops after O_2 adsorption is shown as a function of t_2 . We find that, independent of t_2 , the magnetization of the whole trilayer has switched into the plane. The observed spin reorientation is attributed to an adsorbate-induced change of the magnetic interface anisotropy energy at the Fe-vacuum interface. Oxygen adsorption is reported to cause a charge transfer from iron to oxygen leaving behind Fe states with majority character and causing a decrease of spin polarization at the density of states at the Fermi energy [137, 138]. The strong response of the trilayer magnetism to modification of the electronic structure at the Fe-vacuum interface underlines the importance of this interface for perpendicular magnetization.

Discussion

As discussed in detail in Sec. 1.3, the magnetic coupling between FM layers separated by a non-magnetic layer is characterized by the interplay between interlayer exchange coupling (IEC) and magneto-static interaction. The IEC is often found to cause an alternation of FM and AF coupling between the two magnetic layers as a function of the spacer thickness. If this was the dominant coupling mechanism here, we would observed oscillations in the remanent Kerr intensity of the MOKE loops, with maxima and minima corresponding respectively to FM and AF configuration of the Fe layers. Such oscillations were not observed in our experiments. The results are rather in agreement with the picture of magneto-static interaction between the Fe layers. For $1.5 \leq t_{Cu} \leq 4$ ML, the stray field produced by the top Fe layer magnetization aligns out-of-plane the magnetization of the bottom layer, which exhibits in-plane magnetization after the deposition of the Cu interlayer. The presence of a stray field is evidenced by the formation of magnetic domains. By increasing t_{Cu} , the strength of the dipolar interaction gradually diminishes and for $t_{Cu} \geq 12$ ML, the bottom layer magnetization reorients into the plane along the easy axis. The coupling strength can be adjusted by the top Fe layer thickness. The higher the thickness, the larger its total magnetization and, as a consequence, the stray field. This observation further supports the idea of magneto-static interaction between the Fe layers. In case of negligible biquadratic coupling, the configuration with parallel magnetization in trilayers is always favored, independently of the prevalent mechanism of coupling. However, this is only true if the two FM layers have the same easy magnetization axis. Otherwise, a balance between magneto-static and anisotropy energy has to

be considered. For example, a non-collinear magnetic configuration induced by orthogonal uniaxial magnetic anisotropies in the individual magnetic layers *and* a proper choice of the spacer thickness was recently proposed by Taga *et al.* for Fe/V/Co trilayers [139]. In case of Co/Cu/Ni/Cu(001), a t_{crit} of 3.1 ML Cu for non-collinear magnetization state was measured [140]. In our experiment a 90° alignment of the magnetization directions has been found above a $t_{crit} \sim 12$ ML.

Previous experiments on Fe/Cu/Fe trilayers with the magnetic measurements performed ex-situ showed the indirect interaction through the Cu spacer as the dominant mechanism of coupling [68]. The absence of IEC in our samples is therefore not due to the particular choice of materials, but it has to be attributed to slight deviations in the film structure or morphology.

Bruno *et al.* showed theoretically that the presence of roughness at the film-spacer interfaces strongly reduces the strength of the indirect exchange coupling. In addition, higher correlated interface roughness also leads to a stronger superimposed contribution from magneto-static coupling, the so-called "orange-peel" coupling (Sec. 1.3).

The rapid decay of the oscillation amplitude observed in the RHEED measurements indicates that the layer-wise growth gets more and more out of phase. As a result, unfilled layers remain, contributing to a significant roughness. We thus believe that in our experiments, the interfacial roughness decreases considerably the strength of the interlayer exchange interaction so that the coupling between the Fe layers is governed by magneto-static interaction. The idea is supported by the absence of oscillatory coupling with Cu thickness, the magnetic domain formation in the film, and a morphological argument which will be discussed in the following.

The first experiments on the growth of Fe/Cu(100) by using Auger spectroscopy have been interpreted as a simple layer-by-layer growth mode [111]. This was later confirmed by STM studies [75] and it was also shown that the growth mode dominant up to 11-12 ML, when relaxed bcc-Fe domains start to nucleate [17]. This description is supported by numerous experiments. Recent studies have evidenced that the situation is more complex and the growth mode strongly depends on the substrate morphology. Dulot *et al.* have shown by STM that in case of Cu(100) substrate with high step density (step periodicity 10 – 15 nm), Cu segregation from the step edges was observed up to 4 ML of nominal Fe thickness, resulting in islands of heterogeneous composition. After the deposition of 0.5 ML of Fe, the formation of trenches, which expand through the Cu terraces, was observed, with more than two atomic layers exposed [141].

In collaboration with M. Lingenfelder (Kern's group, Max Planck Institute, Stuttgart), we have performed STM on the Cu(100) crystals which have been

used as substrates in our experiments. We have found a surface morphology with terraces of width between 10 nm and 60 nm (Fig. 4.11). We therefore believe that the growth mode is similar to that one observed by Dulot and coworkers.

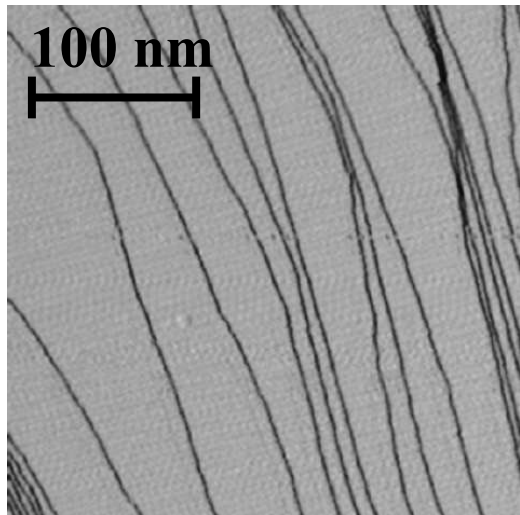


Figure 4.11: Scanning Tunnelling Microscopy (STM) image of Cu(100) crystal, taken after sputtering-annealing cycles. Image size: $312\text{ nm} \times 312\text{ nm}$. *In collaboration with M. Lingenfelder, Nanoscale Department, Max Planck Institute, Stuttgart*

As confirmed by RHEED, the roughness of the first Fe layer is maintained during the fabrication of the trilayer, resulting in rough interfaces between the Fe layers and the Cu spacer and, as a consequence, reduced IEC. Furthermore, the interface roughness might explain why the change of K_S upon Cu coverage was found to be much stronger here than reported previously [27] (Sec. 4.1). An increase of the film roughness results in a smaller contribution of K_S [126], making less favorable out-of-plane easy axis of magnetization. It becomes comparatively easier to induce a spin reorientation transition into the plane by further reducing K_S by depositing the Cu layer.

To further investigate the coupling, it is useful to change the magnetization direction of one layer and observe changes in the the second layer. Thus, a switching into the plane of the easy axis of the top Fe layer has been induced by oxygen adsorption (Sec. 4.2). As a consequence, a reorientation into the plane of the bottom Fe layer magnetization was also observed. The perpendicular magneto-static field produced by the top layer magnetization, which aligns out-of-plane the magnetization of the bottom layer, vanishes as soon as its magnetization reorients into the plane. The dependence of the bottom layer magnetization on the top layer magnetization is therefore evident. The experiments clearly prove the governing role of the top Fe layer for the magnetism of the whole trilayer and the sensitivity of the magnetic anisotropy to modifications of the Fe-vacuum interface by adsorbates.

used as substrates in our experiments. We have found a surface morphology with terraces of width between 10 nm and 60 nm (Fig. 4.11). We therefore believe that the growth mode is similar to that one observed by Dulot and coworkers. As confirmed by RHEED, the roughness of the first Fe layer is maintained during the fabrication of the trilayer, resulting in rough interfaces between the Fe layers and the Cu spacer and, as a consequence, reduced IEC. Furthermore, the interface roughness might explain why the change of K_S upon Cu coverage was found to be much stronger here than reported previously [27] (Sec. 4.1). An increase of the film roughness results in a smaller contribution of K_S [126], making less favorable out-of-plane easy axis of magnetization. It becomes comparatively easier to induce a spin reorientation transition into the plane by further reducing K_S by depositing the Cu layer.

To further investigate the coupling, it is useful to change the magnetization di-

Chapter 5

Structure and magnetism of ultrathin Fe films on Pt substrates

The correlation between structure and magnetism has been suggested and demonstrated on numerous film/substrate systems [2, 3, 12, 142–144]. However, only limited success could be achieved in correlating the magnetism to the sometimes minute details in structural properties, owing to the complex interplay between local atomic structure, electronic structure and magnetic anisotropy in atomically thin films.

To account for the particular electronic and structural properties of epitaxial films and their influence on the magnetism, phenomenological quantities, such as surface and step anisotropy, have been introduced and applied successfully during the past two decades of research [2, 145–147]. These quantities are chosen to reflect the symmetry of the observed magnetic anisotropy and hide the dependence on the local atomic arrangement. The immense effort in determining such anisotropy contributions experimentally has partly distracted from gaining a better understanding of the role of the local atomic structure itself.

In Chapter 3, it has been demonstrated the close relationship between morphology and domain wall pinning on Fe/Cu(001) by monitoring magnetic domain propagation directly during film annealing. In this chapter, I present another, particularly elegant way to reveal structurally driven changes of the magnetism. By controlling the growth mode of atomically thin Fe films on Pt surfaces via substrate steps, we govern the morphology and the local atomic structure. The comparison of Fe on the flat Pt(111) and on the vicinal Pt(997) surfaces strongly suggests a direct correlation between in-plane magnetic anisotropy and structural symmetry for Fe films thicker than 3 ML. In contrast, the perpendicular magnetization easy axis found below 3 ML Fe is independent of the film structure and tentatively ascribed to the film-substrate interaction.

5.1 Growth of Fe on flat and vicinal Pt surfaces

5.1.1 3-D Fe islands on Pt(111)

The growth of Fe on Pt is currently subject of extensive research [113, 114, 148, 149]. Within this work, the growth of Fe on flat Pt(111) has been investigated by LEED and, in collaboration with S. Rusponi and H. Brune (Institut de Physique de Nanostructures, École Polytechnique Fédéral de Lausanne, Switzerland), by STM, for comparison. In Fig. 5.1 STM images of different θ_{Fe} on Pt(111) are shown. On the flat Pt surface Vollmer-Weber growth mode with the formation of 3D islands already at the initial stage of the growth is observed. The 3D islands have irregular, ramified shape and grow laterally and in height with increasing coverage. A nominal θ_{Fe} of 1.7 ML is distributed into 4 simultaneously open layers (Fig. 5.1(d)). The corrugations visible in the second

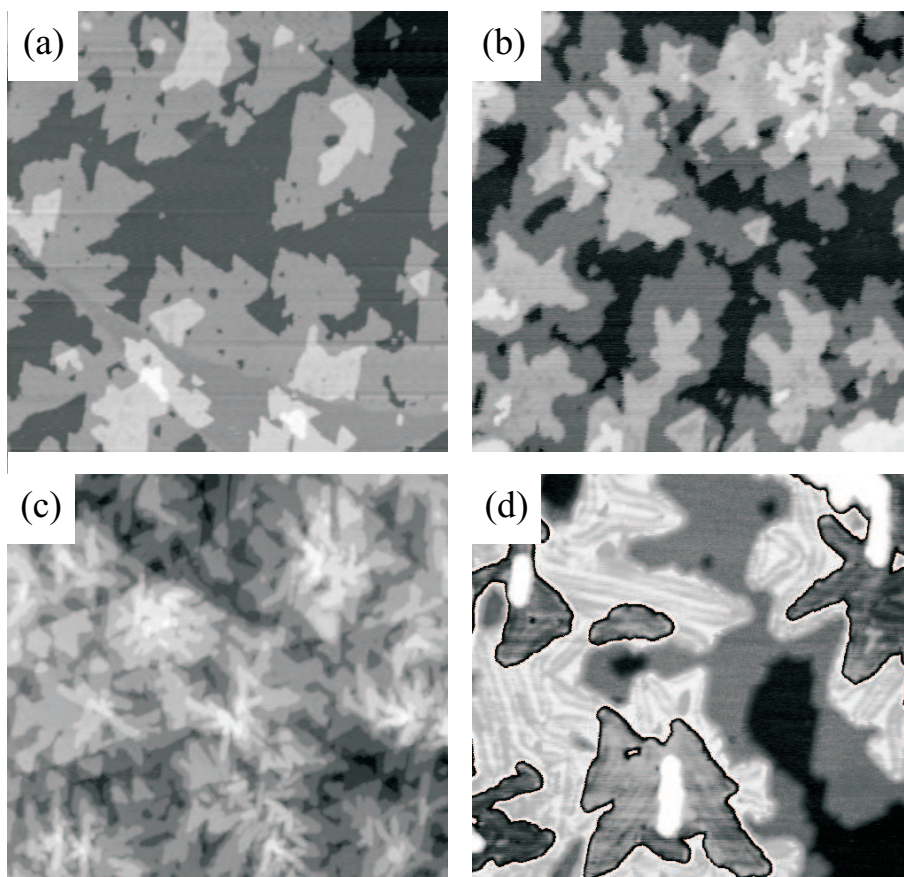


Figure 5.1: (a,b) STM on 0.7 ML Fe, 1.25 ML Fe, image size $150\text{ nm} \times 150\text{ nm}$. (c) 2.5 ML Fe on Pt(111), image size $150\text{ nm} \times 138\text{ nm}$ (d) 1.7 ML Fe/Pt(111), image size $60\text{ nm} \times 55\text{ nm}$. In (d) the contrast was adjusted to accentuate the corrugation in the second layer. *In collaboration with S. Rusponi and H. Brune, Institut de Physique de Nanostructures, École Polytechnique Fédéral de Lausanne, Switzerland*

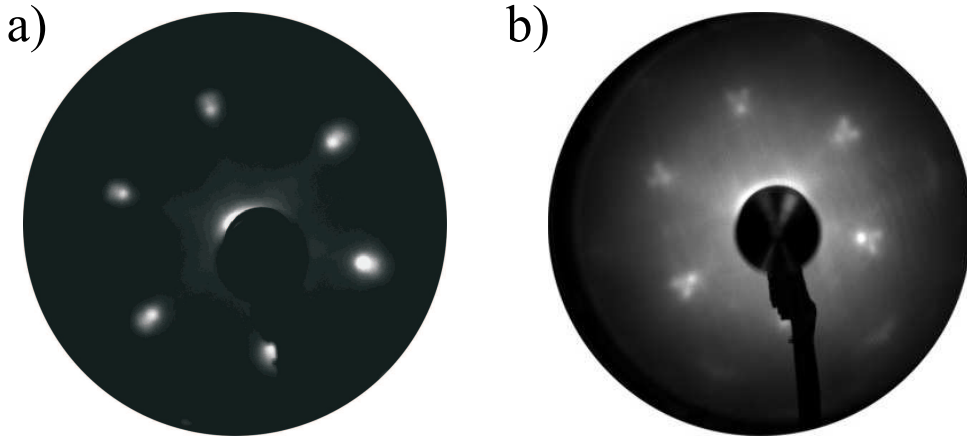


Figure 5.2: LEED images taken at 152 eV on Fe/Pt(111) grown at 300 K : (a) $\Theta_{Fe} = 0.8\text{ ML}$, (b) $\Theta_{Fe} = 3\text{ ML}$ after annealing at 500 K .

and third layer in the contrast-enhanced image in Fig. 5.1(d) are interpreted as a misfit dislocation network. Such dislocations are usually found to reduce the film strain due to the lattice mismatch to the substrate [150].¹ No signs of alloying are observed during growth near RT. Noticeable diffusion of Fe into the Pt sets in only above 600 K [114]. We remark that there is a weak tendency for Fe incorporation into the Pt top layer at very low dilution already around 140 K , which may be ascribed to the relaxation of the compressive stress in the clean Pt(111) surface [151].

Complementary LEED investigations reveal the atomistic film structure. Fig. 5.2(a) displays a LEED image taken on 0.8 ML Fe/Pt(111). The six diffraction spots of the fcc-(111) surface are slightly elongated in radial direction. The second-order diffraction spots, not visible at this energy, show an elongation in tangential direction. The symmetry of the diffraction spots hence excludes the presence of a pure fcc-Fe layer. A comparison with the STM images (Fig. 5.1) shows that at this coverage of 0.8 ML also the second and even the third layer contribute to the diffraction image. The observation of dislocation lines in the second layer in the STM images and the anisotropic spot broadening in the LEED pattern is thus interpreted as a structural transformation from fcc to bcc from the second Fe layer on.

By increasing θ_{Fe} , the LEED pattern visibly changes. For 3 ML Fe/Pt(111), around each first-order diffraction spot, six characteristic satellite spots can be observed (Fig. 5.2(b)). The intensity of the satellite spots depends strongly on the kinetic energy of the primary electrons due to the limited sensitivity of LEED to the structure along the surface normal. At no energy all satellite spots could be seen with identical inten-

¹The epitaxial strain can be calculated to 9.2% by assuming a lattice constant of fcc-Fe, $a_{Fe}^{fcc} = 3.59\text{ \AA}$ [120] and of Pt, $a_{Pt}^{fcc} = 3.92$.

sity. [152] To obtain this image, the sample was annealed at 500 K to improve the quality of the satellite spots which are already visible before annealing. The arrangement of these spots is consistent with the assumption of a bcc-Fe layer on Pt(111) [153], as will be explained in the discussion at the end of this chapter.

5.1.2 Growth of Fe on Pt(997)

The study of the growth of Fe on Pt substrates was focused in particular on the deposition of Fe on stepped Pt(997), since it allows to form linear nanostructures and even chains of single Fe atoms. The available data obtained by Thermal Energy Helium Atom Scattering (TEAS) can be summarized to the following picture: At deposition temperatures between 200 K and 400 K , Fe atoms preferentially decorate the Pt substrate steps at the initial growth stage. With increasing Fe coverage, θ_{Fe} , the step decoration is continued, resulting in step flow growth mode [114]. It is expected that for $\theta_{Fe} > 1$ ML, the film overgrows the substrate steps, leading to vertical mismatch and increasing disorder. The step periodicity is thus progressively lost.

LEED studies have been performed on Fe/Pt(997). LEED images obtained for different Θ_{Fe} are shown in Fig. 5.3(a-c). In Fig. 5.3(a) a characteristic diffraction image of 1 ML Fe/Pt(997) is shown. This image corresponds to the LEED image of the clean Pt(997) substrate without qualitative difference. The superstructure resulting from the substrate steps is fully maintained. This means that a pseudomorphic Fe layer has been formed. For nominal coverage $\theta_{Fe} > 1$ ML, the superstructure spots merge into broad spots with hexagonal symmetry (Fig. 5.3(b)). In addition, the background intensity increases. The observed hexagonal pattern indicates that Fe still grows with fcc-structure in the second and third layers in registry with the substrate. A characteristic change

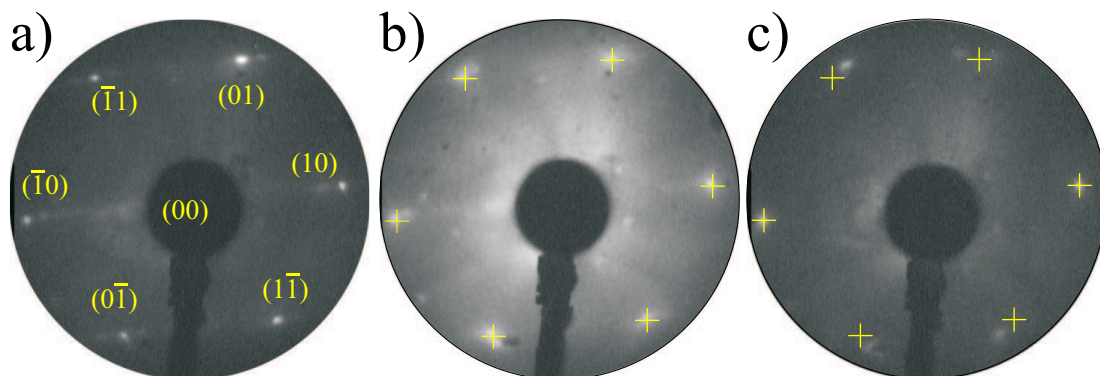


Figure 5.3: LEED images taken at 122 eV on Fe/Pt(997) grown at 300 K , (a) $\Theta_{Fe} = 1$ ML, (b) $\Theta_{Fe} = 2.2$ ML, (c) $\Theta_{Fe} = 6.6$ ML. Crosses (+) mark the position of the substrate fcc(111) diffraction spots.

of the diffraction image is observed at $\theta_{Fe} \simeq 3$ ML: four $((01), (1\bar{1}), (0\bar{1}), (\bar{1}1))$ of the six first-order diffraction spots shift with respect to the fcc-position, while the (10) and $(\bar{1}0)$ spots stay fixed at the same position (Fig. 5.3(c)). To visualize the change, the substrate first order spot positions are marked in the images (+). The observed LEED images will be interpreted as a fcc-bcc structural transition in the discussion later in this chapter.

5.2 Magnetic properties of Fe on Pt substrates

Magnetic investigations have been performed on films of constant coverage as well as wedge shaped films deposited at RT, with the nominal coverage varying from 0 up to 7 ML. For the MOKE measurements on Fe/Pt(111) the angle between the incident laser beam and the surface normal is $\sim 15^\circ$. For the experiments on Fe/Pt(997), an improved MOKE setup has been used, with the angle of incidence increased to 45° . This modification allows for a good sensitivity for both in-plane and out-of-plane magnetization.

5.2.1 Magnetism of Fe/Pt(111)

The evolution of the magnetization with θ_{Fe} at RT (a) and 135 K (b) is shown in Fig. 5.4. The values of remanence and saturation, as derived from MOKE hysteresis loops, are plotted. Clearly visible is a spin reorientation transition (SRT) from in-plane to out-of-plane when θ_{Fe} is reduced below a critical coverage of $\theta_{crit} \sim 2.8$ ML. Such a SRT is found for many thin-film/substrate systems and is commonly ascribed to the dominant role of the interface anisotropy. The magnitude of remanence and saturation as well as θ_{crit} depend on the measurement temperature. Below $\theta_{Fe} \sim 2.8$ ML, the magnetization lies preferentially perpendicular to the plane. However, no remanent signal (\bullet) is observed at RT. Above $\theta_{Fe} \geq 2.8$ ML, the magnetization is found within the film plane. The longitudinal remanent (\blacksquare) and saturation (\square) Kerr intensities increase with θ_{Fe} and remain constant on the plateau of the wedge. For sub-monolayer coverage below $\theta_{Fe} = 0.85$ ML no magnetic signal was detected, most likely because of the low Curie temperature, T_C , here. The coexistence of polar and longitudinal Kerr signals within a limited coverage range around θ_{crit} suggests a SRT via a canted magnetization state. The polar Kerr signal below θ_{crit} depends strongly on the temperature. By lowering the temperature below 150 K, a remanent MOKE signal could be measured (\bullet) Fig. 5.4(b)).

Fig. 5.5 shows polar magnetization loops of 1.4 ML Fe/Pt(111) taken at 200 K (a) and 110 K (b), respectively. A characteristic in-plane magnetization loop of 4.5 ML Fe/Pt(111) taken by longitudinal MOKE at 110 K is shown in Fig. 5.5(c).

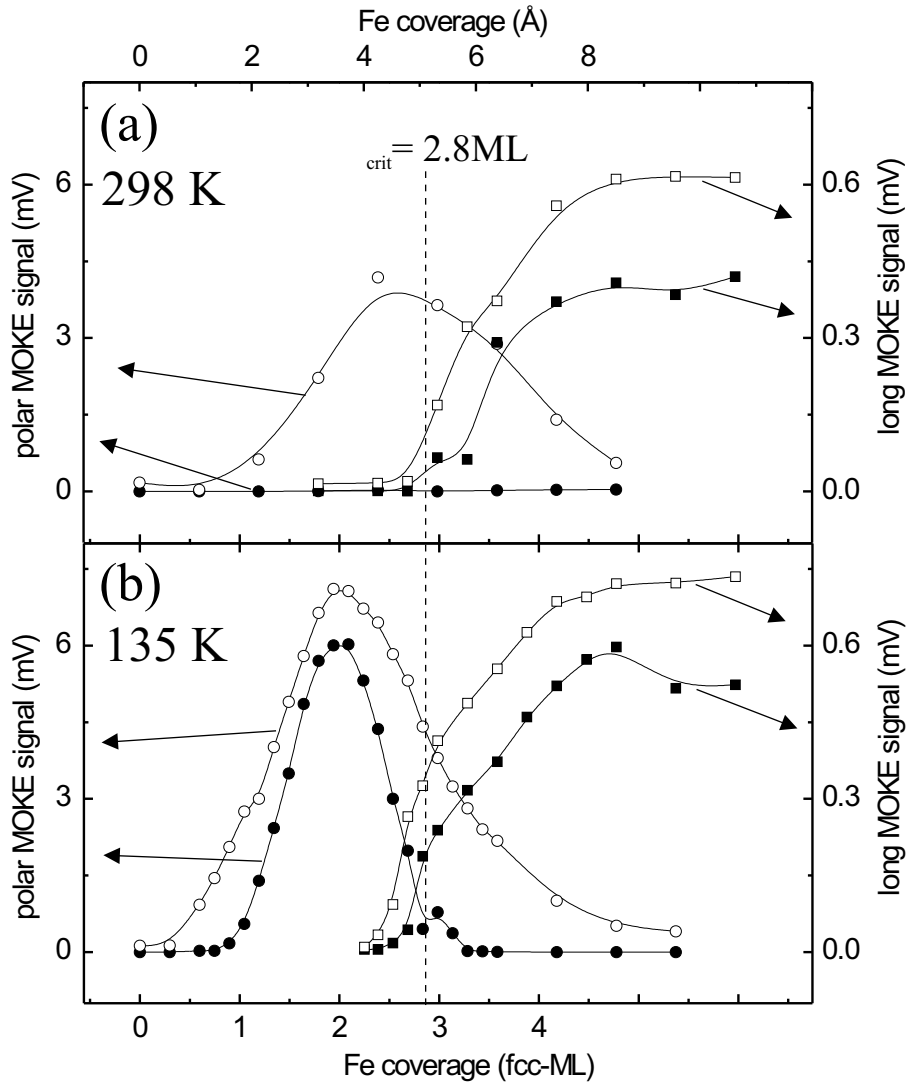


Figure 5.4: Polar remanent (\bullet), polar saturation (\circ), longitudinal remanent (\blacksquare) and longitudinal saturation (\square) Kerr intensities of MOKE hysteresis loops taken at RT (a) and 135 K (b) of an Fe-wedge/Pt(111) of $\theta_{Fe} = 0 - 4.8$ ML as a function of θ_{Fe} . Polar remanent (\blacktriangle) Kerr signal measured at 135 K.

The observations are summarized as follows: (i) Fe films grown on Pt(111) at RT undergo a SRT from perpendicular to in-plane at $\theta_{crit} \simeq 2.8$ ML. (ii) Remanent magnetization is observed at RT only above θ_{crit} . Remanent perpendicular magnetization below θ_{crit} has been observed only at $T \leq 150$ K. (iii) Above θ_{crit} , there are no signs of a magnetic anisotropy within the film plane. The MOKE loops measured with the field applied along the $[\bar{1}10]$ and $[11\bar{2}]$ directions are both square shaped and appear to be identical.

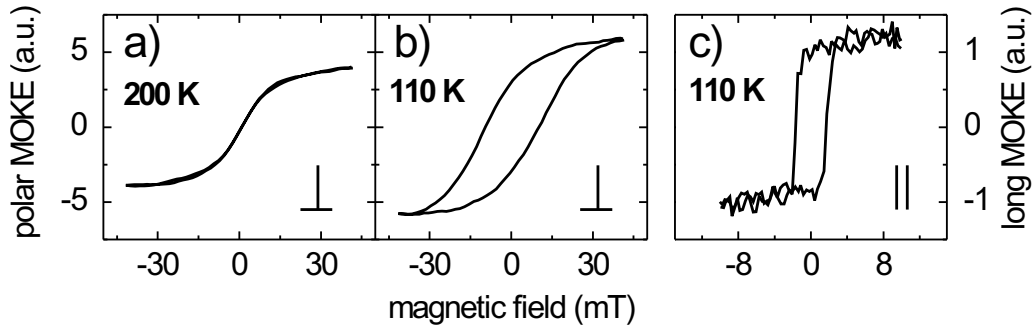


Figure 5.5: Polar (a,b) and longitudinal (c) MOKE hysteresis loops of (a) 1.4 ML Fe/Pt(111) at 200 K, (b) 1.4 ML Fe/Pt(111) at 110 K, (c) 4.5 ML Fe/Pt(111) at 110 K.

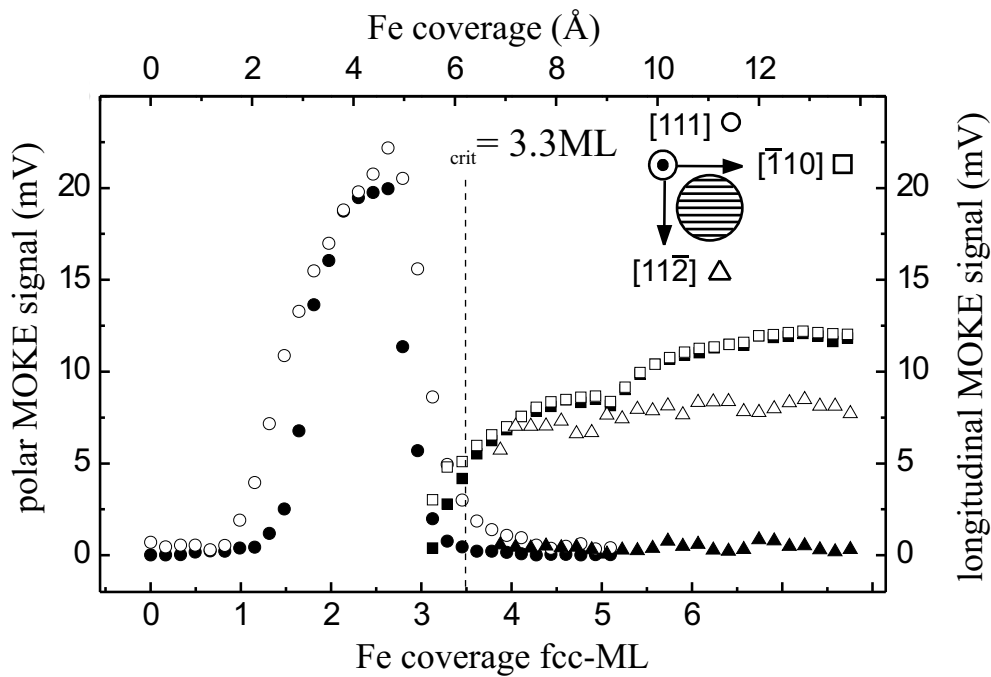


Figure 5.6: Kerr intensities of MOKE hysteresis loops taken at RT of an Fe-wedge/Pt(997) as a function of θ_{Fe} : polar remanent (\bullet), polar saturation (\circ), longitudinal remanent along $[\bar{1}10]$ (\blacksquare), longitudinal saturation along $[\bar{1}10]$ (\square), longitudinal remanent along $[11\bar{2}]$ (\blacktriangle), longitudinal saturation along $[11\bar{2}]$ (\triangle).

5.2.2 Magnetism of Fe/Pt(997)

For comparison, I have studied the magnetic properties of Fe films grown on Pt(997) substrates. Also here, several Fe-wedges with θ_{Fe} varying from 0 up to 6.7 ML have

been grown at RT. The polar remanent (\bullet) and saturation (\circ) Kerr signals are shown in Fig. 5.6. As for Fe/Pt(111), also on the Pt(997) substrates a SRT from in-plane to perpendicular magnetization was observed. The $\theta_{crit} \sim 3.3$ ML is $\sim 15\%$ larger than for Fe/Pt(111). No magnetic signal was measured below $\theta_{Fe} \sim 1$ ML. In this thickness range, T_C is below 200 K as can be shown by measurements on the cooled sample. For $\theta_{Fe} > 3.3$ ML, the magnetization lies within the sample surface. The in-plane magnetic anisotropy has been investigated by applying the field within the film plane parallel and perpendicular to the step edges on separate films, after rotating the substrate by 90° . Along the step edges the saturation (\square) and the remanent (\blacksquare) MOKE signals have the same values. In contrast, no remanence (\blacktriangle) was observed perpendicular to the step edges. The signal (\triangle) corresponds to the Kerr signal at maximum available field and does not represent the saturation signal. Along this direction the film magnetization could not be saturated (see hysteresis loop in Fig. 5.7(c)).

MOKE magnetization loops taken on Fe/Pt(997) at $\theta_{Fe} = 2.5$ ML and $\theta_{Fe} = 6.5$ ML are shown in Fig. 5.7. The polar loop (Fig. 5.7(a)) is clearly square shaped at RT, in contrast to the loops obtained for the same θ_{Fe} on Pt(111). The in-plane loops taken on the thicker film along and perpendicular to the substrate steps (Fig. 5.7(b,c)) reflect a pronounced in-plane anisotropy with the easy axis along the step edges.

Complementary X-ray magnetic circular dichroism (XMCD) measurements have been performed recently on both systems. The experiments confirm the magnetic properties found by the MOKE study. In addition they reveal in-plane spin orientation for

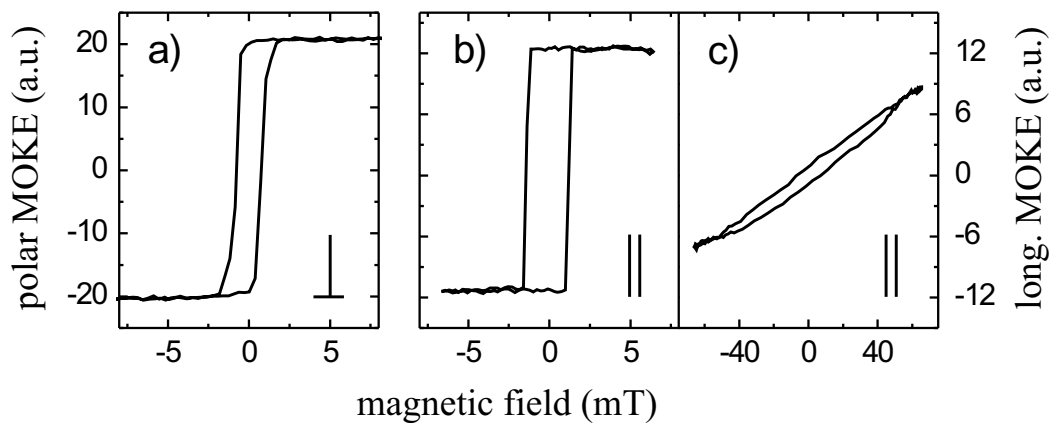


Figure 5.7: polar (a) and longitudinal (b,c) MOKE hysteresis loops, measured at RT, of: (a) 2.5 ML Fe/Pt(997), (b) 6.5 ML Fe/Pt(997) along the $[\bar{1}10]$ direction, parallel to the substrate steps, (c) 6.5 ML Fe/Pt(997) along the $[11\bar{2}]$ direction, perpendicular to the substrate steps.

0.13 ML Fe, identical magnetic moment per atom for the out-of-plane and in-plane phase and induced spin moment for Pt. [154]

5.2.3 Adsorbate induced shift of the Curie Temperature

Oxygen adsorption experiments have been performed on 2 ML Fe/Pt(997) to probe the sensitivity to electronic modification of the Fe-vacuum interface. The oxygen has been introduced into the UHV chamber through a leak valve to achieve an oxygen partial pressure of 8.5×10^{-9} mbar. Polar MOKE loops were recorded as a function of exposure to oxygen (Fig. 5.8(a)). The square shaped magnetization loop of the as-grown film (I) changes to S-shaped loop with no remanence, but almost unmodified saturation (II).

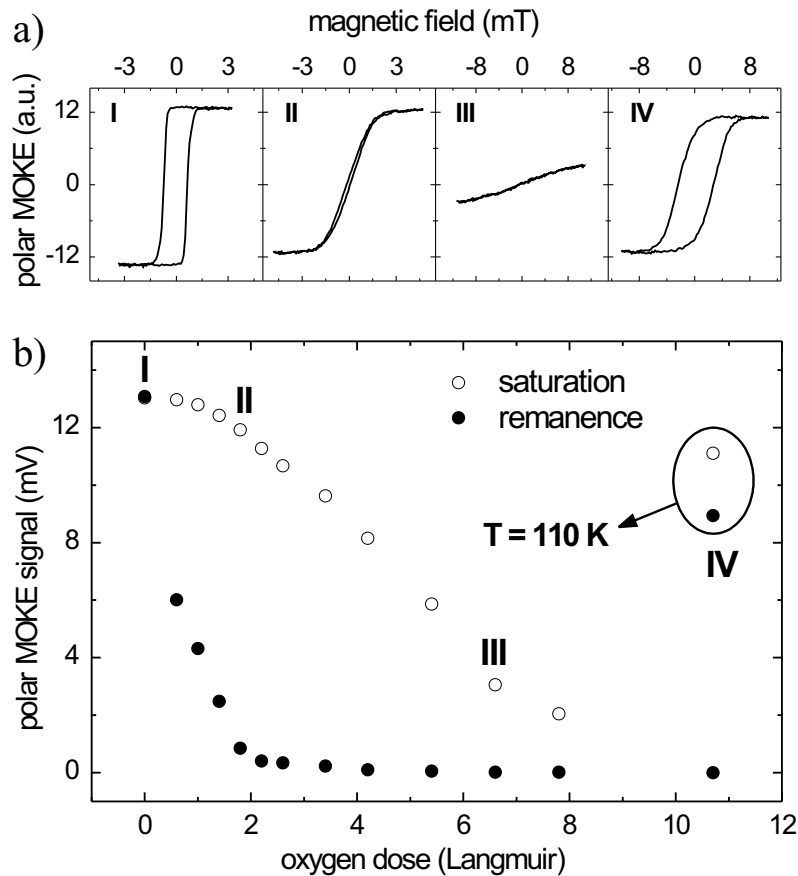


Figure 5.8: (a) Polar MOKE hysteresis loops of 2 ML Fe/Pt(997) taken at RT (I) (II) (III) and 110 K (IV): (I) after the growth, (II) after the adsorption at RT of 1.8 L, (III) of 6.6 L, (IV) of 10.7 L of O₂. (b) Remanent (●) and saturation (○) Kerr intensity of polar MOKE hysteresis loops taken during oxygen adsorption at RT as a function of the oxygen dose put into the chamber.

The saturation disappears for dosages higher than 8 L of O_2 ($1 L = 1 \times 10^{-6} Torr \cdot s$) (III), but can be recovered by cooling the sample to 110 K (IV).

In Fig. 5.8(b), the evolution of the remanent (\bullet) and saturation (\circ) Kerr signals with oxygen exposure, as obtained from polar MOKE hysteresis loops, is shown. For small amounts of O_2 , less than 1.5 L , a drop of the remanence is observed while the saturation remains constant. A further adsorption of oxygen causes a decreasing also of the saturation signal. Above 10 L , neither polar nor longitudinal MOKE signals have been detected at RT. By lowering the temperature to 110 K , the polar remanent and saturation MOKE signals could again be recovered. We thus conclude a lowering of T_C caused by oxygen adsorption.

Changes in the magnetization can be monitored directly during the adsorption process by in-situ Kerr microscopy. The Kerr images in Fig. 5.9 are taken in remanence during oxygen adsorption at RT on 1.6 ML Fe/Pt(997). The sample has been magnetized by an external field to obtain a magnetic single domain state. Exposure to more than 0.35 L

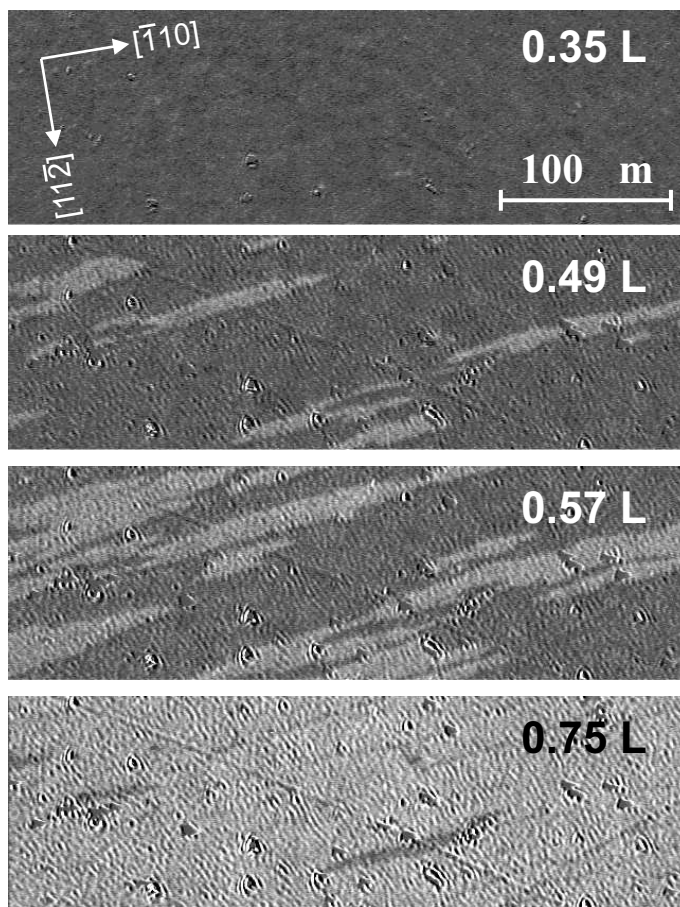


Figure 5.9: Kerr microscope images of 1.6 ML Fe/Pt(997) acquired in remanence during oxygen adsorption at RT as a function of the oxygen dosage. Image size: $400 \mu m \times 125 \mu m$.

of O₂ causes the appearance of bright stripes which propagate mainly along the $[\bar{1}10]$ direction with increasing O₂ exposure. The stripe width of $\sim 20 \mu\text{m}$ is much larger than the step periodicity ($\sim 20 \text{ \AA}$). After the adsorption of $0.75 L$, all magnetic contrast has disappeared. The intermediate grey color of the Kerr image is interpreted as a state with no preferential direction for the magnetization, corresponding to the paramagnetic state above T_C .

Discussion

The structural and magnetic characterization of ultrathin Fe films on Pt substrates with and without substrate steps reveal structural as well as magnetic transitions as a function of θ_{Fe} . Fe films on Pt(111) as well as on Pt(997) show a spin reorientation transition (SRT) from perpendicular to in-plane at a similar critical coverage, θ_{crit} , of 2.8 ML and 3.3 ML, respectively. Fe starts to grow on both substrates pseudomorphically. The resulting tremendous elastic energy triggers structural transition towards bcc(110) already in the second atomic layer of the islands of Fe/Pt(111). The onset of this transition is delayed in the presence of substrate steps and found at ~ 3.2 ML for Fe/Pt(997).

Because of the coincidence of the SRT with the fcc-bcc transition in Fe/Pt(997) it appears obvious to ascribe the perpendicular anisotropy to the fcc-phase of Fe. However, the robustness of the perpendicular anisotropy, in particular θ_{crit} , to distinct variations of structure and morphology as in Fe/Pt(111) opposes such a simple correlation. Rather than the film structure, the electronic interaction at the film-substrate interface seems to dictate the magnetic anisotropy. Circular dichroism experiments on FePt surface alloys reveal the importance of hybridization between the Fe 3d and Pt 5d band: the Fe anisotropy is governed by the large spin-orbit coupling of Pt and an induced magnetic moment is found for Pt [155]. It is reasonable to assume similar hybridization for the epitaxial films investigated here. The perpendicular anisotropy can hence be explained independent of the film structure and is ascribed to the Fe-Pt interface anisotropy. The slight dissimilarity between θ_{crit} of the Fe islands on Pt(111) and the Frank-van-der-Merwe layer on Pt(997) is thus attributed to the differences of the Fe-Pt contact area. In this picture it is merely the stability of the perpendicular magnetization which is directly influenced by the film morphology. The total perpendicular magnetization of the Fe on Pt(111) is destabilized by the separation of the film into islands, manifested in S-shaped magnetization loops and the absence of remanence at $300 K$.

The film-vacuum interface, often cited as the origin of perpendicular magnetization in the thin film limit, does not seem to play a significant role here. The adsorption of oxygen

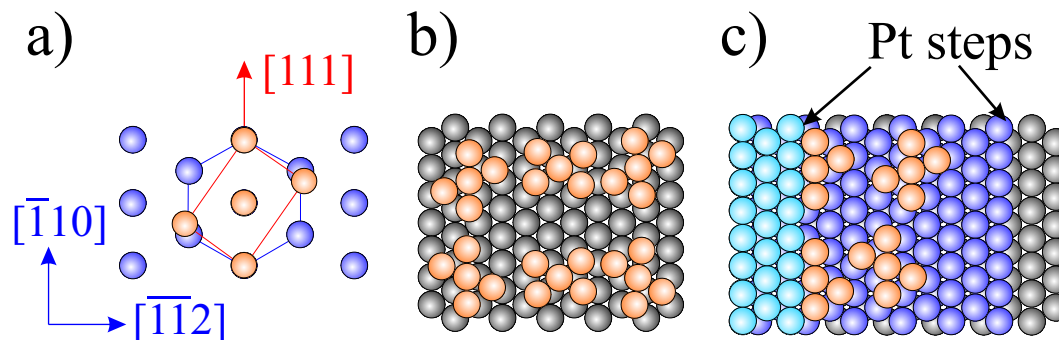


Figure 5.10: (a) bcc-Fe domains with Kurdjumov-Sachs orientation. Blue and orange spheres represent Pt and Fe atoms, respectively. The $[111]$ direction of the bcc-domains in the adlayer coincides with the $[\bar{1}10]$ fcc direction of the substrate. For simplicity, the Fe atoms are placed in on-top sites. (b) Atomistic picture of the bcc-Fe domains with Kurdjumov-Sachs orientation on the Pt(111) substrate. (c) In the presence of substrate steps only 2 bcc KS domains, schematically placed on the substrate terrace, remain.

does not cause a SRT, underlining the insensitivity of the anisotropy to perturbations of the electronic structure at the surface, as discussed later.

The structural transition towards bcc occurs by formation of bcc(110) domains in the so-called Kurdjumov-Sachs orientation to the underlying fcc(111) layer. In this orientation, the bcc $[111]$ direction is coincident with the fcc $[\bar{1}10]$ direction, bringing 2 atoms of the sketched bcc(110) cell out of registry as is shown in Fig. 5.10(a). On the fcc(111) surface six structural domains can be formed (Fig. 5.10(b)), resulting in satellite diffraction spots in the LEED image in Fig. 5.2(b). From these satellite spots only one remains visible at the $(01), (1\bar{1}), (0\bar{1})$ and $(\bar{1}\bar{1})$ first order diffraction spots for Fe coverage larger than 3 ML on Pt(997) (Fig. 5.3(c)). No satellite spots appear at the (10) and $(\bar{1}0)$ spots. The LEED image is consistent with the hard sphere model given in Fig. 5.10(c). The formation of four out of six possible bcc-domains is suppressed, and only those domains with the bcc $[111]$ direction aligned along the substrate steps are present. Such a film structure may be the result of almost free strain relaxation perpendicular to the step direction allowing for an incommensurate structure in this direction. This also implies anisotropic film stress within the plane.

This structural asymmetry is directly reflected in the magnetic anisotropy of the Fe films. Reducing the symmetry of the bcc-Fe film by introducing substrate steps of the Pt(997) surface coincides with a pronounced in-plane anisotropy of the magnetization with the easy axis along the step direction and the hard axis perpendicular to it (Fig. 5.7(b,c)). We thus propose a direct correlation between the particular atomic structure of the film and the magnetic anisotropy for Fe coverage larger than 3 ML.

This conclusion means that the magnetic anisotropy of Fe/Pt(997) is determined by structural asymmetry, besides the Neel-type contribution due to the modified coordination at the substrate steps [39], discussed as the dominant contribution in other systems [156–158]. However, the influence of the structural asymmetry on the anisotropy appears to be a particular property of the Fe/Pt system. Experiments on Fe grown on vicinal Cu(111) also reveal in-plane anisotropy but with all possible six Kurdjumov-Sachs domains present [159]. The authors could prove the directional dependence of the orbital moment within the plane due to broken bonds at the steps, resulting in in-plane magneto-crystalline anisotropy.

Interesting insight in the interplay between electronic structure and magnetism can be gained from the observed adsorbate-induced modification of the Curie temperature of Fe/Pt. Unlike in earlier experiments, for instance on Fe/Cu [77], Fe/Cu/Fe [132], or Ni/Cu [160], no SRT was observed upon adsorption. Here the easy axis remains out-of-plane, independently of the amount of adsorbed oxygen.

A reduction of the Curie temperature, T_C , due to small quantities of metal and gas adsorbates was already found in the past for Cu on Co/Cu(100) and O_2 on Ni/Cu(100) [136, 161]. Weber *et al.* measured an enhancement of T_C by adsorbing 0.1 L of O_2 on pseudomorphic ultrathin Fe films on W(110), whereas the adsorption of 1.0 L results in a small decreasing of T_C [162]. Oscillations of T_C as a function of the capping layer thickness were instead observed in case of Cu on Fe/Cu(100) [27]. The oscillations have been attributed to the oscillatory RKKY character of exchange interactions in itinerant ferromagnets [129]. The coupling between the magnetic atoms is not only mediated through the magnetic layer itself but also via the capping layer *and* the substrate. But in case of non-metallic adsorbate, very unlikely an oscillatory behavior of T_C may be found. Wang *et al.* suggested that a decreasing of T_C might be ascribed either to a smaller effective thickness of the magnetic film or to a reduced magnetic moment of the Fe atoms due to charge transfer and hybridization between the 2p states of O_2 and the 3d states of Fe [163]. In our case, the magnetic saturation signal after gas adsorption is only little affected, proving that the magnetic moment per Fe atom is unchanged and the formation of Fe oxide is minimal.

In general, changes of T_C are ascribed to modifications of the magnetic anisotropy or the exchange interaction. Bruno has discussed the thermodynamics of two dimensional systems taking in account, besides the exchange interaction, both the magnetic crystalline anisotropy *and* the dipolar interactions (shape anisotropy) [164]. In addition to the strong dependence of T_C on the exchange interaction, a weaker logarithmic dependence on the magnetic anisotropy for systems with perpendicular easy axis of mag-

netization was calculated. As a consequence, a reduction of the magnetic anisotropy determines a lowering of T_C . However, based on the insensitivity of the easy axis direction to the oxygen adsorption, a significant anisotropy change is excluded.

It is thus reasonable to conclude that rather the exchange interaction in Fe/Pt systems is reduced by the gas adsorption, resulting in the observed decrease of T_C . The exchange interaction is directly related to the electronic structure near the Fermi energy, E_F [165], and thus susceptible to electronic interaction with adsorbates. Although the electronic structure was not directly studied in this work, earlier experiments revealed strong electronic interaction between Fe and O_2 with major consequences for the magnetism [137]. The density of states and the spin polarization of Fe near E_F were found to decrease gradually with oxygen coverage. A charge transfer from iron to oxygen was furthermore suggested, resulting in spin-polarized states also in the oxygen. Similar effects were observed also for Fe films on different substrates [137, 138].

Chapter 6

Magnetism of Fe clusters on Pt surfaces

The study of small clusters has shown that fundamental properties, such as magnetic moments and anisotropy, electronic structure or chemical reactivity, are different from bulk behavior and dependent on the cluster size [166, 167]. While in free clusters such phenomena are commonly ascribed to the modified atomic coordination, clusters in contact with surfaces are in addition affected by the underlying substrate [168, 169]. Thus, the deposition of clusters offers the opportunity to exert influence on the cluster properties, for instance by exploiting electronic interactions or strain effects.

Several approaches have been developed to achieve controlled deposition of size-selected nanoclusters onto a substrate. On one hand, clusters can be formed in the gas phase and deposited on the substrate by soft-landing on a noble gas buffer layer [170]. On the other hand, compact clusters can be fabricated by Molecular Beam Epitaxy (MBE) directly on the substrate if the surface has been pre-covered with a noble gas buffer layer to enhance the adlayer mobility [171, 172]. But also without such a buffer layer the heteroepitaxial growth of some materials results in the formation of separated 3D islands, offering a third method to fabricate supported nanoclusters [173, 174].

A challenging aim is to explore specifics in the cluster properties resulting from the preparation method. The scope of the work presented in this chapter is to analyze and compare the structural and magnetic properties of Fe clusters on Pt prepared by noble gas assisted growth on one hand, and by heteroepitaxy on the other hand. It will be shown that the structure and the magnetic anisotropy of the clusters are strongly influenced by strain effects imposed by lattice mismatch between cluster material and support.

6.1 Buffer layer assisted growth of Fe clusters

Clusters of Fe of a few nanometer in diameter have been fabricated on Pt(997) by noble gas assisted assembly, as described in [171, 172, 175]. The atomic substrate steps of Pt(997) surface separating terraces of (111) orientation are not expected to influence the cluster formation at low preparation temperatures. Films of 2 atomic layers (ML) and 4 ML Fe have been deposited by Molecular Beam Epitaxy (MBE) onto the substrate which was pre-covered by a Xenon layer at 35 K [113]. Already at this low temperature the mobility of the metal atoms on Xe is sufficiently high to form small clusters [172]. The formation of cluster is possible due to the very weak adatom-buffer interactions. However, as we will see in the next section, to modify the magnetic anisotropy with respect to epitaxial Fe films grown directly on Pt, a Xe layer of at least 2 ML thickness is required. Warming up the substrate to 70 K causes evaporation of the Xe layer. The clusters coalesce during Xe sublimation and thus grow in size, until making contact with the Pt surface where wetting is frustrated by kinetics. The final cluster size and the size distribution are independent of the substrate and depend mainly on the initial thickness of the Xe layer and, to some extent, also on the Fe coverage.

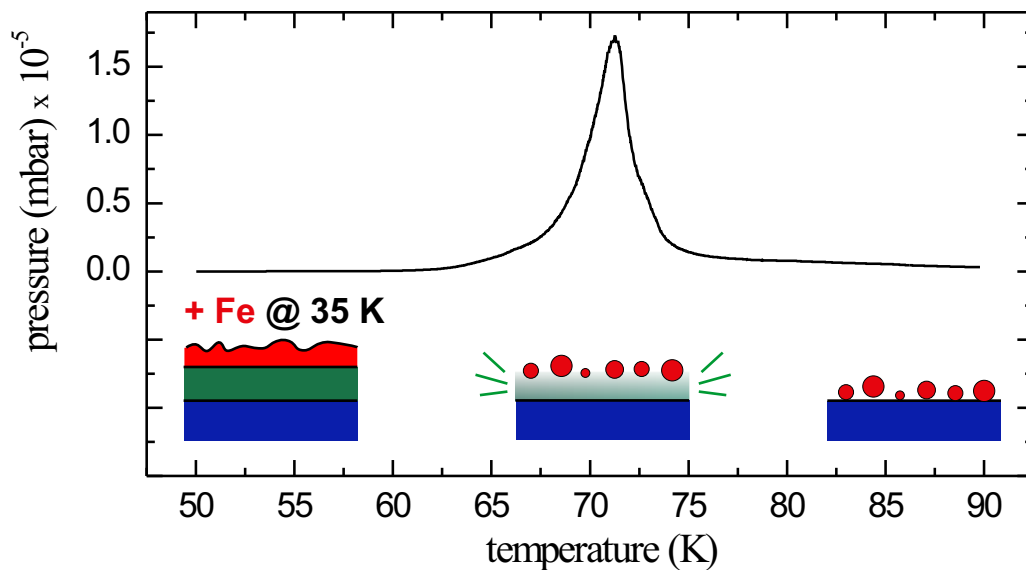


Figure 6.1: Xenon partial pressure in the UHV chamber as a function of substrate temperature recorded during the sample warming up. The sketches illustrate the cluster formation during Xe desorption.

The thickness of the Xe buffer layer is controlled by adjusting the Xe partial pressure and the exposure time. Assuming a sticking coefficient of 1 at 35 K, a gas flow of 5.5 Langmuir ($1 L = 10^{-6} \text{ Torr} \times 1 s$) leads to the formation of 1 ML Xe ($1 ML = 10^{15} \text{ atoms/cm}^2$).

The advantages of this preparation method are that (i) clusters of almost any material can be prepared without limitations usually associated with epitaxy, such as wetting phenomena, surface mobility, and other perturbations by the substrate [176], and (ii) the cluster fabrication does not require experimental equipment beyond the standard tools commonly used for MBE growth.

Auger Electron Spectroscopy (AES) yields integral information about the result of each individual preparation step. The low energy Auger lines of Pt ($64 eV$) and Fe ($47 eV$) are most sensitive to morphological differences of nanostructures. A characteristic AES spectrum of the clean Pt substrate is shown in Fig. 6.2(a). After depositing 100 L ($\sim 18 \text{ ML}$) of Xe at 35 K substrate temperature, only the MNN Auger line of

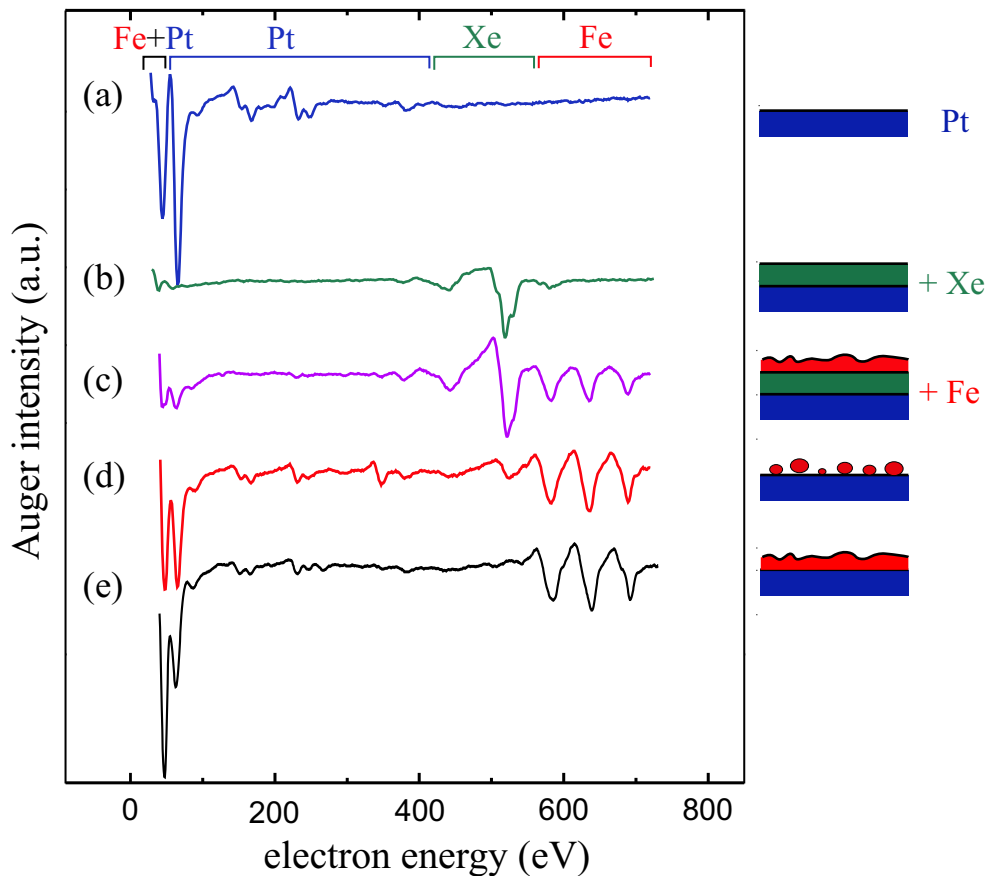


Figure 6.2: Auger spectra taken during different stages of the cluster preparation. (a) clean Pt, (b) 100 L Xe/Pt, (c) 2 ML Fe/100 L Xe/Pt, (d) clusters of Fe after the evaporation of Xe. (e) Auger spectrum taken on 2 ML Fe film on Pt grown at 40 K.

Xe at 544 eV is visible (Fig. 6.2(b)). Fig. 6.2(c) shows an AES spectrum taken after the deposition at 35 K of 2 ML of Fe on the Xe buffer layer. The Xe layer is desorbed by gradually warming up the sample to 110 K with a rate of $\sim 3\text{ K/min}$. The Xe partial pressure in the UHV chamber reaches its maximum at $\sim 71\text{ K}$ substrate temperature, as shown in Fig. 6.1. During the Xe desorption, the Fe atoms become very mobile and the formation of clusters occurs. The AES spectra in Fig. 6.2(d) is observed on Fe clusters after Xe desorption.

As comparison, in Fig. 6.2(e), an AES spectrum taken on epitaxial 2 ML Fe/Pt(997) grown at 41 K is shown. It is clearly visible that (i) the intensity of the Pt peak at 64 eV , as well as the MNN lines at 168 eV and 237 eV are larger in (d), and (ii) The ratio between the Fe_{47} and Pt_{64} peak intensities is larger for the Fe films in (e). These findings are consistent with the picture that small Fe clusters, covering only a fraction of the Pt surface, are formed on the Xe layer, while 2 ML Fe films, covering almost (Pt(111)) or totally (Pt(997)) the full Pt surface area, are formed without Xe.

6.2 Magnetic properties of clusters and films of Fe on Pt

6.2.1 Fe clusters

Magnetization loops of the Fe structures have been recorded in-situ by MOKE measurements in polar and longitudinal geometry [177]. The MOKE measurements were done in a temperature range between 40 K and 300 K , after the desorption of the Xenon at $80\text{-}100\text{ K}$. Longitudinal MOKE loops of clusters formed of 2 ML Fe (a) and 4 ML Fe (b) on 100 L Xe are shown in Fig. 6.3. For clusters of 2 ML Fe, S-shaped magnetization loops with no remanence are found at 43 K . The clusters are not magnetically saturated at the maximum available in-plane field of 70 mT . Increasing the amount of Fe significantly changes the shape of the loops. Aligning the magnetic moments of the clusters of 4 ML Fe by the in-plane field results clearly in remanent magnetization. For both samples no magnetic signal could be detected in polar geometry. Based on this observation, a preferred magnetization axis along the substrate surface is concluded for Fe clusters on Pt substrates.

The magnetic anisotropy of the clusters is thus clearly different from the anisotropy of 2 ML Fe films grown at 40 K without the Xe buffer layer. At such low growth temperatures, the mobility of the Fe atoms is suppressed and a highly disordered and defect-rich adlayer is formed. Despite this significant roughness, clear perpendicular

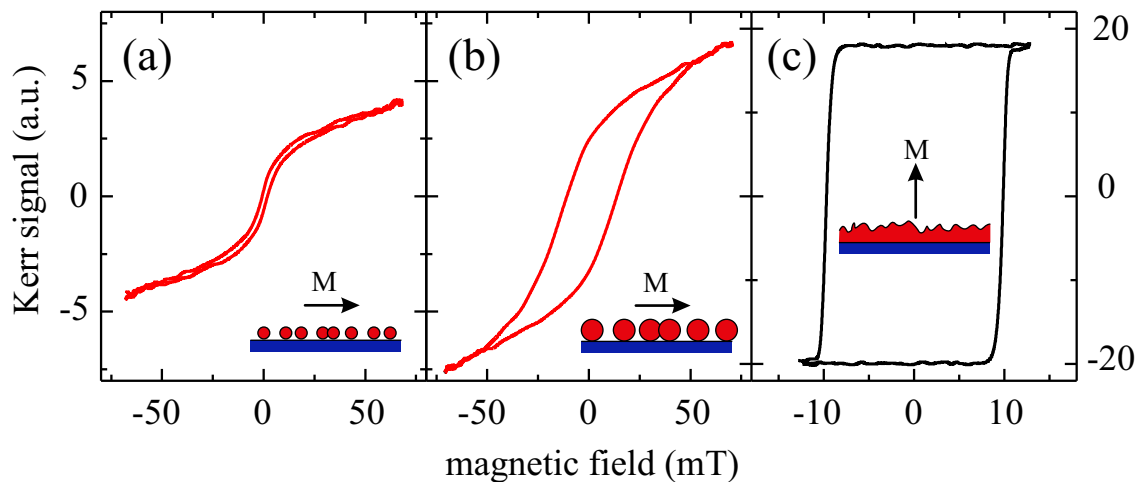


Figure 6.3: Magnetization loops measured at ~ 40 K by (a) longitudinal MOKE on Fe clusters of 2 ML Fe/100 L Xe/Pt, (b) longitudinal MOKE on clusters of 4 ML Fe/100 L Xe/Pt, (c) polar MOKE on 2 ML Fe/Pt grown at 41 K. To decrease the coercivity, this loop was taken at 126 K.

magnetization is found by polar MOKE, as shown in Fig. 6.3(c). The easy magnetization axis is thus identical to the one found for room temperature grown Fe films, as described in the previous chapter.

The investigation of the temperature dependence of the MOKE loops reveals further information about the magnetization of the cluster ensemble. Fig. 6.4 shows longitudinal MOKE loops of clusters of 4 ML Fe/100 L Xe at different temperature. At 34 K, the loop is open and the system exhibits remanence, as already seen in Fig. 6.3(b). Increasing the temperature results progressively in a decrease of the remanence. In Fig. 6.5 the remanent MOKE signal (\bullet) and the MOKE signal at 70 mT (\circ) are plotted as a function

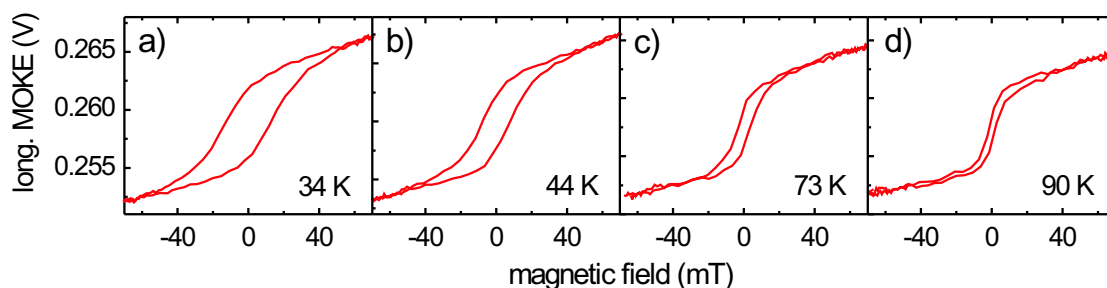


Figure 6.4: Longitudinal MOKE hysteresis loops of clusters of 4 ML Fe/100 L Xe taken at different temperature.

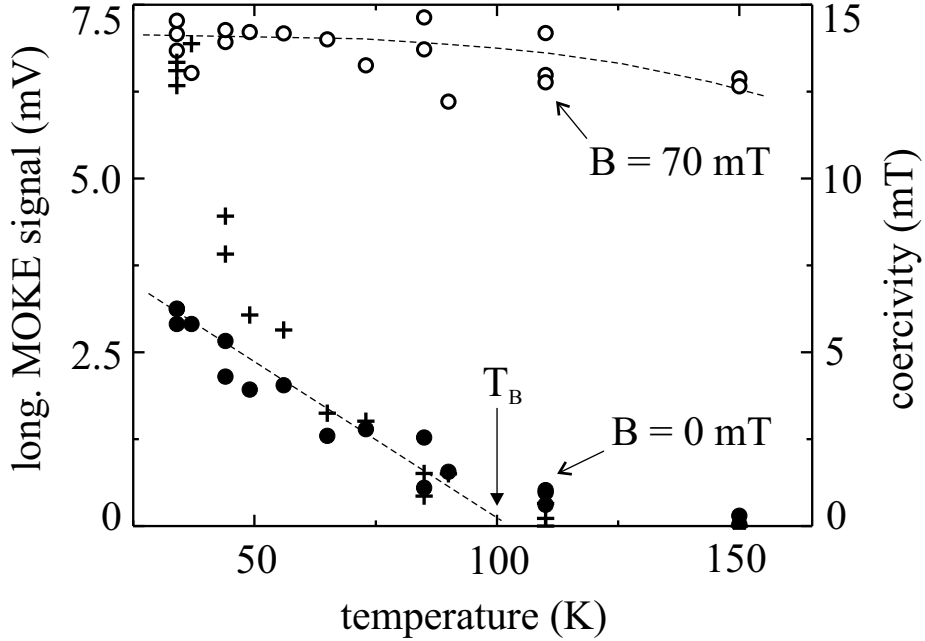


Figure 6.5: Temperature dependence of the magnetization of clusters of 4 ML Fe/100 L Xe measured in remanence (\bullet) and at 70 mT (\circ), and the coercivity ($+$). The dashed lines are guides to the eye.

of temperature. Additionally, also the temperature dependence of the coercive field is plotted ($+$). The data show that the remanent magnetization as well as the coercivity decrease with temperature and become zero at $T_B = 100$ K. In the same temperature range the MOKE signal at $H_{max} = 70$ mT remains unchanged. The difference below T_B between the remanent MOKE signal (\bullet) and the MOKE signal at 70 mT (\circ) might be due to several reasons, such as different orientation of the easy magnetization axis from cluster to cluster, an inhomogeneous clusters size distribution, or to the fact that the clusters are not saturated. It has been shown that the shape and the size of the clusters are stable as the sample temperature increases from 90 K to room temperature [153]. We can therefore exclude that the observed changes are due to thermal induced modification of the cluster structure and morphology.

The presented data are characteristic for superparamagnetic behavior of the deposited clusters. The observed temperature T_B is thus interpreted as the blocking temperature of the clusters formed of 4 ML Fe/100 L Xe/Pt. A rough estimate of the mean cluster size can be made by:

$$V \approx 25 \times \frac{k \cdot T_B}{E_A} \quad (6.1)$$

by assuming bulk magnetic anisotropy, $E_A = 5.8 \times 10^4$ J/m³, and inserting the exper-

imentally determined T_B and the Boltzmann factor, k . Assuming clusters of spherical shape and bulk lattice parameters, equation 6.1 gives a cluster diameter of 10.4 nm , containing 5.0×10^4 Fe atoms. In a similar way, for clusters formed of 2 ML Fe/100 L Xe a blocking temperature $T_B \simeq 50 \text{ K}$ is measured, giving a cluster diameter of $\sim 8.3 \text{ nm}$, or 2.5×10^4 Fe atoms per cluster. One can see that doubling the nominal Fe thickness roughly doubles the average number of Fe atoms per cluster.

In Fig. 6.3 has been shown that ultrathin Fe films on Pt exhibit perpendicular magnetization, whereas Fe clusters formed on 100 L Xe/Pt have the preferred magnetization direction within the film plane. The perpendicular easy axis observed, independently of the structure and morphology, for Fe films on Pt below 3 ML has been ascribed to the film-substrate interaction (Chapter 5). However, such films can not directly be compared to the Fe clusters due to the different local atomic structure at the Fe-Pt interface, which may result in different electronic interaction. Nevertheless, the height of the cluster is significantly larger than the critical coverage for the spin reorientation into the plane of Fe films grown directly on the Pt substrate. Clusters of 5 \AA Au/20 ML Xe have been found to have nearly constant height of $\sim 25 \text{ \AA}$ [172]. Assuming a similar height for the clusters of 2 ML Fe/18 ML Xe as presented here, we obtain a cluster height which is a factor 5 larger than the critical coverage observed for Fe films on bare Pt substrates. This argument indicates that interface contributions may not be relevant here and the magneto-static anisotropy is dominating, thus favoring in-plane magnetization axis. Besides the dominating shape anisotropy for the relaxed clusters, also inter-particle interactions as well as particle-substrate interactions can be expected to be relevant for the observed in-plane magnetization. It is generally recognized that dipole-dipole interaction in cluster and nanodot assemblies can affect the magnetic behavior [178, 179]. In addition, also the idea of indirect coupling between Fe nanodots through a Cu substrate promoting ferromagnetic in-plane ordering has been recently reported [180]. It is interesting to find at which minimum thickness of the Xe buffer layer the transition from perpendicular to in-plane magnetic anisotropy occurs. Results obtained on clusters of 2 ML Fe as a function of the Xe buffer layer thickness are presented in the following. Such experiment allows the investigation of cluster of different size, as well, since the cluster size strongly depends on the buffer layer thickness [175]. The measured magnetization loops are shown in Fig. 6.6. It can be concluded that in-plane anisotropy is obtained if the Xe buffer layer thickness is larger than 2 ML. The evaporation of a thinner Xe layer is not sufficient to complete the formation of clusters. The magnetization loops show an increase of the remanent magnetization with increasing the Xe thickness. This is indicative for an increase of T_B . In other words, larger clusters

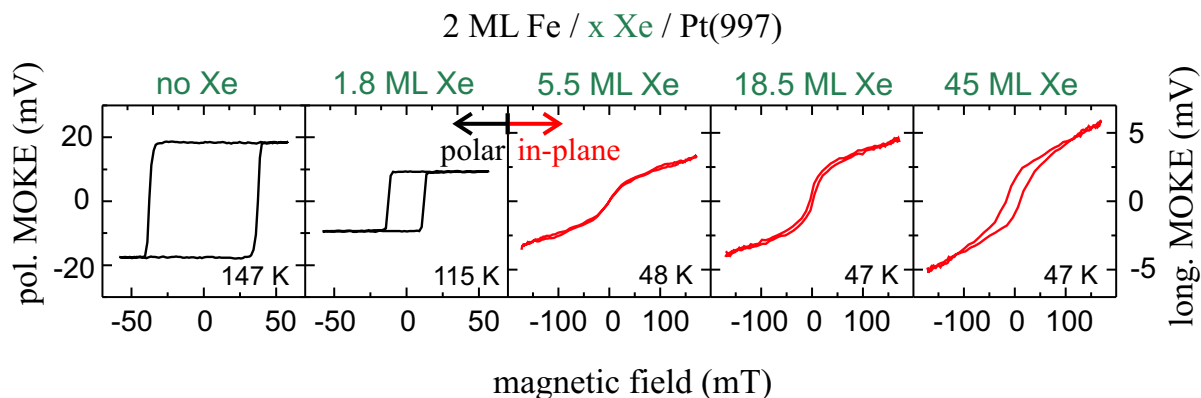


Figure 6.6: Magnetization loops observed at ~ 40 K on 2 ML Fe/Pt(997) grown on Xe buffer layer of different thickness. To reduce the coercivity, the temperature was increased for some measurements, as indicated in the figure.

are formed with increasing the Xe buffer layer thickness. A thicker layer needs longer time to sublimate providing more time for the cluster growth and for the coalescence of clusters into larger aggregates.

A further proof is given by the plot of the remanent MOKE signal (\bullet) and the

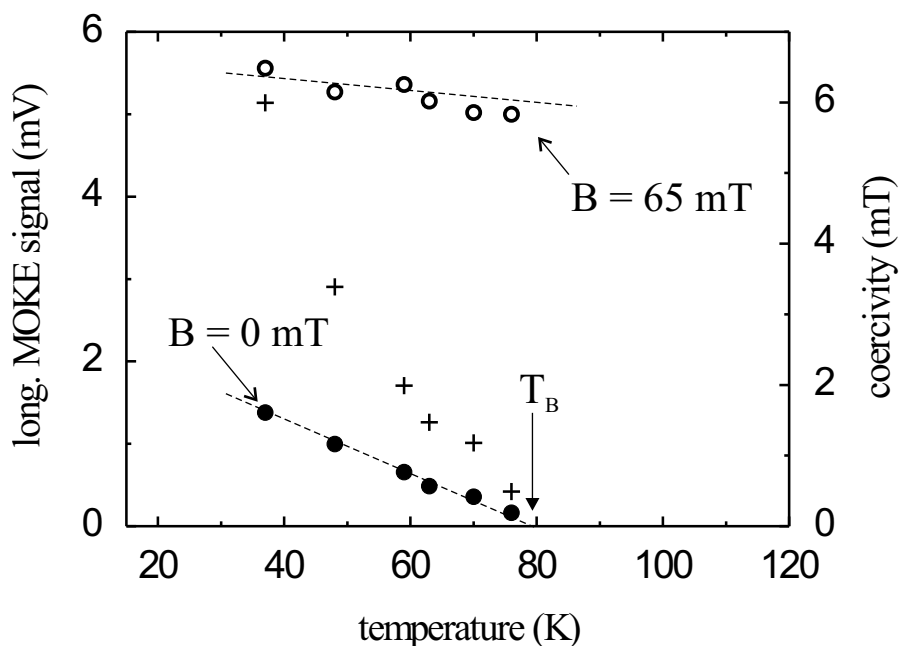


Figure 6.7: Temperature dependence of the magnetization of clusters of 2 ML Fe/100 L Xe measured in remanence (\bullet) and at 65 mT (\circ), and the coercivity (+). The dashed lines are guides to the eye.

MOKE signal at 65 mT (\circ) for clusters of 2 ML Fe formed on 250 L of Xe as a function of temperature (Fig. 6.7). From this plot, $T_B \simeq 80\text{ K}$ is determined, which is higher than $T_B \simeq 50\text{ K}$ found for clusters of 2 ML Fe/100 L Xe. Using Eq. (6.1), a cluster diameter of 9.7 nm can be estimated, which means that each cluster contains 4.0×10^4 Fe atoms if bulk Fe density is assumed. Similarly, for clusters of 4 ML Fe/30 L Xe a blocking temperature of $\sim 55\text{ K}$ has been measured, giving a cluster diameter of $\sim 8.6\text{ nm}$ or 2.8×10^4 Fe atoms per cluster. The results are summarized in Table 6.1. As a tendency, we see that cluster diameter and blocking temperature increase with Fe coverage on one hand, and with Xe layer thickness on the other hand.

Nominal Fe thickness (ML)	Xe buffer layer thickness (L)	Blocking temperature (K)	Cluster diameter (nm)	Fe atoms per cluster
4	30	55	8.6	2.8×10^4
4	100	100	10.4	5×10^4
2	100	50	8.3	2.5×10^4
2	250	80	9.7	4×10^4

Table 6.1: Blocking temperature and average size of Fe clusters (assumed of spherical shape) formed on Xe buffer layer of different thickness.

6.2.2 Epitaxial Fe films and strain effects

While the preparation on noble gas buffer layers supports the formation of Fe clusters independent of the substrate properties, the growth of Fe on Pt surfaces without Xe is significantly influenced by the growth dynamics and the lattice misfit to the substrate.

Epitaxial films on Pt substrates have been thoroughly studied in the previous chapter. A comparison between Fe structures prepared with and without the buffer layer is given in the following.

Epitaxial Fe films of 2 ML thickness grown on Pt substrates exhibit perpendicular magnetization. Fig. 6.8 shows a polar MOKE loop of 2 ML Fe/Pt(111) grown at RT and measured at 135 K . The result is clearly different from the case of Fe clusters of 2 ML Fe formed on the Xe buffer layer for which the preferred magnetization easy axis is within the film plane. In the previous chapter, the perpendicular easy axis observed on Fe films below $\theta_{crit} \sim 3\text{ ML}$ has been ascribed to the film-substrate interaction, neglecting the influence of the epitaxial strain due to the lattice mismatch with the substrate. However, such strain effects can significantly influence or even change the magnetism [35, 36].

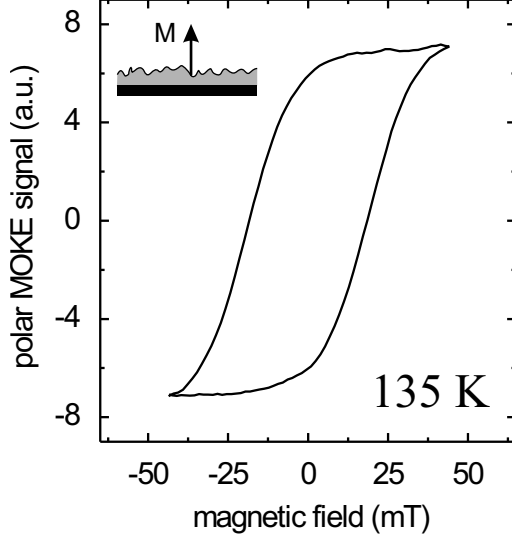


Figure 6.8: Polar MOKE loop measured at 135 K on 2 ML Fe (3.7 Å) grown on Pt(111) at 298 K.

The most striking difference between Fe clusters and islands is indeed, besides their specific morphologies, the lattice strain. The atoms of the first Fe layer occupy lattice sites provided by the Pt, thus forming a pseudomorphic fcc(111) layer. Assuming a lattice constant of fcc-Fe, $a_{Fe}^{fcc} = 3.59 \text{ \AA}$ [120] and of Pt, $a_{Pt} = 3.92 \text{ \AA}$, this implies a considerable epitaxial tensile strain of 9.2%! Such epitaxial strain is known to contribute to the total magnetic energy via the magneto-elastic (ME) coupling constant, B_1 . In order to estimate this contribution, I apply the phenomenological model, commonly used for thin epitaxial films, shown in

Sec. 1.1. The balance between the magneto-static energy:

$$\Delta f_{shape} = \frac{1}{2} \mu_0 M_S^2 \quad (6.2)$$

and the magneto-elastic energy:

$$\Delta f_{ME} = B_1(\varepsilon_{\perp} - \varepsilon_{\parallel}) \quad (6.3)$$

has to be analyzed. Both expressions represent energy differences between out-of-plane and in-plane magnetization and give negative values if the energy for perpendicular magnetization is lower than for an alignment of the magnetic moments within the plane.

The Δf_{ME} is calculated by using the value for B_1 found for strained Fe layers, $B_1^{eff} = 1 \times 10^7 \text{ J/m}^3$ and assuming the in-plane strain of $\varepsilon_{\parallel} = 0.092$. The B_1^{eff} reflects the observation that epitaxial films show a strain dependent ME coupling different from B_1^{bulk} . The value used here is an estimate based on experimentally determined B_1^{eff} for epitaxial Fe films on W(100) and the calculated value using a strain model [36]. The calculation of the strain perpendicular to the surface, ε_{\perp} , requires a transformation of the strain tensor into film coordinates [181]. One obtains $\varepsilon_{\perp} = -0.184$. Using Eq. (6.3)

$\Delta f_{ME} = -2.8 \times 10^6 J/m^3$ is calculated. This value provides an upper limit for the Δf_{ME} , since the pseudomorphic strain is assumed for the entire film. Yet, this simple model shows that the strain contribution alone is sufficient to defy the magneto-static energy of $\Delta f_{shape} = 1.9 \times 10^6 J/m^3$!

The estimate predicts a perpendicular magnetization for fcc(111)-Fe films due to strain, without consideration of surface anisotropy. Surface anisotropy contributions are usually significant and often dominate the magnetism of monolayer thin films. Surface and interface roughness (see for instance Fig. 5.1) are often found to influence the magnitude of the surface anisotropy [126]. Such contributions to the anisotropy arising from the film morphology can be only determined by a complex analysis for each individual system and are neglected in this estimate for simplicity.

Conclusions and outlook

In this thesis, investigations of the correlation between structure, morphology and magnetic properties of atomically thin films and clusters at surfaces for different film/substrate systems have been presented.

The experiments on ultrathin epitaxial Fe films grown on Cu(100) at 120 K show unambiguously that annealing causes reversible and irreversible changes of the magnetic properties of the films. I have described an experiment which allows to determine both contributions to the surface anisotropy separately. Reversible shifts are attributed to the temperature dependence of the surface anisotropy constants. In contrast, irreversible changes have been correlated with changes of the Fe island diameter during annealing. Furthermore, the Fe islands have been found to substantially shape the potential energy surface which is seen by a domain wall during magnetization reversal process. The experiments show clearly that both the height *and* the distribution of the energy barriers within the films are decisive for the film magnetism: The measurements of the magnetic viscosity show that with increasing temperature or applied magnetic field the effective barrier height for magnetization reversal, and thus the necessary activation energy, decreases. As a consequence, the Barkhausen length increases with temperature. The reversible dependence on temperature suggests that the measured Barkhausen length is independent of the film morphology and rather determined by an avalanche-like domain wall propagation. In contrast, the irreversible increase of the coercivity is interpreted as an efficient domain wall trapping due to a morphology-related change in barrier distribution, while the barrier height itself remains unchanged.

Ultrathin Fe films grown on Cu(100) at RT have been used as templates for the fabrication of fcc-Fe/Cu/Fe trilayers. Perpendicular coupling was found between the Fe layers and ascribed to magneto-static interaction. The perpendicular magnetic anisotropy arises at the Fe-vacuum interface and governs the magnetization of the whole trilayer. Without the top Fe layer, in-plane magnetization is found for Cu/Fe/Cu(100). A reorientation into the plane of the top Fe layer magnetization by oxygen adsorption determines a switching into the plane of the bottom layer magnetization, further suggesting the

governing role of the top Fe layer. No RKKY-type oscillations of the magnetic signal as a function of the spacer thickness are observed. The interlayer exchange coupling is assumed to be strongly reduced by the observed interface roughness, as suggested by theory. Due to the suppressed interlayer exchange interaction, magneto-static coupling phenomena become directly observable.

The results on atomically thin Fe films on flat Pt(111) and stepped Pt(997) surfaces underline the fundamental importance of the substrate choice for nanostructure fabrication, due to the possibility to control the structure, the morphology and the magnetism at the ultrathin film limit. Stranski-Krastanov and Volmer-Weber growth modes have been observed with and without the presence of substrate steps, respectively. In spite of the different structure and morphology, an out-of-plane magnetization easy axis was observed on both systems below 3 ML. This finding suggests that the perpendicular magnetic anisotropy is rather governed by the Fe-Pt interface, whereas the film structure itself seems to be only of minor importance. In contrast to that, for the bcc-films at higher Fe coverage we propose a direct correlation between atomic structure and in-plane anisotropy. The suppression of four out of six structural bcc-domains with Kurdjumov-Sachs orientation to the substrate results in a preferred in-plane magnetization direction parallel to the substrate step edges. Oxygen adsorption experiments disprove the importance of the Fe-vacuum interface for the magnetic anisotropy of Fe/Pt, but suggest a direct decrease of the exchange interaction in the film. Due to the interesting correlation between structural and anisotropy asymmetries, Fe films on Pt may serve as a further model system to study the atomistic and electronic origin of magnetic anisotropy contributions in ultrathin films.

Fe clusters have been prepared on Pt substrates by Xe buffer layer assisted growth. The advantage of this technique is that magnetic nanostructures can be prepared on substrate surfaces without the limitations and implications typically arising from the lattice mismatching in molecular beam epitaxy. The relaxed strain free clusters show superparamagnetic behavior and in-plane anisotropy below the blocking temperature. By combining STM with magnetic measurements, a correlation between cluster size and spacing and magnetic interaction between clusters will be possible.

The results of this thesis represent a starting point for future, more complex nanostructuring experiments. The new UHV system with its VT-STM will allow for an improved correlation between structure, morphology, electronic structure, chemical composition and magnetism and aims towards imaging of magnetism on the atomic scale by spin-polarized tunnelling experiments.

The systems studied in this thesis will greatly benefit from complementary STM

investigations. Imaging of the morphology of Fe films on stepped Pt substrates as well as of the clusters formed by noble gas assisted growth will be immediate continuations of this project.

Nanostructuring into the third dimension can be done on the basis of the results of this thesis. The next step could be the formation of artificial $(1 \text{ ML Fe}/1 \text{ ML Pt})_n$ superlattices. Strong hybridization effects and indirect exchange interaction are expected for this system, with direct consequences for the magnetism. A further extension could be the growth of superlattices of FePt monolayers and Pt layers.

Also the possibility to fabricate Fe clusters embedded into a "sea" of Pt is a fascinating prospect. Clusters formed by the procedure described in this thesis could be covered with a Pt layer, on which further clusters could be formed with the same noble gas assisted method. Instead of Pt also Ag, which exhibits a much simpler electronic structure, could be used. Besides the coupling between the clusters, also the interaction with and the polarization of the host material could be investigated. Such bottom-up approaches can now easily be done and are already steps on the road towards three dimensional nanostructuring.

Acknowledgements

It is not easy to thank all the people who helped me during my PhD in the last three years. Sometimes, even a small contribution, a short discussion or an idea captured at the coffee corner can be very helpful. It could be that someone, reading these acknowledgements, will be disappointed to not find her/his name, though she/he would have deserved it. Believe me, it was not on purpose and first of all I would like to apologize those people.

I would like to thank Prof. Klaus Kern for having given me the possibility to do the PhD in his group.

It's not easy to find the words to thank Axel Enders. First of all, he has been and still is a good friend. We could always speak openly, even when we had some problems. I felt involved in any decision, he never told me to do something without previously discussing with me. His optimism, his smiling face, his "take it easy" were fundamental to overcome all the difficult moments. Moreover, he taught me how to use the UHV system and many other things in the field of magnetism. He represents the proof that it's much easier to learn something from someone who enjoys teaching. Axel is really close to my idea of best supervisor that a PhD student might have.

Then, I would like to thank Dietrich Peterka and Jan Honolka, friends and colleagues of the "magnetism subgroup". I also thank all the people who have collaborated with me: Magalí Lingenfelder, Prof. Bret Heinrich and his group in Vancouver, Dr. Taeyon Lee, Dr. Klaus Kuhnke, Dr. Rudiger Vollmer, Dr. Stefano Rusponi, Prof. Harald Brune.

I thank the technicians of our group, Wolfgang Stiepany, Rafail Chaikévitch, Wolfgang Heinz, Martin Siemers, Andreas Koch, and the people of the workshop for having done the work that physicists are not able to do. I thank Artur Küster for his help during my learning of the "Solid Designer Modelling" program. I also thank Franck Dahlem and Pietro Gambardella for the translation in French of the abstract.

I thank Giovanni Costantini for having given hospitality to me during the first three months in Stuttgart. And of course, last but not least, I want to thank all the nice,

interesting and friendly people I have met in these three years in Stuttgart. They are too numerous to be mentioned here, although they would deserve it because I have really spent a great time with them. There is one thing I'm sure of: I could enjoy the work in the institute because outside I have enjoyed the life!

Bibliography

- [1] C. M. Schneider and J. Kirschner, *Handbook of Surface Science, edited by Horn, K. and Scheffler, M.* (Elsevier, Amsterdam, 2000), p. 511.
- [2] U. Gradmann, *in: Handbook of Magnetic Materials, edited by K. H. J. Buschow* (Elsevier, Amsterdam, 1993), Vol. VII.
- [3] J. Shen and J. Kirschner, *Surf. Sci.* **500**, 300 (2002).
- [4] D. M. Eigler and E. K. Schweizer, *Nature* **344**, 524 (1990).
- [5] M. F. Crommie, C. P. Lutz, and D. M. Eigler, *Science* **262**, 218 (1993).
- [6] H. Röder, E. Hahn, H. Brune, J.-P. Bucher, and K. Kern, *Nature* **366**, 141 (1993).
- [7] H. Brune, M. Giovannini, K. Bromann, and K. Kern, *Nature* **394**, 451 (1998).
- [8] P. Gambardella, A. Dallmeyer, K. Maiti, M. C. Malagoli, W. Eberhardt, K. Kern, and C. Carbone, *Nature* **416**, 301 (2002).
- [9] J. Thomassen, F. May, B. Feldmann, M. Wuttig, and H. Ibach, *Phys. Rev. Lett.* **69**, 3831 (1992).
- [10] D. Pescia, M. Stampanoni, G. L. Bona, A. Vaterlaus, R. F. Willis, and F. Meier, *Phys. Rev. Lett.* **58**, 2126 (1987).
- [11] M. Stampanoni, A. Vaterlaus, M. Aeschlimann, F. Meier, and D. Pescia, *J. Appl. Phys.* **64**, 5321 (1988).
- [12] J. Thomassen, B. Feldmann, and M. Wuttig, *Surf. Sci.* **264**, 406 (1992).
- [13] M. Wuttig and J. Thomassen, *Surf. Sci.* **282**, 237 (1993).
- [14] P. Bayer, S. Müller, P. Schmailzl, and K. Heinz, *Phys. Rev. B* **48**, 17611 (1993).
- [15] M. Wuttig, B. Feldmann, F. Thomassen, J. May, H. Zillgen, A. Brodde, H. Hanemann, and H. Neddermeyer, *Surf. Sci.* **291**, 14 (1993).
- [16] P. Schmailzl, K. Schmidt, P. Bayer, R. Döll, and K. Heinz, *Surf. Sci.* **312**, 73 (1994).

- [17] H. Zillgen, B. Feldmann, and M. Wuttig, *Surf. Sci.* **321**, 32 (1994).
- [18] D. Li, M. Freitag, J. Pearson, Z. Q. Qiu, and S. D. Bader, *Phys. Rev. Lett.* **72**, 3112 (1994).
- [19] D. Li, M. Freitag, J. Pearson, Z. Q. Qiu, and S. D. Bader, *J. Appl. Phys.* **76**, 6426 (1994).
- [20] S. Müller, P. Bayer, A. Kinne, C. Reischl, R. Metzler, and K. Heinz, *Surf. Sci.* **333**, 723 (1995).
- [21] S. Müller, P. Bayer, C. Reischl, K. Heinz, B. Feldmann, H. Zillgen, and M. Wuttig, *Phys. Rev. Lett.* **74**, 765 (1995).
- [22] B. Újfalussy, L. Szunyogh, and P. Weinberger, *Phys. Rev. B* **54**, 9883 (1996).
- [23] R. Vollmer, T. Gutjahr-Löser, J. Kirschner, S. van Dijken, and B. Poelsema, *Phys. Rev. B* **60**, 6277 (1999).
- [24] J. Shen, A. K. Swan, and J. F. Wendelken, *App. Phys. Lett.* **75**, 2987 (1999).
- [25] D. Schmitz, C. Charton, A. Scholl, C. Carbone, and W. Eberhardt, *Phys. Rev. B* **59**, 4327 (1999).
- [26] A. Biedermann, M. Schmid, and P. Varga, *Phys. Rev. Lett.* **86**, 464 (2000).
- [27] R. Vollmer, S. van Dijken, M. Schleberger, and J. Kirschner, *Phys. Rev. B* **61**, 1303 (2000).
- [28] R. E. Camley, *J. Appl. Phys.* **89**, 7142 (2001).
- [29] D. Qian, X. F. Jin, J. Barthel, M. Klaua, and J. Kirschner, *Phys. Rev. Lett.* **87**, 227204 (2001).
- [30] P. F. Carcia, A. D. Meinhaldt, and A. Suna, *Appl. Phys. Lett.* **47**, 178 (1985).
- [31] J. Elmers, *J. Magn. Magn. Mater.* **185**, 274 (1998).
- [32] A. J. Freeman and C. L. Fu, *J. Appl. Phys.* **61**, 3356 (1987).
- [33] B. Heinrich, K. B. Urquhart, A. S. Arrott, J. F. Cochran, K. Myrtle, and S. T. Purcell, *Phys. Rev. Lett.* **59**, 1756 (1987).
- [34] N. C. Koon, B. T. Jonker, F. A. Volkening, J. J. Krebs, and G. A. Prinz, *Phys. Rev. Lett.* **59**, 2463 (1987).
- [35] S. W. Sun and R. C. O'Handley, *Phys. Rev. Lett.* **66**, 2798 (1991).
- [36] A. Enders, D. Sander, and J. Kirschner, *J. Appl. Phys.* **85**, 5279 (1999).

- [37] R. Bergholz and U. Gradmann, *J. Mag. Mag. Mater.* **45**, 389 (1984).
- [38] Y. Li, K. Baberschke, and M. Farle, *J. Appl. Phys.* **69**, 4992 (1991).
- [39] L. Néel, *J. Phys. Radium* **15**, 376 (1954).
- [40] J. Stöhr, *J. Magn. Magn. Mater.* **200**, 470 (1999).
- [41] H. van Vleck, *Phys. Rev.* **52**, 1178 (1937).
- [42] P. Bruno, *Phys. Rev. B* **39**, 865 (1989).
- [43] G. van der Laan, *J. Phys.: Condens. Matter* **10**, 3239 (1998).
- [44] P. Gambardella, S. Rusponi, M. Veronese, S. Dhesi, C. Grazioli, A. Dallmeyer, I. Cabria, R. Zeller, P. Dederichs, K. Kern, C. Carbone, and H. Brune, *Science* **300**, 1130 (2003).
- [45] C. Kittel, *Einführung in die Festkörperphysik* (R. Oldenburg-Verlag, München, 1996).
- [46] C. Kittel, *Phys. Rev.* **70**, 965 (1946).
- [47] D. Sander, R. Skomski, C. Schmidhals, A. Enders, and J. Kirschner, *Phys. Rev. Lett.* **77**, 2566 (1996).
- [48] S. Boukari, R. Allenspach, and A. Bishof, *Phys. Rev. B* **63**, 180402 (2001).
- [49] H. Barkhausen, *Phys. Z.* **29**, 401 (1919).
- [50] A. Moser and D. Weller, *IEEE Trans. Magn.* **35**, 4423 (1999).
- [51] P. Bruno, G. Bayreuther, P. Beauvillain, C. Chappert, G. Lugert, D. Renard, J. P. Renard, and J. Seiden, *J. Appl. Phys.* **68**, 5759 (1990).
- [52] G. Bayreuther, P. Bruno, G. Lugert, and C. Turtur, *Phys. Rev. B* **40**, 7399 (1989).
- [53] J. Pommier, P. Meyer, G. Pénissard, J. Ferré, P. Bruno, and D. Renard, *Phys. Rev. Lett.* **65**, 2054 (1990).
- [54] A. Kirilyuk, J. Ferré, and D. Renard, *IEEE Trans. Magn.* **29**, 2518 (1993).
- [55] A. Kirilyuk, J. Giergiel, J. Shen, and J. Kirschner, *J. Magn. Magn. Mater.* **159**, L27 (1996).
- [56] A. Bauer, E. Mentz, and G. Kaindl, *J. Magn. Magn. Mater* **199**, 489 (1999).
- [57] R. P. Cowburn, J. Ferré, S. J. Gray, and J. A. C. Bland, *Phys. Rev. B* **58**, 11507 (1998).

- [58] M. Labrune, S. Andrieu, F. Rio, and P. Bernstein, *J. Magn. Magn. Mater* **80**, 211 (1989).
- [59] E. Fatuzzo, *Phys. Rev.* **127**, 1999 (1962).
- [60] Y. P. Zhao, R. M. Gamache, G. C. Wang, T. M. Lu, G. Palasantzas, and J. T. M. D. Hosson, *J. Appl. Phys.* **89**, 1325 (2001).
- [61] P. Grünberg, R. Schreiber, Y. Pang, M. B. Brodsky, and C. H. Sowers, *Phys. Rev. Lett.* **57**, 2442 (1986).
- [62] B. Heinrich, Z. Celinski, J. F. Cochran, W. B. Muir, J. Rudd, Q. M. Zhong, A. S. Arrot, K. Myrtle, and J. Kirschner, *Phys. Rev. Lett.* **64**, 673 (1990).
- [63] S. S. P. Parkin, *Phys. Rev. Lett.* **67**, 3598 (1991).
- [64] M. T. Johnson, S. T. Purcell, N. W. E. McGee, R. Coehoorn, J. aan de Stegge, and W. Hoving, *Phys. Rev. Lett.* **68**, 2688 (1992).
- [65] A. T. Costa, J. d'Albuquerque e Castroand, R. B. Muniz, M. S. Ferreira, and J. Mathon, *Phys. Rev.B* **55**, 3724 (1997).
- [66] J. Unguris, R. J. Celotta, and D. T. Pierce, *Phys. Rev. Lett.* **79**, 2734 (1997).
- [67] P. Bruno, *J. Phys.: Condens. Matter* **11**, 9403 (1999).
- [68] W. R. Bennett, W. Schwarzbacher, and W. F. Egelhoff, *Phys. Rev. Lett.* **65**, 3169 (1990).
- [69] V. Grolier, D. Renard, B. Bartenlian, P. Beauvillain, C. Chappert, C. Dupas, J. Ferré, M. Galtier, E. Kolb, M. Mulloy, J. P. Renard, and P. Veillet, *Phys. Rev. Lett.* **71**, 3023 (1993).
- [70] G. Gubbiotti, G. Carlotti, M. A. Ciria, F. Spizzo, R. Zivieri, L. Giovannini, F. Nizzoli, and R. C. O'Handley, *J. Magn. Magn. Mater.* **240**, 461 (2002).
- [71] P. Bruno and C. Chappert, *Phys. Rev. Lett.* **67**, 1602 (1991).
- [72] P. Bruno and C. Chappert, *Phys. Rev. B* **46**, 261 (1992).
- [73] L. Néel, *C. R. Hebd. Sean. Acad. Sci.* **255**, 1676 (1962).
- [74] J. Moritz, F. Garcia, J. C. Toussaint, B. Dieny, and J. P. Nozières, *Europhys. Lett.* **65**, 123 (2004).
- [75] J. Giergiel, J. Shen, J. Woltersdorf, A. Kirilyuk, and J. Kirschner, *Phys. Rev. B* **52**, 8528 (1995).

- [76] A. Biedermann, R. Tscheließnig, M. Schmid, and P. Varga, *Phys. Rev. Lett.* **87**, 086103 (2001).
- [77] D. Peterka, A. Enders, G. Haas, and K. Kern, *Phys. Rev. B* **66**, 104411 (2002).
- [78] M. A. Ruderman and C. Kittel, *Phys. Rev.* **96**, 99 (1954).
- [79] T. Kasuya, *Progr. Theor. Phys.* **16**, 45 (1956).
- [80] K. Yosida, *Phys. Rev.* **106**, 893 (1957).
- [81] J. Friedel, *Nuovo Cimento Suppl.* **7**, 287 (1958).
- [82] P. Bruno, *J. Magn. Magn. Mater.* **116**, L13 (1992).
- [83] M. Rühlig, R. Schäfer, A. Hubert, R. Mosler, J. A. Wolf, S. Demokritov, and P. Grünberg, *Phys. Status Solidi (a)* **125**, 635 (1991).
- [84] K. Pettit, S. Gider, S. S. P. Parkin, and M. B. Salamon, *Phys. Rev. B* **56**, 7819 (1997).
- [85] B. Heinrich and J. F. Cochran, *Adv. in Phys.* **42**, 523 (1993).
- [86] J. C. Slonczewski, *J. Appl. Phys.* **73**, 5957 (1993).
- [87] J. C. Slonczewski, *J. Magn. Magn. Mater.* **150**, 13 (1995).
- [88] P. M. Levy, S. Maekawa, and P. Bruno, *Phys. Rev. B* **58**, 5588 (1998).
- [89] J. Unguris, R. J. Celotta, and D. T. Pierce, *Phys. Rev. Lett.* **67**, 140 (1991).
- [90] C. Daboo, J. A. C. Bland, R. J. Hicken, A. J. R. Ives, M. J. Baird, and M. J. Walker, *J. Appl. Phys.* **73**, 6368 (1993).
- [91] Z. J. Yang and M. R. Scheinfein, *Phys. Rev. B* **52**, 4263 (1995).
- [92] N. M. Kreines, D. I. Kholin, S. O. Demokritov, and M. Rikart, *JEPT Lett.* **78**, 627 (2003).
- [93] J. Thomassen, F. May, B. Feldmann, M. Wuttig, and H. Ibach, *Phys. Rev. Lett.* **69**, 3831 (1992).
- [94] J. Kranz and W. Drechsel, *Zeits. Phys.* **150**, 632 (1958).
- [95] J. Kranz and A. Hubert, *Zeits. Angew. Phys.* **15**, 220 (1963).
- [96] D. Peterka, A. Enders, G. Haas, and K. Kern, *Rev. Sci. Instrum.* **74**, 2744 (2003).
- [97] D. Peterka, Ph.D. thesis, *École Polytechnique Fédérale de Lausanne*, (2002).

- [98] G. Binning, H. Rohrer, C. Gerber, and E. Weibel, *Phys. Rev. Lett.* **49**, 57 (1982).
- [99] G. Binning and H. Rohrer, *Helv. Phys. Acta* **55**, 726 (1982).
- [100] F. Besenbacher, F. Jensen, E. Lægsgaard, K. Mortensen, and I. Stensgaard, *J. Vac. Sci. Techn. B* **9**, 874 (1990).
- [101] F. Jensen, F. Besenbacher, E. Lægsgaard, and I. Stensgaard, *Phys. Rev. B* **42**, 9206 (1990).
- [102] B. C. Stipe, M. A. Rezaei, and W. Ho, *Rev. Sci. Instrum.* **70**, 137 (1999).
- [103] K. Besocke, *Surf. Sci.* **181**, 145 (1987).
- [104] J. Kerr, *Phil. Mag.* **3**, 321 (1877).
- [105] M. Faraday, *Phil. Trans. Roy. Soc.* **136**, 1 (1846).
- [106] W. Voigt, *Handbuch der Elektrizität und des Magnetismus*, edited by L. Graetz (A. Barth, Leipzig, 1920), Vol. IV, pp. 667–710.
- [107] A. Bauer, *Far-Field and Near-Field Magneto-Optical Microscopy of Ultrathin Films*, Habilitation, Freie Universität Berlin, 2000.
- [108] A. Hubert and R. Schäfer, *Magnetic Domains* (Springer-Verlag, Berlin, 2000).
- [109] B. E. Argyle, B. Petek, and J. Herman, *J. Appl. Phys.* **61**, 4303 (1987).
- [110] E. Bauer, *Z. Kristallogr.* **110**, 372 (1958).
- [111] M. Onellion, M. A. Thompson, J. L. Erskine, C. B. Duke, and A. Paton, *Surf. Sci.* **179**, 219 (1987).
- [112] J. Shen, M. Klaua, P. Ohresser, H. Jenniches, J. Barthel, C. Mohan, and J. Kirschner, *Phys. Rev. B* **56**, 11134 (1997).
- [113] D. Repetto, J. Honolka, S. Rusponi, H. Brune, A. Enders, and K. Kern, (2005) (accepted for publication in *Appl. Phys. A*).
- [114] T. Y. Lee, S. Sarbach, K. Kuhnke, and K. Kern, *Cond-mat*, 0504337 (2005).
- [115] J. Giergiel, J. Kirschner, J. Landgraf, J. Shen, and J. Woltersdorf, *Surf. Sci.* **310**, 1 (1994).
- [116] R. Allenspach and A. Bischof, *Phys. Rev. Lett.* **69**, 3385 (1992).
- [117] A. Enders, D. Peterka, D. Repetto, N. Lin, A. Dmitriev, and K. Kern, *Phys. Rev. Lett.* **90**, 217203 (2003).

- [118] B. Heinrich, Z. Celinski, J. F. Cochran, A. S. Arrott, and K. Myrtle, *J. Appl. Phys.* **70**, 5769 (1991).
- [119] Landolt-Börnstein, *in: Structure Data of Elements and Intermetallic Phases*, new series ed. (Springer-Verlag, Berlin, 1971), Vol. III/6.
- [120] F. Jona and P. M. Marcus, *Crit. Rev. Surf. Chem.* **4**, 189 (1994).
- [121] T. Gutjahr-Löser, Ph.D. thesis, Martin-Luther-Univ. Halle-Wittenberg, (1999).
- [122] Landolt-Börnstein, *in: Magnetic Properties of Metals: 3d, 4d and 5d Elements, Alloys and Compounds*, new series ed. (Springer-Verlag, Berlin, 1971), Vol. III/19a, p. 49.
- [123] E. Callen, *J. Appl. Phys.* **53**, 8139 (1982).
- [124] A. Ecker, P. Fröbrich, P. Jensen, and P. Kuntz, *J. Phys.: Condens. Matter* **11**, 1557 (1999).
- [125] M. Farle, B. Mirwald-Schulz, A. N. Anisimov, W. Platow, and K. Baberschke, *Phys. Rev. B* **55**, 3708 (1997).
- [126] P. Bruno, *J. Phys. F: Met. Phys.* **18**, 1291 (1988).
- [127] D. A. Steigerwald, I. Jacob, and W. F. Egelhoff, *Surf. Sci.* **202**, 472 (1988).
- [128] S. Moran, C. Ederer, and M. Fahnle, *Phys. Rev. B* **67**, 012407 (2003).
- [129] M. Pajda, J. Kudrnovský, I. Turek, V. Drchal, and P. Bruno, *Phys. Rev. Lett.* **85**, 5424 (2000).
- [130] A. Enders, D. Repetto, D. Peterka, and K. Kern, (2005) (accepted for publication in *Phys. Rev. B*).
- [131] A. Enders, D. Repetto, T. Y. Lee, and K. Kern, *J. Magn. Magn. Mater.* **272-276**, Supp. 1, E959 (2004).
- [132] D. Repetto, A. Enders, and K. Kern, (2005) (accepted for publication in *J. Magn. Magn. Mater.*).
- [133] M. Speckmann, H. P. Oepen, and H. Ibach, *Phys. Rev Lett.* **75**, 2035 (1995).
- [134] H. W. Zhao, Y. Z. Wu, C. Won, F. Toyoma, and Z. Q. Qiu, *Phys. Rev. B* **66**, 104402 (2002).
- [135] W. Weber, C. H. Back, A. Bischof, D. Pescia, and R. Allenspach, *Nature* **374**, 788 (1995).

- [136] M. E. Buckley, F. O. Schumann, and J. A. C. Bland, *Phys. Rev. B* **52**, 6596 (1995).
- [137] P. Ferro, R. Moroni, M. Salvetti, M. Canepa, and L. Mattera, *Surf. Sci.* **407**, 212 (1998).
- [138] R. Moroni, F. Bisio, M. Canepa, and L. Mattera, *Appl. Surf. Sci.* **175-176**, 797 (2001).
- [139] A. Taga, L. Nordström, P. James, B. Johansson, and O. Eriksson, *Nature* **406**, 280 (2000).
- [140] W. Kuch, X. Gao, and J. Kirschner, *Phys. Rev. B* **65**, 064406 (2002).
- [141] F. Dulot, B. Kierren, and D. Malterre, *Surf. Sci.* **494**, 229 (2001).
- [142] U. Gradmann, *J. Magn. Magn. Mater.* **100**, 481 (1991).
- [143] R. Allenspach, *J. Magn. Mag. Mat.* **129**, 160 (1994).
- [144] B. Heinrich, *in: Ultrathin Magnetic Structures, edited by B. Heinrich and J. A. C. Bland* (Springer-Verlag, Berlin, 1994), Vol. II, and references therein.
- [145] D. S. Chuang, C. A. Ballentine, and R. C. O'Handly, *Phys. Rev. B* **49**, 15084 (1994).
- [146] R. K. Kawakami, E. J. Escorcia-Aparicio, and Z. Q. Qiu, *Phys. Rev. Lett.* **77**, 2570 (1996).
- [147] E. J. Escorcia-Aparicio, H. J. Choi, W. L. Ling, R. K. Kawakami, and Z. Q. Qiu, *Phys. Rev. Lett.* **81**, 2144 (1998).
- [148] W. Weiss and M. Ritter, *Phys. Rev. B* **59**, 5201 (1999).
- [149] D. I. Jerdev and B. E. Koel, *Surf. Sci.* **513**, L391 (2002).
- [150] D. Sander, A. Enders, C. Schmidhals, D. Reuter, and J. Kirschner, *J. Magn. Magn. Mater.* **177**, 1299 (1998).
- [151] S. Rusponi, T. Cren, and H. Brune, EPF Lausanne, Switzerland, private communication.
- [152] U. Starke, (2005) (to be published).
- [153] J. Shen, J. P. Pierce, E. W. Plummer, and J. Kirschner, *J. Phys.: Condens. Matter* **15**, R1 (2003).
- [154] T. Y. Lee, K. Kuhnke, A. Enders, J. Honolka, D. Repetto, C. Grazioli, K. Menom, M. Veronese, C. Carbone, and K. Kern, (in preparation).

- [155] J. Honolka, T. Y. Lee, K. Kuhnke, A. Enders, K. Kern, K. Fauth, M. Hessler, and G. Schütz, (2005) (submitted).
- [156] W. Weber, C. H. Back, U. Ramsperger, A. Vaterlaus, and R. Allenspach, *Phys. Rev. Lett.* **52**, R14400 (1995).
- [157] E. J. Escorcia-Aparicio, J. H. Wolfe, H. J. Choi, W. L. Ling, R. K. Kawakami, and Z. Q. Qiu, *Phys. Rev. B* **59**, 11892 (1999).
- [158] H. C. Mireles and J. L. Erskine, *Phys. Rev. Lett.* **87**, 037201 (2001).
- [159] C. Boeglin, S. Stanescu, J. P. Deville, P. Ohresser, and N. B. Brookes, *Phys. Rev. B* **66**, 014439 (2002).
- [160] D. Sander, W. Pan, S. Ouazi, J. Kirschner, W. Meyer, M. Krause, S. Muller, L. Hammer, and K. Heinz, *Phys. Rev. Lett.* **93**, 247203 (2004).
- [161] F. May, M. Tischer, D. Arvanitis, M. Russo, J. H. Dunn, H. Henneken, H. Wende, R. Chauvistré, N. Mårtensson, and K. Baberschke, *Phys. Rev. B* **53**, 1076 (1996).
- [162] W. Weber, D. Kerkmann, D. Pescia, D. A. Wesner, and G. Güntherodt, *Phys. Rev. Lett.* **65**, 2058 (1990).
- [163] D. S. Wang, R. Wu, and A. J. Freeman, *J. Magn. Magn. Mater.* **129**, 237 (1994).
- [164] P. Bruno, *Phys. Rev. B* **43**, 6015 (1991).
- [165] K. Terakura, N. Hamada, T. Oguchi, and T. Asada, *J. Phys. F: Met. Phys.* **12**, 1661 (1982).
- [166] T. Martin, *Phys. Rept.* **273**, 199 (1996).
- [167] W. de Heer, *Rev. Mod. Phys.* **65**, 611 (1993).
- [168] K. Wildberger, V. Stepanyuk, P. Lang, R. Zeller, and P. Dederichs, *Phys. Rev. Lett.* **75**, 509 (1995).
- [169] G. Pastor, J. Dorantes-Dávila, S. Pick, and H. Dreyssé, *Phys. Rev. Lett.* **75**, 326 (1995).
- [170] K. Bromann, C. Felix, H. Brune, W. Harbich, R. Monot, J. Buttet, and K. Kern, *Science* **274**, 956 (1996).
- [171] J. H. Weaver and G. Waddill, *Science* **251**, 1444 (1991).
- [172] C. Haley and J. H. Weaver, *Surf. Sci.* **518**, 243 (2002).
- [173] O. Fruchart, M. Klaua, J. Barthel, and J. Kirschner, *Phys. Rev. Lett.* **83**, 2769 (1999).

- [174] Z. Gai, B. Wu, J. P. Pierce, G. A. Farnan, D. Shu, M. Wang, Z. Zhang, and J. Shen, *Phys. Rev. Lett.* **89**, 235502 (2002).
- [175] L. Huang, S. J. Chey, and J. H. Weaver, *Phys. Rev. Lett.* **80**, 4095 (1998).
- [176] J. H. Weaver and V. N. Antonov, *Surf. Sci.* **557**, 1 (2004).
- [177] D. Repetto, T. Y. Lee, S. Rusponi, J. Honolka, K. Kuhnke, H. Brune, A. Enders, and K. Kern, (2005) (submitted).
- [178] D. Kechrakos and K. Trohidou, *Phys. Rev. B* **58**, 12169 (1998).
- [179] V. Novosad, K. Y. Guslienko, H. Shima, Y. Otani, S. G. Kim, K. Fukamichi, N. Kikuchi, O. Kitakami, and Y. Shimada, *Phys. Rev. B* **65**, 60402 (2002).
- [180] J. Pierce, M. Torija, Z. Gai, J. Shi, T. Schulthess, G. Farnan, J. Wendelken, E. Plummer, and J. Shen, *Phys. Rev. Lett.* **92**, 237201 (2004).
- [181] D. Sander, *Rep. Prog. Phys.* **62**, 809 (1999).

Curriculum vitae

Name: Diego Repetto
Date of Birth: 22nd May 1975
Nationality: Italian

Education and scientific activities:

1989 – 1994 High school at Istituto Tecnico Nautico C. Colombo, Camogli, Genova, Italy

Mar. 1999 – Dec. 1999 Diploma work at Micro Engineering Department in the group of Prof. R. Popovic at École Polytechnique Fédéral de Lausanne, Switzerland

1994 – 2000 Diploma di Laurea in Fisica at Università degli studi di Genova, Italy

Jun. 2001 – Jul. 2001 Teacher of electronics, electrotechnics and electric machines in a "Course of Retraining for Master for Engine-room Officers", La Habana, Cuba

Apr. 2002 – Nov. 2005 Doctoral research in the group of Prof. K. Kern at Max Planck Institute for Solid State Research, Stuttgart, Germany

Sep. 2004 International Summer School Nicolas Cabrera on "Magnetic Nanostructures", Miraflores de la Sierra, Madrid, Spain

Nov. 2005 PhD thesis, École Polytechnique Fédéral de Lausanne, Switzerland

Publications

Temperature dependence of surface anisotropy of Fe ultrathin films on Cu(001)

A. Enders, D. Peterka, D. Repetto, N. Lin, A. Dmitriev, and K. Kern
Phys. Rev. Lett. **90**, 217203 (2003)

Perpendicular coupling and spin reorientation transition in fcc Fe/Cu/Fe trilayers

A. Enders, D. Repetto, T.Y. Lee, and K. Kern
J. Magn. Magn. Mater. **272-276**, Supp. 1, E959 (2004)

Magnetism of Fe clusters and islands on Pt surfaces

D. Repetto, J. Honolka, S. Rusponi, H. Brune, A. Enders, and K. Kern
Accepted for publication in Appl. Phys. A (2005)

Coupled perpendicular magnetization in Fe/Cu/Fe trilayers

D. Repetto, A. Enders, and K. Kern
Accepted for publication in J. Magn. Magn. Mater. (2005)

Temperature dependence of the magnetism in Fe/Cu(001)

A. Enders, D. Repetto, D. Peterka, and K. Kern
Phys. Rev. B **72**, 054446 (2005)

Structure and magnetism of atomically thin Fe layers on flat and vicinal Pt surfaces

D. Repetto, T.Y. Lee, S. Rusponi, J. Honolka, K. Kuhnke, H. Brune, A. Enders, and
K. Kern
Submitted to Phys. Rev. B (2005)

